Search of exotic particles and $\mathcal{B}f$ measurement of $\Xi^{*0}(1530)\&\Xi_c^0(2470)$ from $\Upsilon(1,2S)$ in Belle

BongHo Kim

Under the supervision of
Professor Stephen Lars Olsen

A dissertation submitted to
the Graduate Faculty of Seoul National University
in partial fulfillment of the requirement
for the Degree of Doctor of Philosophy

Department of Physics and Astronomy
The Graduate School of Natural Sciences
Seoul National University
Seoul, KOREA

August, 2013

Abstract

The possible baryons which has exotic quantum numbers have been predicted from the earliest days of QCD. Though several searches are done, there's still no confident answer. Pentaquark search was increased from 2003 and almost end at 2009 with denial of the existence. But silmilar years, H-dibaryon searches show some possibility and this shows exotic particle search is not dead. In here, i report searches of exotic particle candidates though we could not find any hint of existence.

I present results from searches for exotic multiquark baryon states, including the Ξ_5^{--} pentaquark and the H-Dibaryon in inclusive $\Upsilon(1,2S)$ decays. In addition we report first measurements of the inclusive branching fraction $\mathcal{B}(\Upsilon(1S)\to\overline{\Xi^{*0}}(1530)X) = (3.23 \pm 0.02\ (\text{stat}) \pm 0.26\ (\text{syst})) \times 10^{-3}$, and inclusive product branching fraction $\mathcal{B}(\Upsilon(1S)\to\Xi_c^0(2470)X) \times \mathcal{B}(\Xi_c^0(2470)\to\Xi^-\pi^+) = (3.42 \pm 0.34\ (\text{stat}) \pm 0.15\ (\text{syst})) \times 10^{-5}$, using data samples containing 102 million $\Upsilon(1S)$ decays and 158 million $\Upsilon(2S)$ collected in the Belle detector at the KEKB collider.

Keywords: exotic, pentaquark, H-dibaryon, Belle, branching fraction

Student Number: **2009-20402**

Contents

List of Figures

List of Tables

Chapter 1

Introduction

1.1 Basic concept

The Standard Model is a theory that explains particle physics with three forces and 61 particles. Except for gravity(too small and so negligible in particle interactions), there are three forces and their mediators. The mediators are photons, which mediate electromagnetic interactions, $W^{\pm}$ and Z^0 bosons, which mediate weak interactions, and gluons which mediate strong interactions. (There are 8 different color charged gluons)

Roughly speaking, particle physics is the study of interactions between elementary particles. The 12 mediators, leptons, quarks and Higgs are the elementary particles of the standard model. All of these particles have been discovered, with the last one, the Higgs particle, discovered by CERN in July 2012. Because the $W^{\pm}$ and Z bosons have mass different with other bosons which all have zero mass, the Higgs particle was predicted and finally discovered.

There are three generations of particles classified as leptons which are named e, μ and τ. Each lepton has a partner neutrino and all of them have anti-particles. Quarks are classified in three generations like leptons.

The first generation contains the u and d quarks, the second contains the s and c quark and the third contains the t and b quarks. All quarks have an associated anti-quark. In totall there are 61 particles: 12 leptons, 36 quarks, 12 mediators and the Higgs, as summarized in Fig.1.1.

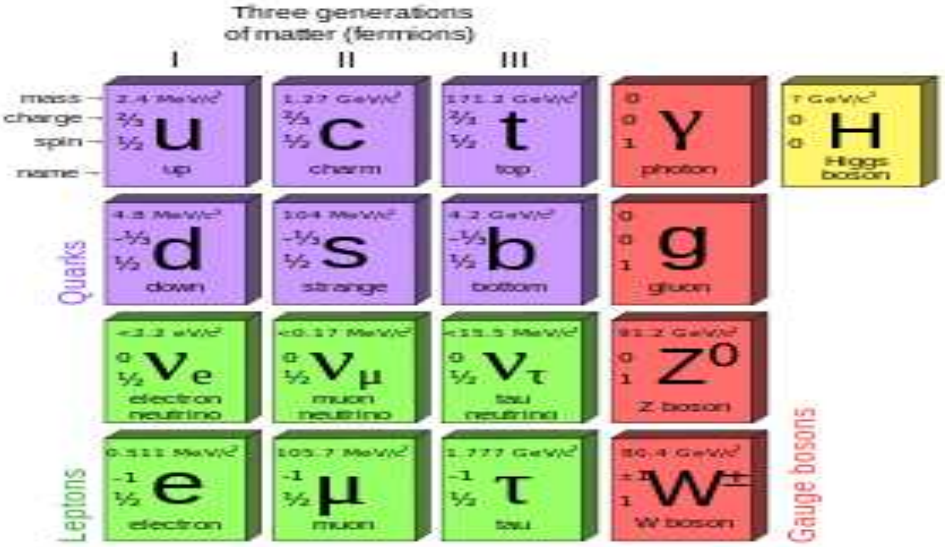

Figure 1.1: Standard model particle list

Although the Higgs has been found and we can think that all of the elementary particles may have been found, we can not be certain. We do not understand the neutrino sector well and we still do not understand QCD very well. Many things need to be studied and figured out.

What we mainly focus on here is QCD , i.e, the strong interaction between quarks and hadrons mediated by gluons or mesons which are bound states of quarks and hadrons. For short distance of order $\sim$ 1fm (the proton's diameter is 1fm), the strong force is dominant compared with other forces. This strong attraction between valance quarks by the strong force is basic to the understanding of the confinement of quarks. Of course when we know more about more exact potential, radius and etc, we need to care many

possible interactions not only confinement.

For the understanding of hadrons that have same-flavor quarks, the Pauli exclusion principla must be considered. This led to the discovery of the color charge, which is at the core of the QCD theory. Gluons carry color charges which is like electromagnetic charge but have 3 different varietes (colors). To explain their properties,Quantum ChromoDynamics(QCD) based on a SU(3) group, is used. With constraint that observed hadrons must be color singlets, we can expect color-anti color pair or three color contributions which are singlets. In addition, QCD also permits the existence of 5, 6 quark combinations, which also satisify the Pauli-principle.

1.2 exotic particles

In the original quark model of Gell-Mann [1] and Zweig [2], baryons are comprised of three quarks. Many experimental searches for baryons with "exotic" quantum numbers, *i.e.,* quantum numbers that can not be produced by any combination of only three quarks, were carried out, but produced ambiguous results [3]. Most of the initial work in this area was concentrated on searches for a strangeness (S)=+1 baryon resonance for which the minimal quark configuration would be $qqq\bar{s}q$ ($q = u$ or d), the so-called pentaquark. Such structures were predicted since the earliest days of QCD [4, 5]. In 1977, Jaffe predicted the existence of a tightly bound, $S = -2$, six-quark structure that has come to be called the H-dibaryon [6].

1.2.1 preview

In the original constituent quark model, many hadrons are explained well by concept of quarks and the eight-fold way. But the constituent quark

model could not explain baryon with same 3 quark, like the Ω or the Δ^{++} which have three same-flavor spin 1/2 quarks and thereby, violate the Pauli-exclusion principle, which does not allow more than one identical quark in same quantum state. This implied the existence of a new degree of freedom that would accomodate the Pauli exclusion principle. The three color charges of the SU(3) color gauge theory were introduced to explain these particles. So 3 kind of colors (Red, Green, Blue) are assigned with the condition that all particles need to be color singlet(= Red + Green + Blue). By this condition, we can predict many hadrons with more complex quark combinations, such as $qq\bar{q}q$, $qqqq\bar{q}$ and $qqqqqq$. We refer to these as exotic particles.

1.2.2 penta-quark

Penta quark is a hypothesized exotic particle candidate that is composed of 4 quarks and 1 anti-quark. After it was first proposed by Michal Praszalowicz in 1987 [7], it was realized that the color structure of QCD suggests that the lowest lying pentaquark flavor $SU_F(3)$ multiplet is an anti-decuplet that contains an S = +1 iso-singlet, the Θ_5^+, and the $I_3 = \pm 3/2$ members of the $S = -2$ isospin 4-plet, the Ξ_5^+ and the Ξ_5^{--}, both of which have exotic quantum numbers with spin 1/2 and even parity. In 1997, Diakonov, Petrov and Polyakov proposed a chiral soliton model that predicted the mass of the Θ_5^+ to be 1530 MeV with width less than 15 MeV as in Fig. 1.2 with [8]. (The Particle Data Group call Ξ_5 state the $\Phi(1860)$).

Interest in this subject increased considerably in 2003, when the LEPS group reported the observation of a narrow resonance-like peak in the K^+n invariant mass spectrum produced in the $\gamma n \to K^+K^-n$ photoproduction process that they attributed to the Θ_5^+ [9]. The peak position, 1540$\pm$10 MeV, and width, $\Gamma < 25$ MeV, were in good agreement with the predictions of Ref. [8]. The LEPS result implied a large production rate for the Θ_5^+; the

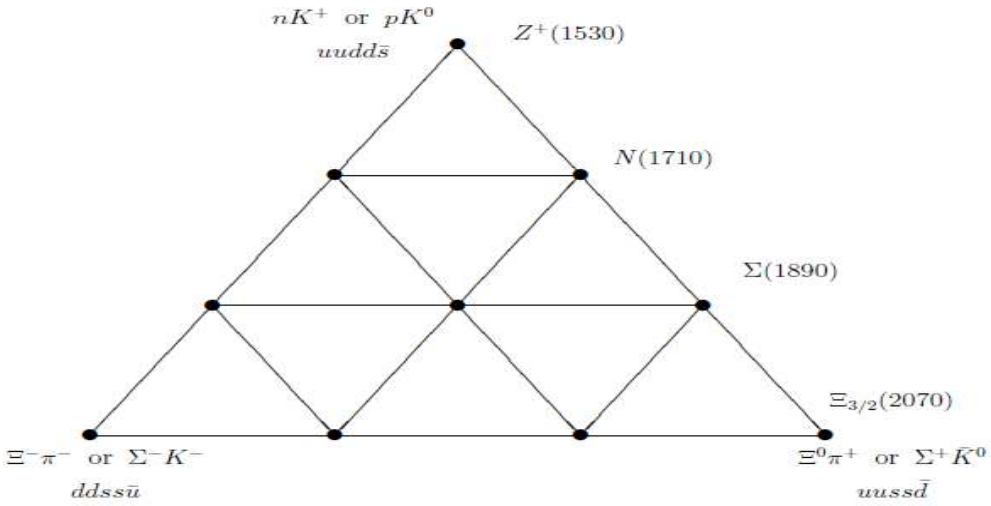

Figure 1.2: The suggested anti-decuplet of baryons. The corners of this (T_3, Y) diagram are exotic. We show their quark content together with their(octet baryon + octet meson) content, as well as the predicted masses.

observed K^+n peak contains 19.0 ± 2.8 events, which is about 2/3rds the number of events in the $\Lambda(1520) \rightarrow K^-p$ peak that is seen in the same sample of selected K^+K^-n events.

The LEPS result stimulated a huge amount of theoretical and experimental activity over the next three years [10]. After a number of reported positive signals for pentaquarks, a number of high statistics attempts at confirming these results found no signals and reported cross section or branching ratio limits that often contradicted earlier sightings. Now there is a general consensus that the original sighting was likely incorrect and that pentaquarks, if they exist at all, are produced with cross sections or branching fractions that are substantially below those inferred from the early sightings [11].

Among the experiments that reported a positive pentaquark signal was the NA49 experiment which reported greater than 5σ evidence for the production of a narrow $\Xi_5^{--} \rightarrow \Xi^-\pi^-$ resonance [12] at a mass of 1862 ± 2 MeV

and a width less than the detector resolution of 18 keV FWHM in fixed target proton-proton collisions at $\sqrt{s} = 17.2$ GeV [13]. This result was in good agreement with a Jaffe and Wilczek prediction in 2003 [15] that this state have mass of 1.75GeV and width only $\sim 50\%$ greater than that of the Θ_5^+. A subsequent high statistics search for Ξ_5^{--} production in $\sqrt{s} = 1.96$ GeV proton-antiproton collisions by the CDF group(2007) failed to confirm the NA49 Ξ_5^{--} claim. In contrast to the NA49 measurements, which did not have very good acceptance for the $\Xi^{*0}(1530) \to \Xi^-\pi^+$ mass region [14], the CDF group sees a strong, ∼2000-event signal for $\Xi^{*0}(1530) \to \Xi^-\pi^+$ and sets limits on the ratio of the cross sections times branching fraction for Ξ^{--} and $\Xi^{*0}(1530)$ production and decay over the [1600-2100] MeV mass range that are less than $3 \sim 4\%$ for a narrow ($\Gamma = 0$) Ξ^{--} and less than $4 \sim 6\%$ for $\Gamma = 17$ MeV [16]. With CDF results, many other reports have been released that fail to see Ξ_5^{--} in pp, ep, pA and γA production experiments. Recently, an upper limt was established in conjunction with 6.5k $\Xi(1530)$ event from the FOCUS γp experiment. [17]

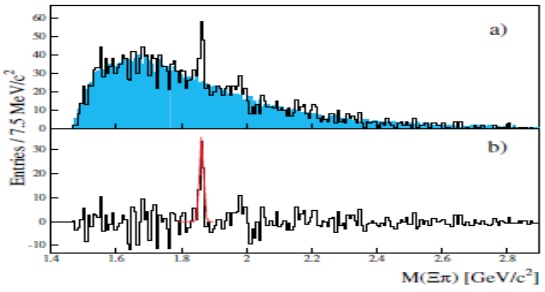

Figure 1.3: NA49(pp) results that (a) The sum of the $\Xi^-\pi^-$,$\Xi^-\pi^+$,$\bar{\Xi}^+\pi^-$ and $\bar{\Xi}^+\pi^+$ invariant mass spectra. The shaded histogram shows the mormalized mixed-event background. (b) Background subtracted spectrum with the Gaussian fit to the peak.

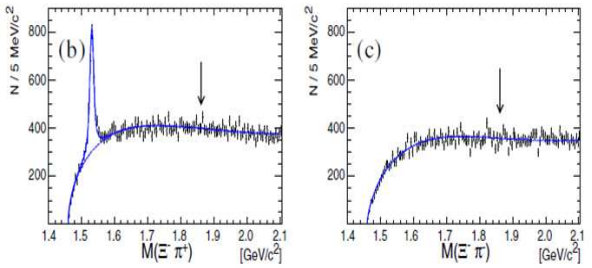

Figure 1.4: CDF pp collision results that (b) $\Xi^-\pi^+$ combinations, which display a clear $\Xi^{*0}(1530)$ peak; (c) $\Xi^-\pi^-$ combination. Arrows mark the mass at $1862MeV/c^2$, where the NA49 Collaboration reported obsesrving the Ξ_5. The smooth curves represent fits to the spectra.

1.2.3 H-dibaryon

In 1977, Jaffe predicted the possible existence of a doubly strange, six-quark bound structure (uuddss) with quantum mumbers $I = 0$ and $J^P = 0^+$ and a mass that is $\simeq 80MeV$ below the $2m_\Lambda$ threshold, which he called the H-dibaryon under the title "Perhaps a Stable Dihyperon" using MIT bag model. [4] Although the H-dibaryon has quantum numbers consistent with those of a $\Lambda - \Lambda$ bound state as a baryon-baryon molecule like deuteron, it was proposed, instead, to be a tightly bound single hadron with a strong binding energy and distinct from a deuteron or any other 6 quark configuration. Jaffe's H-dibaryon is a six-quark system containing two up, two down, and two strange quarks can exist in an SU(3)-flavor siglet with spin zero which takes maximum advantage of the attraction due to the color-magnetic interactions of quantum chromodynamics. As the ground state in the S = -2 sector of a B = 2 system, the H-dibaryon is stable against the strong interaction and can only decay via the weak interactions and , thus,

be long-lived, i.e. $c\tau \geq 3cm$, and with negligible width. By this expectation, we can strongly suggest existance of H-dibaryon but we can't predict exact mass and decay time of H-dibaryon because lack of experimental results and limitations of the non-perturbative theory.

In his paper, Jaffe predicted a binding energy of $80MeV$, but also predicted a possible energy range and several decay channels. If the H-dibaryon's binding energy is lower than 2 neutron masses ($M_H \geq 2m_n$), it is absolutely stable and will decay only with baryon number violation. If the H-dibaryon mass is in the range ($2m_\Lambda \geq M_H \geq 2m_n$), the H-dibaryon can decay via a Δ = 1,2 weak process. If H-dibaryon mass is above $2m_\Lambda$, it will strongly decay with negligable small life-time. Right after Jaffe's prediction, extensive searches of the H-dibaryon were carried out, using a wide range of production mechanisms and searching for different decay signatures. Having such a large binding energy, it was thought to be easy to detect and the experimental searches were very active. To date there have been no conclusive experimental results on the existence of the H-dibaryon.

For masses below threshold $M_H = 2m_\Lambda$, the H would predominantly decay via $\Delta S = +1$ weak interactions to Λn, $\Sigma^- p$, $\Sigma^0 n$ and $\Lambda p\pi^-$ final states. Just above threshold, the H would decay via strong interactions to $\Lambda\Lambda$; the $\Xi^0 n$ channel opens at 23.1 MeV above $2m_\Lambda$ and the $\Xi^- p$ channel opens 5.6 MeV above that. About production process, the H-dibaryon can be produced via (K^-, K^+) reaction, Ξ^--capture, heavy ion collision, $\bar{p}$-nucleus annihilation reaction, etc. For several reaction process from several collaboration like BNL, Fermilab, KEK, etc, each mass region's upperlimit is setted. The $\Lambda\Lambda$ channel was studied by the E522 collaboration at KEK [24], and they saw an intriguing near-threshold enhancement but with limited statistics. The BNL-E836 collaboration at Brookhaven National Laboratory searched for the reaction $^3He(K^-, K^+)Hn$ and put stringent cross section limits spanning the range 50 MeV $\leq B_H \leq$ 380 MeV [25]. Searches for a bound H decaying to $\Lambda p\pi^-$ have reported negative results [26, 27]. Some

earlier searches, also with negative results, are listed in Ref. [28]. Fig. 1.5 shows two positive results of existance of H-dibaryon. The left-hand panel is $M(\Lambda\Lambda) - 2m_\Lambda$ distribution from E522 collaboration at KEK. The shaded histogram shows the data and the lines indicate the expected background. Above threshold, a small enhancement is seen but the statistics are low. The right-hand panel is the $M(\Lambda p\pi)$ distribution from Star collaboration at BNL. Points are data and red line is background distribution estimated by side-band [18]. But it's hard to distinguish any signal from the background, which peaks near threshold and Star collaboration reported a negative result.

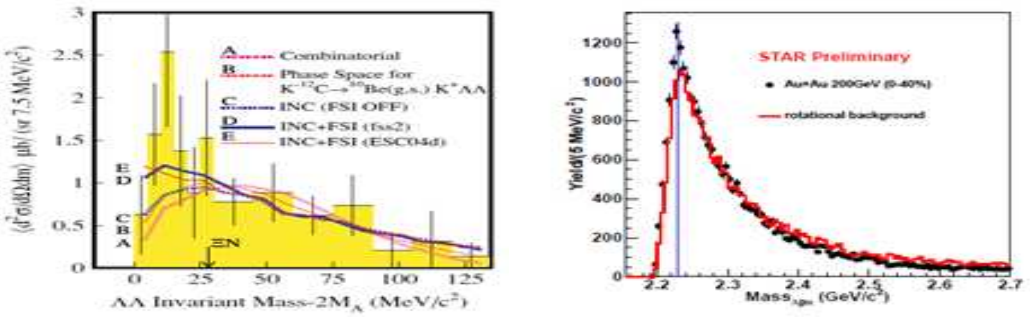

Figure 1.5: **Left:** $\Lambda\Lambda$ invariant mass distribution $-2M_\Lambda$ from E522 collaboration at KEK **Right:** $M(\Lambda p\pi)$ mass distribution (point) and estimated background (red line) from star experiment.

Jaffe's original prediction has been ruled out experimentally by the observation of double-Λ hypernuclei events in 2000 year. Details are in the following subsections. The celebrated "Nagara" event (a ${}^{6}_{\Lambda\Lambda}He$ hypernucleus with $B_{\Lambda\Lambda} = 7.13 \pm 0.87 MeV$), translated to a 90% confidence level limit that excludes $M_H \leq 2223.7 MeV$.

Although Jaffe's original prediction is ruled out, the theoretical case for the existence of an H-dibaryon with a mass near $2m_\Lambda$ continues to be strong and, in fact, has been strengthened by recent lattice QCD calculations by the NPLQCD [19] and HALQCD [21] collaborations in 2011 year, which

both found a bound H-dibaryon, albeit for non-physical values for the π mass. An updated NPLQCD result is $B_H = 13.2 \pm 4.4$ MeV for a π mass $m_\pi \simeq 390$ MeV [20]; the HALQCD result is $B_H = 37.4 \pm 8.5$ at $m_\pi \simeq 837$ MeV. The NPLQCD group used these measurements to extrapolate to the physical π mass: using a quadratic extrapolation they find a bound H with $B_H = 7.4 \pm 6.2$ MeV; a linear extrapolation gives $B_H = -0.2 \pm 8.0$ MeV [20]. Carames and Valcarce recently studied the H using a chiral constituent model, constrained by the elastic and inelastic ΛN, ΣN, ΞN and $\Lambda\Lambda$ cross sections [23]. They find values for B_H in the same range as the extrapolated LQCD values.

double-Λ hypernuclei search

There are two ways to search for the H-dibaryon. One is a direct search of H-dibaryon and the other is searching double-Λ hypernuclei with $S = -2$. The binding energy of the two hyperons inside a nucleus gives an upper limit for the binding energy of the free H-dibaryon. It means that if the mass of the H-dibaryon were below the available energy of the ΛΛ system in a double-Λ hypernuclei, the Λ pair of hypernuclei would form an H-dibaryon via strong interaction and decay with in the original nuclei with this energy. But if mass of the H-dibaryon is above bind energy of the two hyperons then Λ could decay by weak interaction. Initially, there were many direct H-dibaryon searches but with no positive signals or hints of the existence. So eventually many hypernuclei experiments were done and the celebrated "Nagara" event, which has the relatively unambiguous signature of a ${}^{6}_{\Lambda\Lambda}He$ hypernucleus produced via Ξ^- capture at rest in a photographic emulsion. [22] The ΛΛ binding energy, determined to be $B_{\Lambda\Lambda} = 7.13 \pm 0.87 MeV$, translates to a 90% confidence level lower limit of $M_H \geq 2223.7 MeV$, severely narrowing the window for a stable H to $B_H \geq 7.9 MeV$. Here, the binding energy $B_{\Lambda\Lambda}$ is mass difference that $B_{\Lambda\Lambda} \equiv M({}^{A-2}Z) + 2m_\Lambda - M({}^{A}_{\Lambda\Lambda}Z)$. From the follwing relation: $M_H \leq 2m_\Lambda - B_{\Lambda\Lambda}$, we can get the lower limit on the H-

dibaryon mass. The reason for using emulsion experiments, in spite of their poor efficiency, is their excellent for resolution for measuring short tracks.

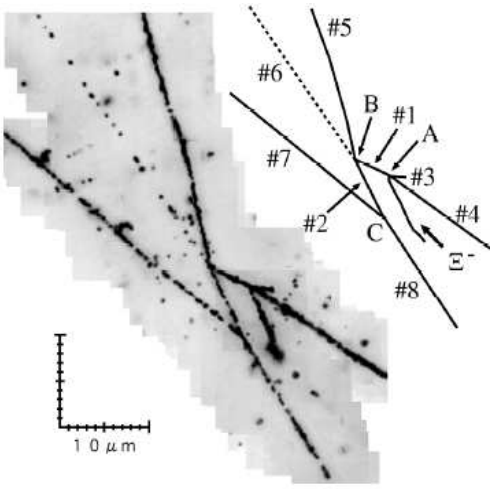

Figure 1.6: Photographic emulsion picture from Ξ^- capture to hypernuclei (S = 2) decay as named Nagara "event".

The "Nagara" event is shown in Fig. 1.6. After the collision of a Ξ^- and ^{12}C at point A, doubly strange hypernucleus track is denoted as #1. This track is just a few μm long and it's not possible to detect such a short track by any other detection method. After one Λ weakly decays to p and π (tracks #5 and#6) at position B, strangeness hypernuclus #2 decay at position C.

In addition to the "Nagara" event a few other doubly strange hypernuclei events have ever been recorded as in Table. 1.1. Among these, the Nagara event provides the most stringent mass limit for the H-dibaryon. In Table. 1.1, the upper two experiments are ambiguous because of no photograph was published and the reaction was not identified. The next four candidates that are listed found in KEK experiments. (i need to mention that we don't know whether $S = -2$ component in a double hypernuclus just takes the form of $\Lambda\Lambda$ or H-dibaryon itself and it is not a simple question. It is possible

that H-dibaryon state is in double hypernucleus and weakly decay.)

Table 1.1: Reported double hypernuclear events. [31]

Event	Nuclide	$B_{\Lambda\Lambda}(MeV)$	$\Delta B_{\Lambda\Lambda}(MeV)$
1963	${}^{10}_{\Lambda\Lambda}Be$	17.7 ± 0.4	-4.3 ± 0.4
1966	${}^{6}_{\Lambda\Lambda}He$	10.9 ± 0.5	-4.7 ± 1.0
E176	${}^{13}_{\Lambda\Lambda}B$	23.3 ± 0.7	-0.6 ± 0.8
NAGARA	${}^{6}_{\Lambda\Lambda}He$	6.91 ± 0.16	-0.67 ± 0.17
MIKAGE	${}^{6}_{\Lambda\Lambda}He$	10.06 ± 1.72	-3.82 ± 1.72
DEMACHIYANAGI	${}^{10}_{\Lambda\Lambda}Be$	11.90 ± 0.13	-1.52 ± 0.15
HIDA	${}^{11}_{\Lambda\Lambda}Be$	20.49 ± 1.15	-2.27 ± 1.23
	${}^{12}_{\Lambda\Lambda}Be$	22.23 ± 1.15	

Theoretical approaches

Because of color confinement, i.e, no-existance of bare quarks and gluons in nature, quarks can't be studied by direct way. It means that we need to study quark and gluon interactions by collision or decay of hadrons. As hypothetical understanding of hadron confinement, many theoretical approaches are in QCD inspired and many theories are explaining well hadron dynamics without strangeness. But by adding strangeness, SU(3) symmetry is broken and model can't explain exactly. After Jaffe' paper, many theoretical calculations have been made from bag model, quark cluster model, Skyrme model and also in Lattice QCD. Many of them predict positive results as binded H-dibaryon. You can find several prediction in [32]'s Fig.1. What is explained below is constituent quark models(QCD inspired quark model). As basic concept, for hadron's potential expectation of QCD, color confinement and asymtotic freedom are two important features. Many models have different phenomology for this confinement but almost all explain single hadron properties well. With confinement term, one-gluon exchange potential and meson

exchange potential is mainly considered.

$$H = \sum_{i}^{n} \frac{p_i^2}{2m_i} - K_{cm} + \sum_{i<j} V_{ij}^{OGE} + V_{ij}^{conf} + V_{ij}^{psM} \tag{1.1}$$

S-wave quarks carry color $SU_c(3)$, flavor $SU_F(3)$ and spin-parity SU(2). In the one-gluon exchange potential, chromomagnetic interaction(CMI) is the main force for the binding of the H-dibaryon in the original jaffe's prediction. One-gluon exchange potential is below Eq. 1.2 [36] and CMI term is that is proportional to $\sigma_i \cdot \sigma_j \lambda_i \cdot \lambda_j$ where σ_i is the Pauli matrix for the spin SU(2) group and λ_i is the Gell-Mann matrix for the color $SU_c(3)$ so CMI term is colorspin $SU_{cs}(6)$ term.

$$V_{OGE}(r_{ij}) = \frac{\alpha_s}{4} \Lambda_i \cdot \Lambda_j \left\{ \frac{1}{r_{ij}} - \left(\frac{\pi}{2m_i^2} + \frac{\pi}{2m_j^2} + \frac{2\pi \sigma_i \cdot \sigma_j}{3 m_i m_j} \right) \delta(r_{ij}) - \frac{S_{ij}}{(4 m_i m_j r_{ij}^3)} \right\} + (spin - orbit\ term). \tag{1.2}$$

Here α_s is quark-gluon coupling constant and r_{ij} is distance between quarks. The last term which has tensor operator S_{ij} is tensor force term. In the SU(3) symmetric limit, expectation value of the sum of $\sigma_i \cdot \sigma_j \lambda_i \cdot \lambda_j$ matrix calculation [37] is below,

$$\Theta \equiv -\langle \sum_{i<j} \sigma_i \cdot \sigma_j \lambda_i \cdot \lambda_j \rangle = n(n-10) \ + \ \frac{4}{3} J(J+1) \ + \ \langle (\sum_i f_i)^2 \rangle, \tag{1.3}$$

First term only depends on quark number and second term depends on spin. both valuables are fixed value. Third term depends Casimir operator from colorspin $SU_{cs}(6)$ and this term is main motivation of H-dibaryon be like bound state. Two Λs have $\langle (\sum_i f_i)^2 \rangle = 12$ and H-dibaryon has 0 because of flavor-singlet state. Total value Θ is -16 for two Λ seperate state and -26 for one H-dibaryon. Because of this short range potential difference, H-dibaryon be interested. Differ with this attraction, we can simply understand

that 6 quarks in the same spatial point is forbidden by the pauli exclusion for NN,NY or YY channels but flavor siglet H-dibaryon is not affected by pauli exclusion and have attractive potential in short distance. For estimating bound state, we need to care not only quark interaction, but also π interaction and other pseudo scalar meson interaction which is important in middle and long range interaction. These meson interactions are understanded with baryon-baryon channel coupling calculation like $\Lambda\Lambda - N\Xi - \Sigma\Sigma$ with meson as mediator. But about sclar meson contribution and instanton-induced contribution is model dependent. So each model and papers shows different bound energy and existance of H-dibaryon.

1.2.4 State of these exotic candidate?

Although penta-quark and H-dibaryon are predicted by QCD with quark interaction potential not like deuteron, we can't convince about particle structure if we find resonance near threshold which have many possibility. As we know, resonance is arise by attraction in short distance and repulsion in long distance. So from the interplay resonance is generated. There's two possibility that one is single channel as one confined hadron and the other is scattering with confined channels was developed by Feshbach as known Feshbach resonance. [34] For explaining narrow resonance of Θ_5 from LEPS results, Jaffe study about this possibility. [35] Feshbach resonance can be understanded in weak transition potential between one closed channel and two confined channel. In collision of two scattering particles make one closed channel and then transition is reversed and decay to two particles. If new states have angular momentum, we can add angular momentum barrier term $\sim l(l+1)/2\mu\, r^2$ for repulsion. But especailly s-wave particle like H-dibaryon, because of no effect of angular momentum, we can't expect narrow resonance without feshbach resonance. If we can get enough attraction in short distance range like H-dibaryon first predicted, we can expect tight bound state, but

if we get eventually repulsive in short distance by all effect, we need to care about molecules state like feshbach resonance.

1.3 Inclusive decays of the Υ(1S,2S) to baryon with $S = -2$

Decays of the $\Upsilon(1,2S)$ are particularly well suited for searches for doubly strange multiquark states. The $\Upsilon(1S)$ is a flavor-$SU(3)$ singlet, and its dominant decay mode is $\Upsilon(1S) \to ggg$, with a branching fraction of $81.7 \pm 0.7\%$ [29]. The decay final states contain u-, d-, s-, $\bar{u}$-, $\bar{d}$- and $\bar{s}$-quarks in roughly equal numbers. The high density of quarks and antiquarks in the limited phase space of the final state is conducive to the production of multiquark systems. For example, the inclusive branching fraction for antideuteron ($\bar{D}$) production is substantial: $\mathcal{B}(\Upsilon(1S) \to \bar{D}\,X) = (2.9 \pm 0.3) \times 10^{-5}$ [30]. The branching fraction for $\Upsilon(2S) \to ggg$ is smaller, $58.8 \pm 1.2\%$ primarily because of competition from the addition channels associated with intra-bottomonium transions such as $\Upsilon(2S) \to \pi^+\pi^-\Upsilon(1S)$ $(18.1 \pm 0.4\%)$ and $\Upsilon(2S) \to \gamma\chi_{b1,2,3}$ $(17.9 \pm 0.7\%)$. These latter decays produce final-state $\Upsilon(1S)$ and $\chi_{b1,2,3}$, which are also flavor-$SU(3)$ singlets. The antideuteron production rate is similar: $\mathcal{B}(\Upsilon(2S) \to \bar{D}\,X) = (3.4 \pm 0.6) \times 10^{-5}$ [30]. An upper limit for the production of a 5- or 6-quark $S = -2$ state in $\Upsilon(1S)$ decays that is substantially below that of the 6-quark antideuteron would be strong evidence against their existence.

Chapter 2

KEKB Accelerator and Belle Detector

2.1 KEKB Accelerator

KEKB is an asymmetric energy electron-positron collider constructed as B-factory in KEK. KEKB, constructed from 1994, showed steady improvement in performance from in June 1999 as physics experiment run to the end of June 2010 and turned off. After the peak luminosity reach the designed value of $1.0 \times 10^{34}\ cm^{-2}s^{-1}$ in May 2003, the maximum peak luminosity was recoreded $2.11 \times 10^{34}\ cm^{-2}s^{-1}$ in June 2009. With stable performance, Belle detector which was started in June 1999, have collected $1041 fb^{-1}$ totall luminosity. With this world best luminosity, predicted CP violation from the Kobayashi-Maskawa theory was measured and prof.Kobayashi and Maskawa were awarded the 2008 Nobel Prize in Physics. Detailed luminosity information and all summary of KEKB accelerator is in . [38]

2.1.1 Feautres of KEKB

KEKB Accelerator is aymmetric energy electron-positron collider with an 8 GeV electron ring (HER) and 3.5 GeV positron ring (LER) with 3016 m long rings as Fig. 2.1. This energy asymmetry is required to detect the complex phase of the KM matrix. Asymmetry of energy is not innovative beam physics because target experiments, e-p collison or even BABAR are asymmetric particle experiment. But giving crossing angle is not popular in collision and historically unsuccessful from the DORIS experiment that they achieved very small vertical beam-beam parameter $\xi_y \sim 0.01$ which propotional to luminosity. With taking resk of small luminosity problem, there's merits that finite crossing angle seperate of two beams without placing deflecting dipole magnets, give weaker background, etc. By studying good tuning, KEKB get high luminosity with $\pm$ 11 *mrad* crossing angle.

The designed current in KEKB is 1.1A in the HER and 2.6A in the LER. In order to achieve high luminosity, stable high current and small beam size at the IP point is nessesary issue.

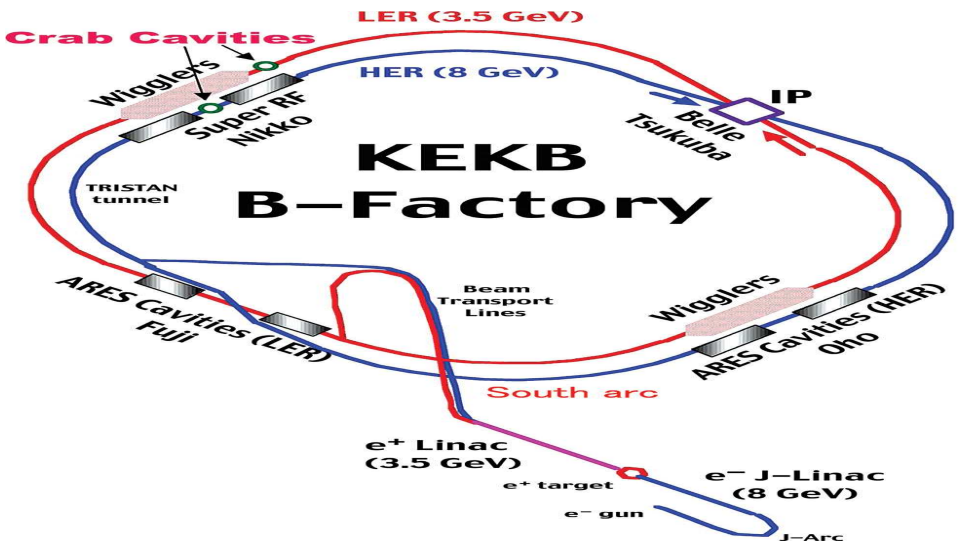

Figure 2.1: Schematic layout of KEKB.

2.2 Belle Detector

The Belle detector is a large-solid-angle magnetic spectrometer that consists of a silicon vertex detector (SVD), a 50-layer cylindrical drift chamber (CDC), an array of aerogel threshold Cherenkov counters (ACC), a barrel-like arrangement of time-of-flight scintillation counters (TOF), and an electromagnetic calorimeter (ECL) comprised of CsI(Tl) crystals located inside a superconducting solenoid coil that provides a 1.5 T magnetic field. An iron flux-return with layer of detector located outside of the coil is instrumented to detect K_L mesons and to identify muons (KLM). Measurements of dE/dx in the CDC, light yields in the ACC and flight times in the TOF are combined to form particle identification (id) likelihoods $\mathcal{L}(h)$ ($h = \pi^+$, K^+ or p) for charged hadronic tracks. Hadron id assignments are based on the likelihood ratios

$$R(h|h') = \frac{\mathcal{L}(h)}{\mathcal{L}(h) + \mathcal{L}(h')}. \tag{2.1}$$

The detector is described in detail elsewhere [39].

Fig. 2.2 shows the configuration of the Belle detector. With the beam crossing angle ± 11 mr and 1.5T magmetic field, belle detector cover 4π angle all with asymmetric feature for the task force to test CP-violation. Small angle part near beam line covered by BGO crystal arrays(EFC) placed on the surfaces of the QCS cryostats in the forward and backward direction.

2.2.1 Interaction region

3.5 GeV e^+ positron beam (LER) and 8 GeV e^- electron beam (HER) collide in IP position inside BELLE TSUKUBA Hall. With the merit of high luminosity, ±11 mr crossing angle is setted by beam line magnet with final-focus quadrupole magnets(QCS) which is also shown Fig. 2.2 by avoiding parasitic collision background. To avoid hardness of bending lower momentum beam particles by solenoid, we bent high energy e^- beam (HER) 22 mr for the

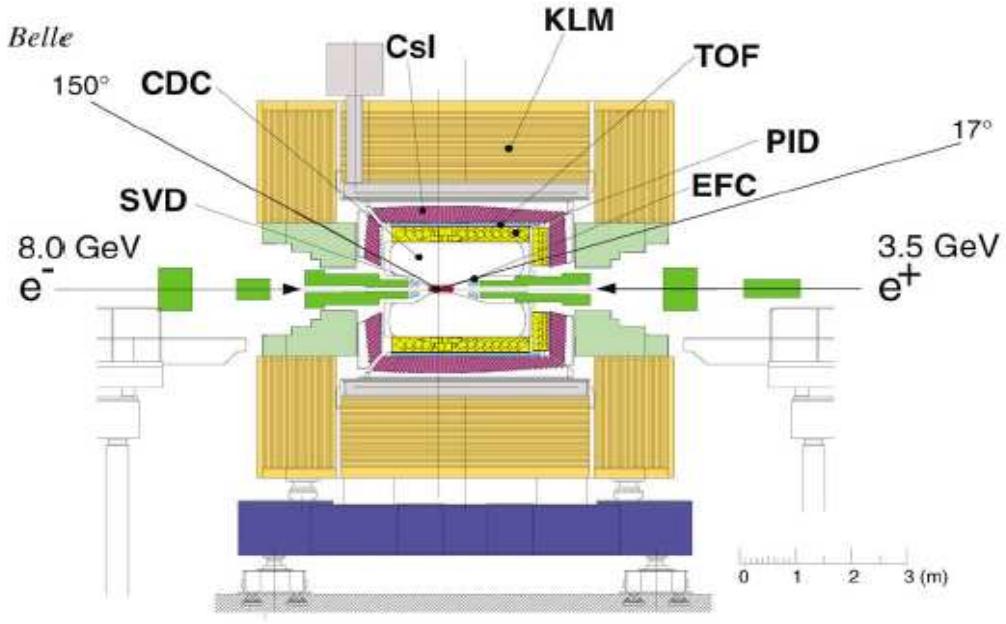

Figure 2.2: Side view of the belle detector.

solenoid axis.

To reduce background by beam pipe or synchrotron radiation, beam pipe made the thickness minimized for reducing multiple coulomb scattering. As mentioned before, elimination of the seperation magnet by giving crossing angle and attached masks in beam pipe reduce synchrotron radiation. By this way, problems happened in TRISTAN is solved.

2.2.2 EFC

EFC is Extreme Forward Calorimeter which is useful for analysis of extend the polar angle coveraging $17^o < \theta < 150^o$ by ECL by adding from 6.4^o to 11.5^o and from 163.3^o to 171.2^o. Also if particles decay to polar only, it's hard to trigger by TOF then EFC give trigger signal as sub-detector for triggering. The other task of EFC is to be raiation hard as placed in high radiation-level area and be masks to reduce background for CDC. It also

require enough high resolution for two-photon physics study even under high dose condition. Selected BGO crystal calorimeter has below property that

- radiation hardness at megarad level,($\sim 10 Mrad$ dose decrease $\sim 30\%$ light output)
- excellent e/γ energy resolution of (0.3 - 1)%/$\sqrt{E(GeV)}$,
- high density of 7.1 gm/cm^3,
- short radiation length of 1.12 cm,
- large refractive index of 2.15,
- suitable scintillation at about 480 nm,
- non-hygroscopic nature.

Radiation damage to refractor and glues also studied and photodiods are also selected good for radiation dose. The detector is segmented into 32 in ϕ and 5 in θ angle for both the forward and backward corn. The BGO crystal itself are contained in 1 mm thick stainless steel and photodiode is attatched.

Fig. 2.3 **(Upper)** shows LER and HER currenct for 4000 sec and lower figures are EFC coincidence **(left)** rate and accidental **(right)** rate. With the correlation between forward and backward EFC detector signal, we can check Bhabha rate. Forward EFC shows rms resolution of 7.3% for 8 GeV beam and backward EFC shows rms resolution of 5.8% for 3.5 GeV beam.

2.2.3 SVD

SVD is Silicon Vertex Detector which is important detector to measure exact difference in z-vertex positions of B meson pairs for observing time-dependent CP asymmetries in decays of B mesons. For this goal, $\sim 100 \mu m$ precision is required to silicon vertex detector with average distance between the two vertices is 200 μm.

SVD had been changed with new version from 1(1.0, 1.2, and 1.4) to 2 because of gain decrease caused by radiation damage. The SVD is required

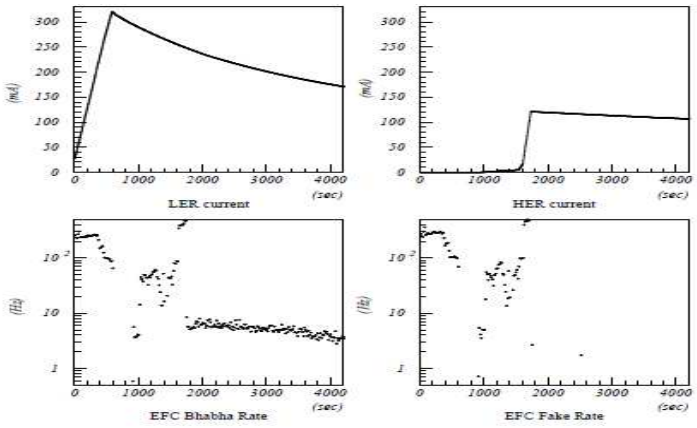

Figure 2.3: An operation history of a typical beam fill of KEKB. The top figures show e^+ and e^- beam current, and the bottom figures the coincidence rate of the forward and backward detectors (left) and their accidental rates (right) of EFC.

not only radiation hardness but also high momentum resolution with restriction of multiple-coulomb scattering to approach to the IP position, rigidity of the support structure. So the SVD require all condition but it is sensitivie and breakable. Fig. 2.4 shows geometrical configuration of the SVD1. The difference between version 1 and 2 is in Table. 2.1. The $\Upsilon(1S, 2S)$ resonance samples are collected after SVD2 installation.

SVD have 3 or 4 layers which are constructed from each ladders. Each ladder has double-side silicon strip detectors (DSSDs). In SVD, each DSSD consists of 1280 sense strips and 640 readout pads on opposite sides. The z-strip and ϕ-strip pitches are $42\mu m$ and $25\mu m$. Double-side means detecting x-y position both by cross n and p type strip in opposite side differ with normal strip detector which use one side for position detection. A proper biasing on the strips generates electron-hall pair inside of medium by particle penetration and these pairs are collected by the strips which give 2 dimensional position.

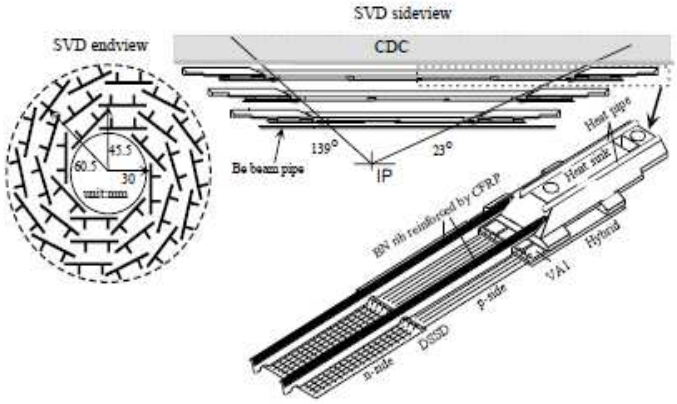

Figure 2.4: Detector configuration of SVD.

With covering same angle of CDC, $\sim$ 97% matching is shown between tracking of SVD and CDC. The momentum and angular dependence of the impact parameter resolution of SVD2 is represented by $\sigma_{xy} = 21.9 \oplus 35.5/(p\beta \sin^{3/2}\theta)\mu m$ and $\sigma_z = 27.8 \oplus 31.9/(p\beta \sin^{5/2}\theta)\mu m$.

2.2.4 CDC

The Belle Central Drift Chamber(CDC) is multi-wire cylinderical drift chamber as main tracking devide for detecting charged particle informations by charged drift, diffusion and energy loss inside gas filled chamber. The physics goals for CDC require a momentum resolution of $\sigma_{pt}/p_t \sim 0.5\%\sqrt{1+p_t^2}$ (p_t in GeV/c) for all charged particles with $p_t \geq$ 100MeV/c in the polar angle region of $17^o \leq \theta \leq 150^o$. [39]

Basic concept

Basic phenomena is ionization and excitation of gaseous molecules by traversed charged particles. Other electromagnetic processes like cherenkov radiation, bremsstrahlung, etc have negligible energy loss. Electrons and ion-

Table 2.1: Comparision of SVD1 and SVD2.

Parameter	SVD1	SVD2
Number of DSD layers	3	4
Number of total DSSD ladders	8 + 10 + 14 = 32	6 + 12 + 18 + 18 = 54
Coverage	$23^o < \theta < 139^o$	$17^o < \theta < 150^o$
Radius of beam pipe	2 cm	1.5 cm
Radius to the first layer	3 cm	2 cm
Radius to the final layer	6 cm	8.8 cm
Radiation tolerance	$<$ 1 MRad	$<$ 20 MRad
Readout chip	VA1	VA1TA
Working period	$Jan.1999 \sim Jul.2003$	$Aug.2003 \sim now$

ized ions by ionization of gaseous molecules are trace of particle trajectory. Because several wire detectors are placed each cell, connection of continuing detected signal be track of charged particle. By giving magnetic field for charged particle, we can get momentum using bent track. Because we also have particle property dE/dx which is usable for particle identifying, CDC is very important detector for charged particle.

Eq.2.2 is Bethe-Bloch formula for average differential energy loss due to Coulomb interactions. As we know energy loss is depend on cross section of particles and this cross section depends on mass and Z, etc. So different property of particle make different energy loss. In formula, ρ : density of absorbing material, z : charge of incident particle, W_{max} : maximum energy transfer in a single collision, δ : density correction, C : shell correction. W_{max} depends on mass and velocity of incident particle. Two correction term in end of formula is important for high energy(δ) and low energy(C) incident particles. Because we focus on momentum more than 100MeV/c, density correction is important for light particle.

$$\frac{dE}{dx} = 2\pi N_a r_e^2 m_e c^2 \rho \frac{Z}{A}\frac{z^2}{\beta^2}[\ln(\frac{2m_e\gamma^2\nu^2 W_{max}}{I^2} - 2\beta^2) - \delta - 2\frac{C}{Z}]. \qquad (2.2)$$

For the mass below deuteron, if momentum be larger that 1GeV it become hard to distinguish by dE/dx distribution as minimum ionization plateau as Fig. 2.5. Although this figure doesn't show Kaon line, we can expect line will be middle of proton and π line.

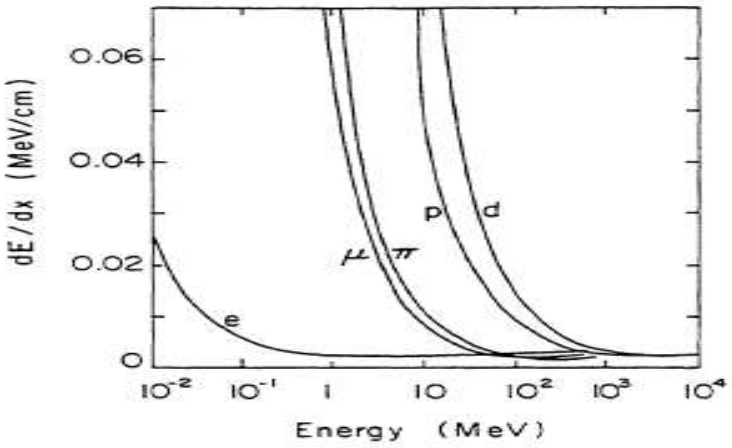

Figure 2.5: Energy loss per unit length in air by Eq.2.2. At energies above 1GeV/c, all particles lose about the same amount of energy(minimum ionization plaeau). [40]

Because we need to emphasize signal compare with noise, we use avalanche multiplication by accelerating electron. We gather electrons formed liquid drop like avalanche multiplication (electron is more mobile than ions) made by ionization of gas molecules by electric field accelerate ionized electron. We can get dE/dx parameter by gathering electron with constant electric field using multiplication factor and gas gain.

For getting track information of 3 dimension, i.e. measurement of r-ϕ and z coordinate, we use wire detector and cathode stripe detector. By cell

structure with 8400 cell which have z direction wires, we can draw track for r-ϕ signal distribution. For getting z position information, we use division of signal charges at both ends of the wire. Almost half of wire have few mrad stereo angle named stereo wire help more precise z position. But these technique resolution is typically of the order of several mm. For getting $\sim$ 100 μm resolution like r-ϕ resolution, we use cathode stripe detector. When electron avalanche be gathered in wire, we can detect current signal in wire detector and we can also detect induced charge by current in cathode stripe detector as Fig. 2.6 which is arrayed perpendicular to wire detector.

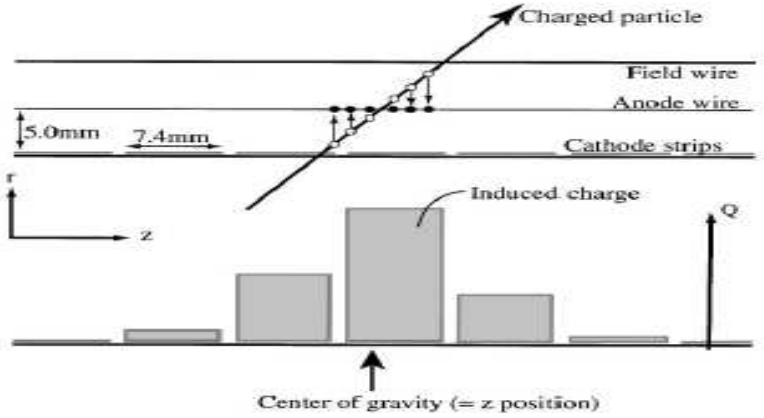

Figure 2.6: An illustration of the principle of cathode image readout. [41]

structure and electronics

As shown in Fig. 2.7, the CDC provide an angular coverage of $17^o \leq \theta \leq 150^o$ corresponding acceptance about 92% with inner radius 103.5 mm with conical shapes to outer radius 874 mm. No wall is inside for low transverse momentum tracks efficiency by minimizing the material thickness. Drift chamber compose of 3 kind of superlayer type which is axial wire detector, stereo wire detector and cathode strip detector. Wire detector superlayer

compose of 2 to 5 signal layer surrounded by field wire or cathode as Fig. 2.8 for constant electric field environment.

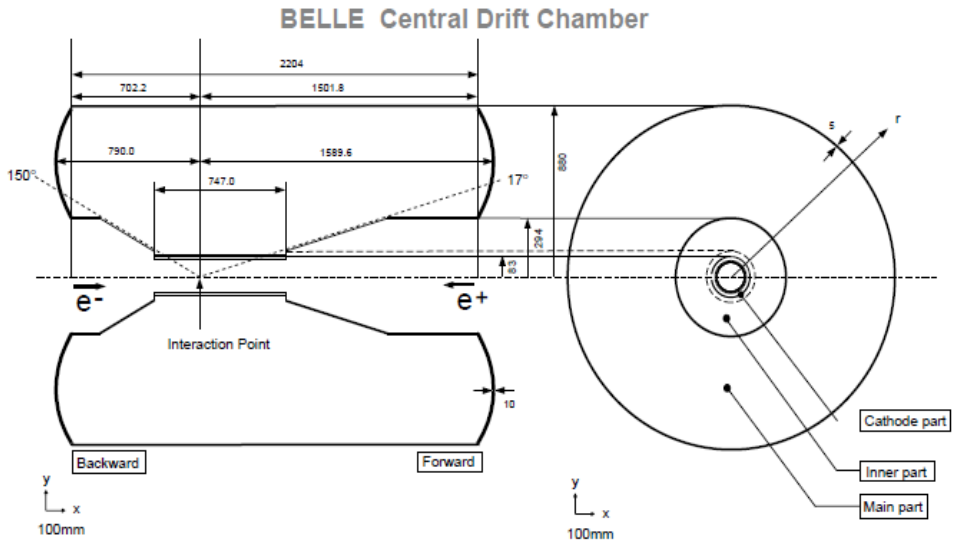

Figure 2.7: Overview of the CDC structure. The lengths in the figure are in units of mm. [39]

The chamber has 50 cylindrical layers with 8400 drift cells. For individual drift cells are nearly square (except inner three) which have a maximum drift distance between $8 \sim 10$ mm with length of one square is $15.5 \sim 17$ mm. For avoiding radiation damage, elecric field at surface of the aluminum field wire(126 μm) is less than 20 kV/cm. The sence wire are gold plated tunsten wire of 30 μm to maximize the drift electric field.

Inner most superlayers are three cathode layers and one inserted axial wire superlayer. After arrays of cathode superlayers, axial and stereo superlayers are repeatedly arrayed with 5 layer for axial superlayer and 4 layers for stereo superlayers. Stereo angles in each stereo superlayer by maximizing the z measurement capability while keeping the gain variations along the wire below 10%. Three cathode detector have 64 strips, 80 strips and 80 strips in one sector from inside and one layer has 8 sector which divided by

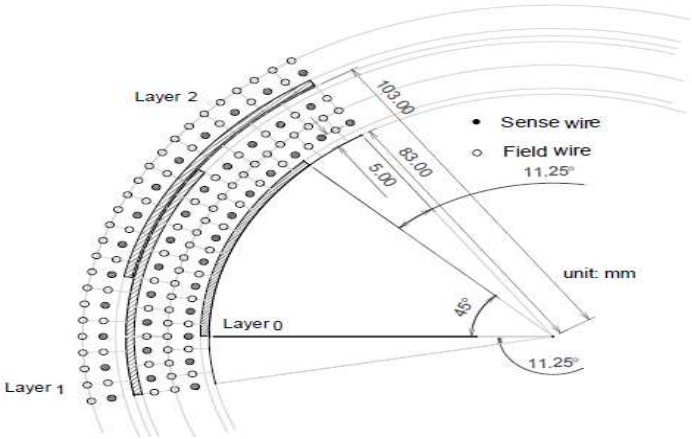

Figure 2.8: Cell structure and the cathode sector configuration. [39]

angle. Their thick is 400 μm with less than 100 μm diviation from perfect cylindrical shape. Strip width is 7.4 mm with 8.2 mm pitch.

We need incident particle scattering with gaseous molecules for detection. But we need to minimize multiple scattering to improve the momentum resolution. As a result, we need to use low-Z gas which also good for reducing synchrotron radiation background by small photo electron cross section. We use 50% helium- 50% ethane gas mixture for long radiation length (640m) and 4cm/μs drift velocity in low elecric field which is good for uniform field. Large ethane component also give good dE/dx resolution which is needed for particle identification. Detailed study for gas property done by several test chamber as Fig. 2.9.

Z dependence of Magnetic field B_z inside solenoid in CDC region is checked before installation of CDC. The nominal value of the magnetic field inside CDC is 1.5 T and non-uniformity of the magnetic field which is difference between the mininum and maximun values along the central axis is about 4%. Using corrected magnetic field by Kalman filtering method [42], spatial resolution is studied as a function of the drift distance in Fig. 2.10 **(left)** with approximately 100 μm resolution for tarcks which pass near the

Table 2.2: Configurations of the CDC sense wires and cathode strips. [39]

Superlayer type	No. of layers	Signal channels per layer	Radius(mm)	Stereo angle(mrad) or strip pitch(mm)
Cathode	1	64 (z) × 8 ϕ	83.0	(8.2)
Axial 1	2	64	88.0 ∼ 98.0	0.
Cathode	1	80 (z) × 8 ϕ	103.0	(8.2)
Cathode	1	80 (z) × 8 ϕ	103.5	(8.2)
Axial 1	4	64	108.5 ∼ 159.5	0.
Stereo 2	3	80	178.5 ∼ 209.5	71.46 ∼ 73.75
Axial 3	6	96	224.5 ∼ 304.0	0.
Stereo 4	3	128	322.4 ∼ 353.5	-42.28 ∼ -45.80
Axial 5	5	144	368.5 ∼ 431.5	0.
Stereo 6	4	160	450.5 ∼ 497.5	45.11 ∼ 49.36
Axial 7	5	192	512.5 ∼ 575.5	0.
Stereo 8	4	208	594.5 ∼ 641.5	-52.68 ∼ -57.01
Axial 9	5	240	656.5 ∼ 719.5	0.
Stereo 10	4	256	738.5 ∼ 785.5	62.10 ∼ -67.09
Axial 11	5	288	800.5 ∼ 863.0	0.

middle of wires. Fig. 2.10 **(right)** shows transverse momentum resolution dependence on momentum. The dotted point is data and line is fitted result, dashed line is expected distribution with $\beta = 1$. We can see tendency is same and resolution result satisfy what we decide as goal. Above figures are calibration data using a sample 5×10^7 cosmic ray which tracks are triggered by TOF as back to back events.

As mentioned before, cathode stripe detector is used for good spatial resolution for z direction position. Fig. 2.11 shows cathode raedout information on $\Delta z = z_{up} - z_{down}$ from cosmic ray. Left panel is without cathode readout information and right panel is with the cathode information. We can see resolution become μm order by using cathode detector. This cathode detector also important for triggering because at least two signal from cathode

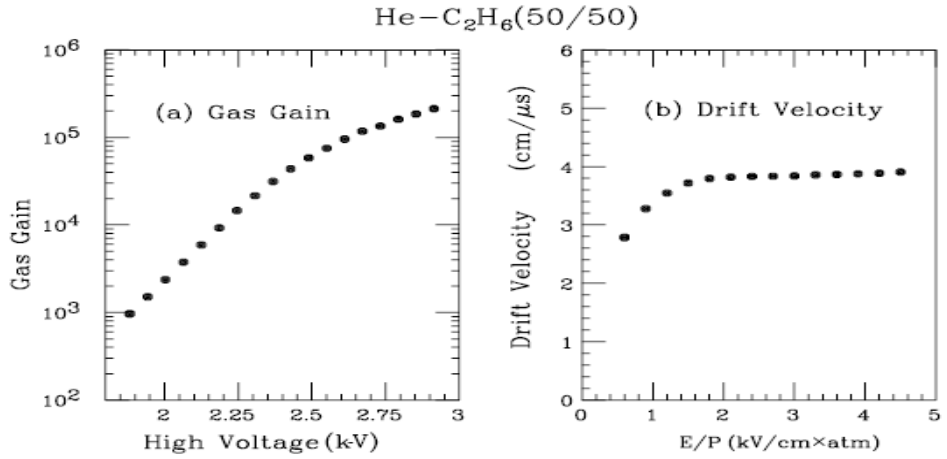

Figure 2.9: **left** The measured gas gain; **right** The drift velocity for a 50% He and 50%C_2H_6 gas mixture. [39]

detector is required.

calibration and performance

After installation into the Belle detector, high voltages and electronics parameters (bias voltage, etc) are readjusted to fit the high beam-background environment. With this corrrection, magnetic field nun-uniformity by accelerator magnet also corrected. But eventually resolution be worse compare with calibration data. Spatial resolution is obtained 130 μm for r-ϕ plane. High energy momenetum ($4 \sim 5.2$GeV/c) resolution is obtained $1.62 \pm 0.04\%$ which is studied by $e^+e^- \to \mu^+\mu^-$ events and low energy momentum (below 1GeV/c) resolution estimated by $K^0_S \to \pi\pi$ decays with the FWHM value is $7.7 MeV/c^2$ which is worse than $6.9 MeV/c^2$ by MC prediction.

For estimate dE/dx for each track, largest 20% which is landau tail is discarded and truncated-mean value is used. Fig. 2.12 shows $\langle dE/dx \rangle$ distribution for $\log_{10}(p)$ with πs, Protons, Kaons and electrons. Momentum from 0.4 to 0.6GeV/c has good resolution which was measured as 7.8% but

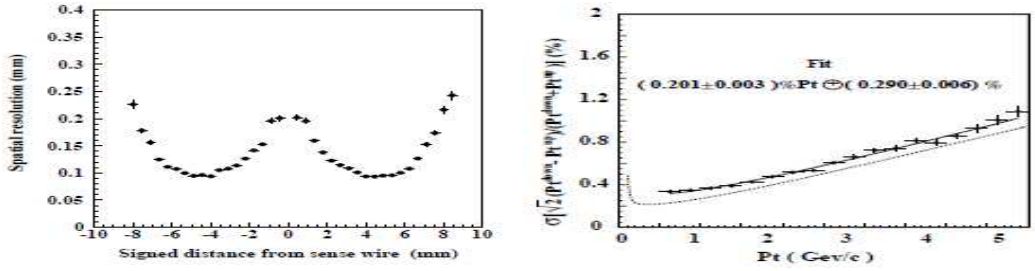

Figure 2.10: **left)** Spatial resolution as a function of the drift distance; **right** p_t dependence of p_t resolution for cosmic rays. The solid curve shows the fitted result($0.201\%\ p_t \oplus 0.290\%/\beta$) and the dotted curve ($0.118\%\ p_t \oplus 0.195\%$) shows the ideal expectation for $\beta = 1$ particles. [39]

electrons from Bhabha events with high momentum has 6% resolutuion for $(dE/dx)/(dE/dx_{expect})$. As figure, we can seperate π to kaon $\geq\ 3\sigma$ up to 0.8GeV/c and 2σ above 2.0GeV/c. But we can't seperate between two momentum region. This $\langle dE/dx \rangle$ distribution is corrected for • gain variations between cells; • drift distance depedence (due to impurities in the gas); • z-position dependence (the wire configuration in a cell is z-dependect); • dependence of the gas gain on the energy deposited, and the dip angle between track and wire (e.g. a large signal and small dip angle lead to gas gain saturation); • the dependence of the sense wire voltage (and hence the gain) on the current drawn; Figure looks not good enough for Particle identification for all momentum region and ACC light yield and TOF detection need to be add for identification.

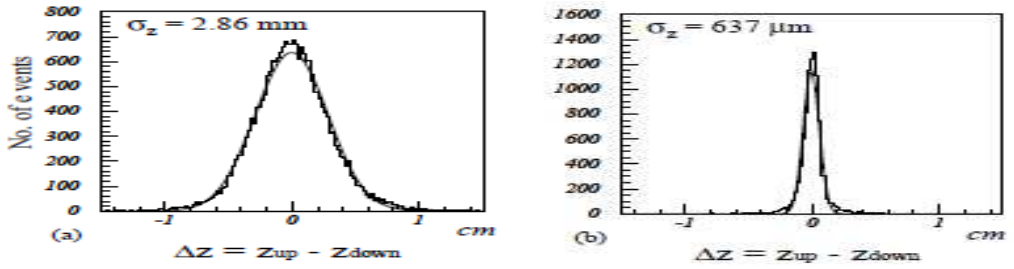

Figure 2.11: The effect of the cathode readout information on $\Delta z = z_{up} - z_{down}$ for cosmic ray tracks: **left)** without and **right)** with the use of cathode information in tracking, respecively. [39]

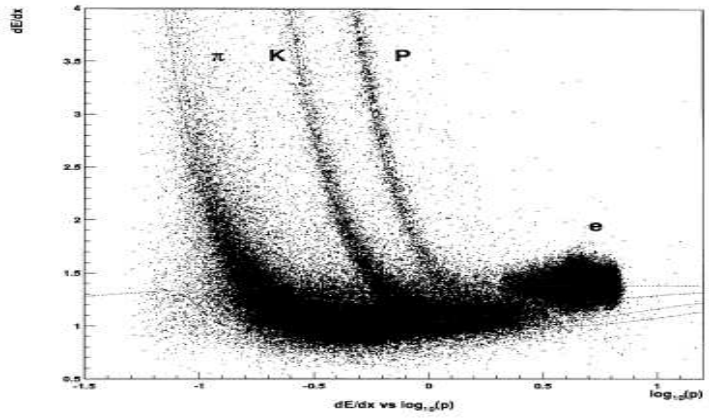

Figure 2.12: Truncated mean of dE/dx versus momentum observed in collision data. [39]

2.2.5 ACC

ACC is silica Aerogel Cerenkov Counter system which detect Cherenkov radiation generated by incident particles in silica aerogels which have refractive index value more than 1. As on and off system of particle identification, it will be used with dE/dx measurements by CDC and time-of-flight measurements by TOF. When the incident particle passes through a dielectric medium with velocity faster than light, the molecules be polarized and turn back with emission of radiation. This radiation is cherenov radiation. As like sonic shock wave, conical shape angle of cherenkov radiation from incident particle track can be used for detecting particle velocity. But in here, we only use small cubic silica aerogel for particle identification by threshold effect of cherenkov radiation. With simple formula $v_{particle} \geq c/n$ (n = index of refraction), particle which faster than light in medium will give cherenkov light and slower one will not give any radiation.

detector

Silica Aerogel Cerenkov Counter system compose of Barrel ACC and Endcap ACC which have different designed module. totally 960 counter modules segmented into 60 cells in the ϕ direction and 228 counter modules arranged in 5 concentric layers for the foward end-cap region. Fig. 2.13 shows the side-view of ACC, TOF with darker color and CDC, ECL are also shown with lighter color.

Every ACC detector point to IP position with covering $17^o \leq \theta \leq 127^o$ smaller than CDC because of no ACC in backward. One module has $12 \times 12 \times 12\ cm^3$ dimension silica aerogel which is composed of 5 tiles with 0.2 mm think and this cubic medium covered by goretex and alulminum container. Goretex reflector is used for correcting light and aluminum is used for containing. Fine mesh-type photomultiplier tubes are selected which are operated in a 1.5T magnetic field. For covering angle without gap, different design is used in

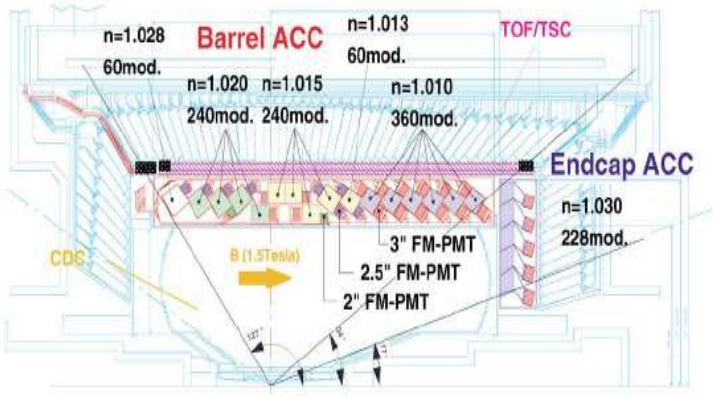

Figure 2.13: The arrangement of ACC at the central part of the Belle detector. [39]

barrel ACC and Endcap ACC as Fig. 2.14.

Figure 2.14: Schematic drawing of a typical ACC counter module: (left) barrel ACC (right) endcap ACC [39]

Most important thing is using correct refractive index of silica aerogel (SiO_2 with more than 95% porosity) as thresold for high energy particle which is not well distinguished by CDC. For distinguish π and kaon with momentum near 1GeV/c region which can't cover well by CDC (CDC has good resolution below 0.8GeV region), the refractive indeces are selected between 1.01 and 1.03 which can cover $1.2 \leq p \leq 3.6 GeV/c$ momentum region. Refractive indeces are selected depends on polar angle. Though we select aerogel with refractive index, we also need to check transmission

for efficiency. With function $T = T_0 \exp(-d/\Lambda)$, where T_0 and T are the incident and transmitted light intensity and Λ is transmission length. In sample test, 400 nm wave length gives 25 mm to 46 mm transmission length and longer wave length shows more transmission length. After transmission to end of aerogel, cherenkov light which pass the borosilicate glass window in FM-PMT(fine-mesh photomultiplier tube) is absorbed to photo-cathode with emission of electron by 25% efficiency. This electron make avalanche in fine-mesh dynode with gain 10^8 to anode for HV values(<2500 V). Magnetic field of 1.5T and degree of field direction efficiency decrease while resolution be higher.

calibration and performance

The performance of prototype ACC has been tested by $\pi 2$ beam line at KEK-PS. For 3.6GeV/c π and proton beam, aerogel counter with n = 1.015 shows Fig. 2.15 distribution. In here, left panel shows pulse-height distribution without magnetic field and right panel shows distribution with 1.5T magnetic field. Number of photo-electron N_{pe} is measured to be about $N_{pe} = 20$. π and protons are clearly seperated by more than 3σ. Because π velocity is large enough to generate cherenkov radiation as GeV order velocity but kaon or proton need to have higher momentum. So we can distinguish π, election and μ compare with proton and kaon.

After installation into the Belle detector calibration was carried out using cosmic-ray and more careful calibration has been performed with μ-pair events. The light yield range from 10 to 20 photoelectrons for the barrel ACC and from 25 to 30 photo-electrons for the end-cap ACC which is high enough for π and kaon distinguish. Fig. 2.16 shows observed Bhabha events and $K^{\pm}$ candidates in hadron events after callibration. Painted histogram is Monte Carlo and it agree well with dotted real data histogram. It shows clear seperation between high energy electrons and low energy kaons.

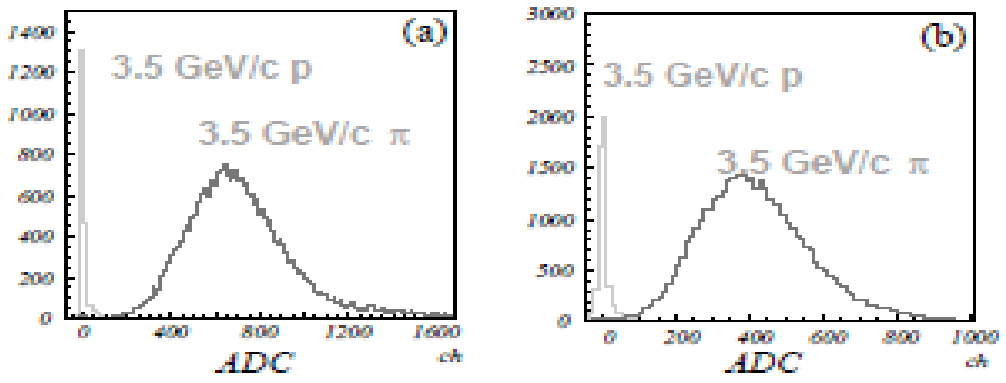

Figure 2.15: Pulse-height spectra for 3.5GeV/c πs (above threshold) and protons(below threshold) obtained by a single module of ACC in (left) non-magnetic field, (right) a magnetic field of 1.5T. Silica aerogels with n = 1.015 were stacked to form the module. [39]

2.2.6 TOF

TOF is a Time-Of-Flight detector system which is used for measuring exact time of particle passed. A plastic scintillation counter is installed barrel of Belle detector after ACC with r = 1.2 m. Measurement of exact arrival time in about 1.2 m with momentum and track estimation by CDC, we can estimate mass of particle and it can be used particle identification. This particle identification assume particle which is detected generated in collision point. 100 ps time resolution for PID of particle momenta below about 1.2GeV/c is goal of TOF and this momentum is gap of CDC and ACC particle identification region. Even though TOF only have barrel part which cover small angle compare with ACC and CDC, a monte carlo study expect TOF can cover 90% of particles from $B\bar{B}$ events. In addition, TOF provide fast timing signals for the trigger system to generate gate signals and stop signals for ACD and TCD. TOF module (not only TOF counter but also TSC (trigger scintillation counter)) keep the rate of trigger signals below 70kHz

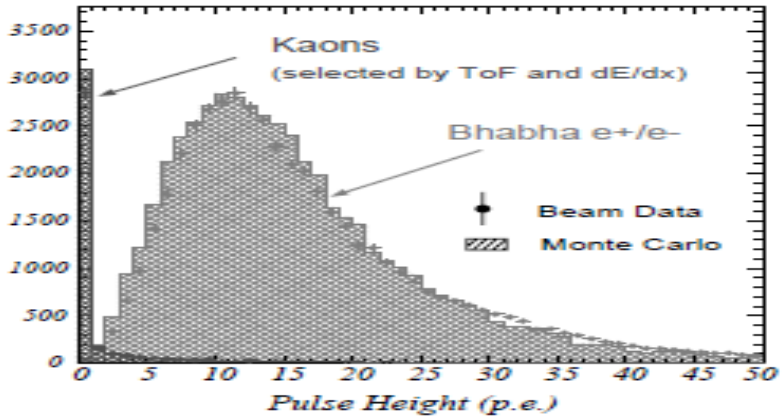

Figure 2.16: Pulse-height spectra in units of photo-electrons observed by barrel ACC for electrons and Kaons. Kaon candidates were obtained by dE/dx and TOF measurements. The Monte Carlo expectations are superimposed. [39]

for avoiding pile-up.

detector

Total 64 TOF systems in the ϕ direction are installed in barrel part with covering $34^o \geq \theta \geq 120^o$ with radius of 1.2m. One TOF system consists of 2 trapezoidally shaped TOF counter and 1 TSC counter with a 1.6-cm intervening radial gap. So totally 128 TOF and 64 TSC is in. Fig. 2.17 is figure of one TOF module. TSC counter has 0.5 cm thickness, 12 cm width with one PMT in backward connected by light guide which is used for triggering. Each TOF counter has 4 cm thickness, 6 cm width with two PMT in both side without light guide. The gap between TSC and TOF is used for reducing photon conversion backgrounds which will suppressed by gap. By taking coincidence between TSC and TOF, electrons and positirons by photon conversion are subtracted.

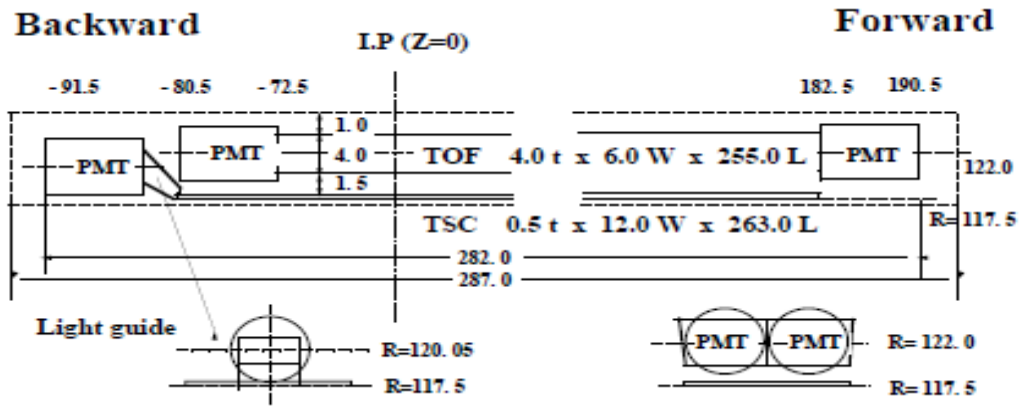

Figure 2.17: Dimensions of a TOF/TSC module. [39]

With FM-PMTs like ACC, plastic scintillator (BC408, Bicron) is used with thin film for light tightness. Because of 255 cm long length, the attenuation legth and light yield are important. With design strategy: • use of fast scintillator with an attenuation length longer than 2 m, the average attenuation leght was 3.9 m and light propagation velocity was 14.4 cm/ns. The other design strategy was • use of photo-tubes with large-area photocathodes to maximize photon collection and • elimination of light guides to minimize the time dispersion of scintillation photons propagating in the counter.

perfomance and calibration

Before installation, TOF module was tested using the $\pi 2$ beam line of KEK-PS. In test, a time resolution of about 80 ps was obtained over the whole counter. Because timing is related not only to the flight time but also to the rise time and time-walk, it is corrected. When we get exact time from installed TOF, we need to correct time with • a 10% degradation of the intrinsic resolution caused by the 1.5T magnetic field as observed in a beam test. • a 20 ps contribution due to the 4 mm beam bunch length and jitter in the RF signal used as the reference time. • a 20 ps contribution from time

stretcher readout electronics. The time shift by large deposit energy which exceed the leading-edge discriminator threshold sooner is time-walk. Easily speaking, change of pulse distribution in edge by deposit energy is time-walk. Eq. 2.3 is used for precise time measurement.

$$T_{obs}^{twc} = T_{raw} - (\frac{z}{V_{eff}} + \frac{S}{\sqrt{(Q)}} + F(z)). \tag{2.3}$$

In equation second term is hit position dependence with V_{eff}(:effective velocity of light in the scintillator), third term is time-walk correction with S(:coefficient of time walk), Q(:charge of the signal). Last therm is z position dependent correction and all free parameters determined by predicted time from CDC hits.

Calibration is done with μ-pair events and using hadronic decay sizable δt is studied. Deviation is depends on particle and momentum(eventually come from velocity) as Fig. 2.18 **(left)**. This figure shows averaged data over all counters with z. Right panel shows the mass distribution for each track in hadron events. Mass is calculated by Eq. 2.4. By the resolution of time and momentum, mass deviation looks not small but enough for particle identification which has mass difference like $\sim 100MeV$. The sigma value depends on momentum and 0.6 GeV/c momentum particle shows 6 σ deviation between k/π and high momentum shows be decrease as 2 σ.

$$M^2 = (\frac{1}{\beta^2} - 1)P^2 = ((\frac{cT_{obs}^{twc}}{L_{path}})^2 - 1)P^2. \tag{2.4}$$

2.2.7 ECL

ECL is electromagnetic Calorimetry for detection of photons. Although this detector important B-meson decay or π^0 decay to γ, it also can helpful for studying anti-neuteron. In H-dibaryon search channel, if H-dibaryon will weakly decay near $2m_\Lambda$ then it will decay to $\Lambda p\pi$, Λn channel, and etc. Although it's hard to detect and to identify neuteron using this small crystal,

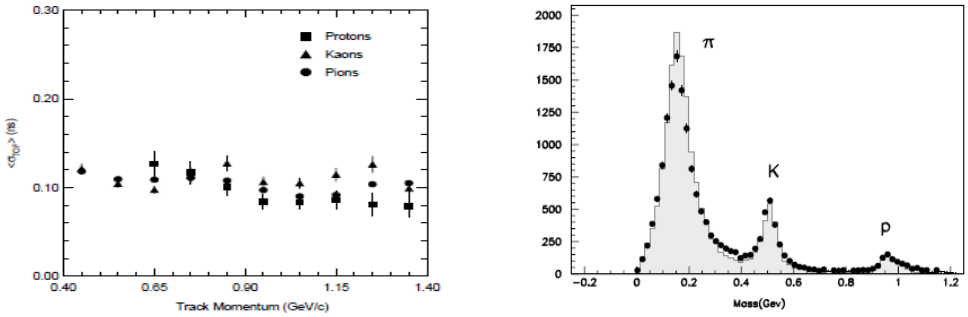

Figure 2.18: **Left:** The TOF resolution, averaged over all counters and z, as a function of momentum for each hadron species. **Right:** Mass distribution from TOF measurements for particle momenta below 1.2 GeV/c.

anti-neuteron can lose whole energy inside crystal and show cluster. But in here, we will focus on basic task of ECL and performance. The other task of ECL is Particle identification of electron. Differ with other hadrons which is not loose much energy inside crystal, electron has big energy deposit and shows cluster.

Fig. 2.19 shows overall configuration of ECL. The ECL cover from forward to backward by three part as forward end-cap, barrel, and backward end-cap. Barrel section has 3.0 m length and 1.25 m inner radius. End-cap depart from IP-point to z = +2.0 m and z = -1.0 m. Totally 8736 crystal counter has 43 tons weight. Detail is in Table. 2.3

Table 2.3: Geometrical parameters of ECL.

Item	θ coverage	θ seg.	ϕ seg.	No. of crystals
Forward end-cap	$12.4^o \sim 31.4^o$	13	48 $\sim$ 144	1152
Barrel	$32.2^o \sim 128.7^o$	46	144	6624
Backward end-cap	$130.7^o \sim 155.1^o$	10	64 $\sim$ 144	960

Using tower like shape crystal, crystal points almost to the IP-point with

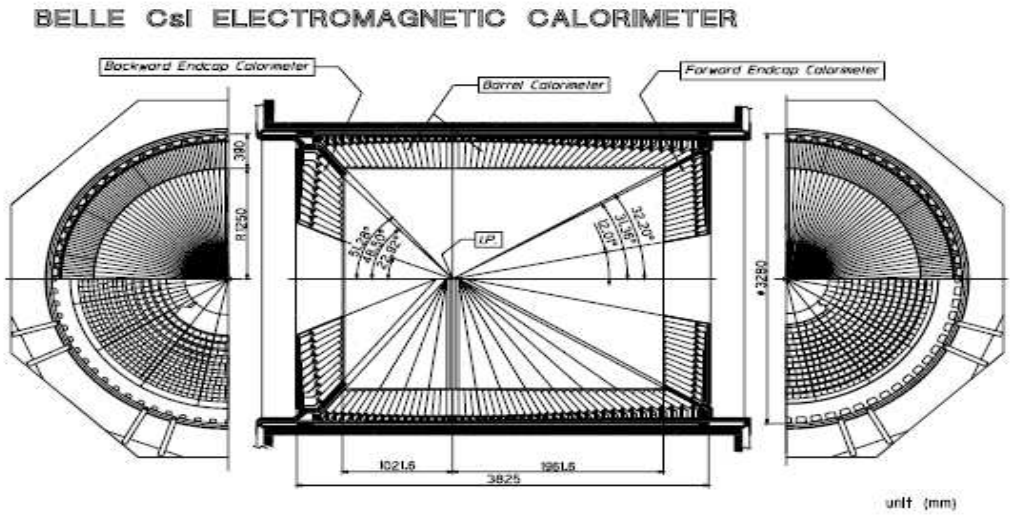

Figure 2.19: Overall configuration of ECL.

small tilt angle of $\sim 1.3^o$ (barrel), $\sim 1.5^o$ to $\sim 4^o$ (end-cap) to avoid photons escaping through the gap of crystal. Gap between end-cap and barrel, which is needed for pathway for cable and room for supporting, lose 3% of the total acceptance. One crystal size is determined for approximately 80% of the total energy deposition and for containing energy resolution and oppositly small enough position resolution of two photon from π^0 Each crystal is wrapped in a diffuse reflector(Goretex teflon) and back end is attached by two silicon PIN photo-diode (Hamamatsu S2744-08).

calibration and perfomance

Calibration is done by cosmic ray in the measuring system called a "cosmic-ray calibration stand" which has 8 layer of drift chambers for tracking and two layers of scintillation counters for triggering and timing. Each crystal counters was calibrated and radiation hardness was checked. Also beam test is done by electron and π beams at the $\pi 2$ beam line of 12-GeV KEK-PS and photon beams produced at the ROOK-1M facility of the Budker Institute of

Nuclear Physics (BINP).

Using the π and electron beams, we can estimate position resolution and Particle identification of π and electron. The position resolutions were determined from the impact position on the matrix from summed and weighted energy deposit and track from CDC chamber and gave 3.6 mm for 2.0 GeV/c and 5.8 mm for 0.5 GeV/c electrons. By the difference of the energy deposit, we can distinguish electrons and πs. Fig. 2.20 **(left)** shows energy deposit summed over 25 crystals for 1GeV/c electrons and πs. We also can see difference of π^+ and π^- because of the cross-section difference. With the defined electron region as $\pm\ 3\sigma_e(\sigma_e$ is energy resolution), the misidentification probability is found to be less than 1% above 2 GeV/c and less than 7% below 2 GeV/c as Fig. 2.20 **(right)**.

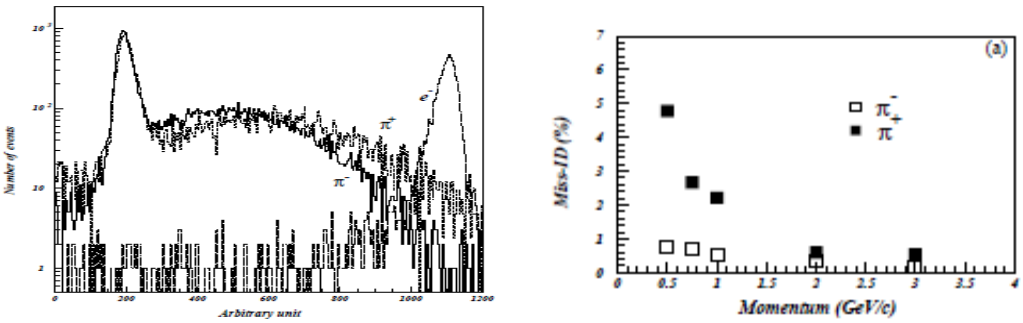

Figure 2.20: **Left:** Distribution of the energy deposit by electrons (dotted histogram), by positive πs (dashed histogram) and by negative πs (solid histogram) at 1GeV/c. **Right:** Probability to misidentify a π as an electron.

Using photon beams range from 20 MeV to 5.4 GeV, the energy resolution is estimated by three ways. One way is using E_9/E_γ or E_{25}/E_γ ratio, other ways are using compton distribution and bremsstrahlung distribution. Details are in [39]. Using three ways, quadratic sum of resolution is as follows:

$$\frac{\sigma_E}{E(GeV)} = \frac{0.0066(\%)}{E} \oplus \frac{1.53(\%)}{E^{1/4}} \oplus 1.18\% \tag{2.5}$$

for the 3×3 matrix sum, and

$$\frac{\sigma_E}{E(GeV)} = \frac{0.066(\%)}{E} \oplus \frac{0.81(\%)}{E^{1/4}} \oplus 1.34\% \tag{2.6}$$

for the 5×5 matrix sum.

After calibration, performance is checked. Using large number of the Bhabha and $\gamma\gamma$ events, the energy resolution was achieved to be 1.7% for the barrel ECl, and 1.74% and 2.85% for the forward and backward ECl. Fig. 2.21 shows two-photon invariant mass distribution and energy resolution has been achieved to be 4.9 MeV(π^0) and less than 10 MeV(η).

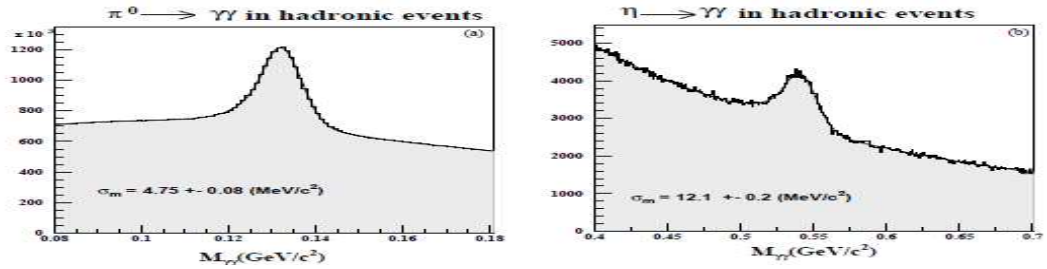

Figure 2.21: Two photon invariant mass distribution for hadronic events **(left)** in $\pi^0 \to \gamma\gamma$ and **(right)** in $\eta \to \gamma\gamma$ where each photon energy was required to be greater than 30 MeV in the barrel region.

2.2.8 KLM

KLM is K_L and Muon Detection system with high efficiency over a broad momentum range greater than 600 MeV/c. In outside of superconducting magnet, it cover an angular range from 45^o to 125^o in the polar angle and the end-caps in the forward (backward) directions extend to 20^o (155^o). Fig. 2.22 shows side view of Belle detector and end-cap KLM is opend. KLM is in iron Yoke and consists of 15 alternating layers of charged particle detector as RPC (glass resistive pate counter) in barrel (14 in end-caps) and 14 layer of

4.7 cm-thick iron plate. This iron plates provide 3.9 interaction lengths of material.

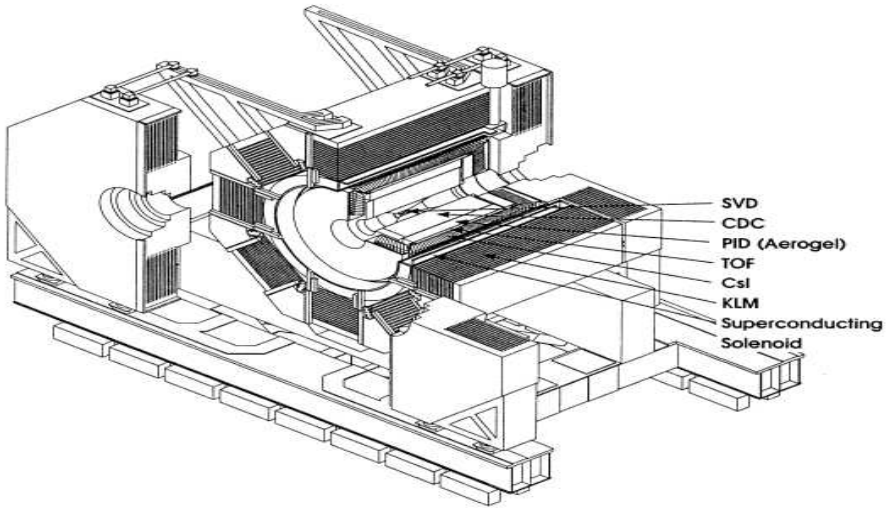

Figure 2.22: The Belle detector side view.

The K_L that interacts in the iron or ECL (0.8 interaction length) produces a shower of ionizing particles. This shower gives position information but not enough use for energy measurement. KLM also allow discrimination between muon and other charged hadrons by relatively small deflection of muon.

The RPC is Resistive plate counter which have two parallel plate electodes whith high bulk resistivity ($10^{10}\Omega\, cm$) separated by a gas-filled gap. Streamer which can be generated by free charge particle transvering gas as insulating material with high voltage difference and that results in a local discharge of the plates. The discharge induces on signal on external pickup strips and give location and time information.

Fig. 2.23 (2.24) shows schematic diagram of the barrel (end-cap) of RPC with internal spacer **(left)** and cross section of a KLM super-layer **(right)**.

With dielectric form and ground plane for insulation, double-gap RPC with two direction strips cathode provide 3-dimensional space point for particle tracking.

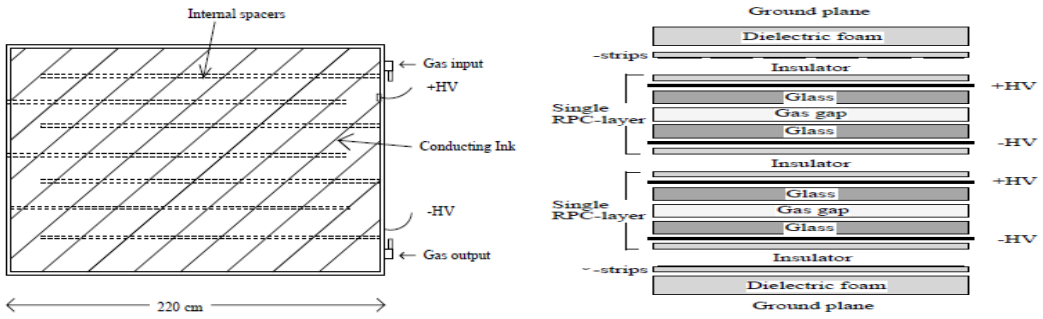

Figure 2.23: **Left:**Schematic diagram of the internal spacer arrangement for barrel RPC **Right:** Cross section of a KLM super-layer.

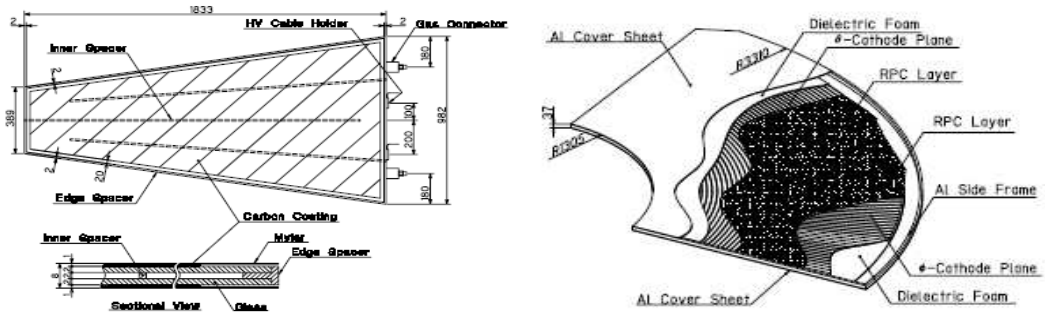

Figure 2.24: **Left:** Schematic diagram of the internal spacer arrangement for end-cap RPC **Right:** Cut-away view of an end-cap of a KLM super-layer.

The internal spacer were designed with concave regions were extruded to an accuracy of $\pm$ 0.05 mm. The outer surface of glass was coated by india ink to distribute the high voltage with resistivity of $10^6 \sim 10^7 \Omega/square$. As you can see right panels, RPCs are sandwiched between orthogonal θ and ϕ pickup-strips and these two RPC were insulated. Each barrel module has 48 z-pickup strips perpendicular to the beam direciton. The smaller 7

superlayers closest to the interaction point have 36 ϕ strips and the outer 8 superlayers have 48 ϕ strips. Each end-cap module has 10π shaped RPCs and one superlayer module has 96ϕ and 46θ pickup-strips.

perfomance

With averaging efficiency over 98% for operating a high voltage 4.3 (4.2)kV/mm, signal threshold of 40 (70)mV is choosed for the barrel (end-cap) modules. Cosmic rays were used for checking and for giving set of operation condition. A penetrating muon generates the average hits of 1.4 strips and 1.9 strips per layer in the baerrel and end-cap modules. With this high efficiency, spatial resolution of the modules is shown in Fig. 2.25 **(left)**. This residual distribution is difference between meaesured and predicted value from adjacent layers. For strips, standrard deviation is 1 $\sim$ 3 cm, respectively.

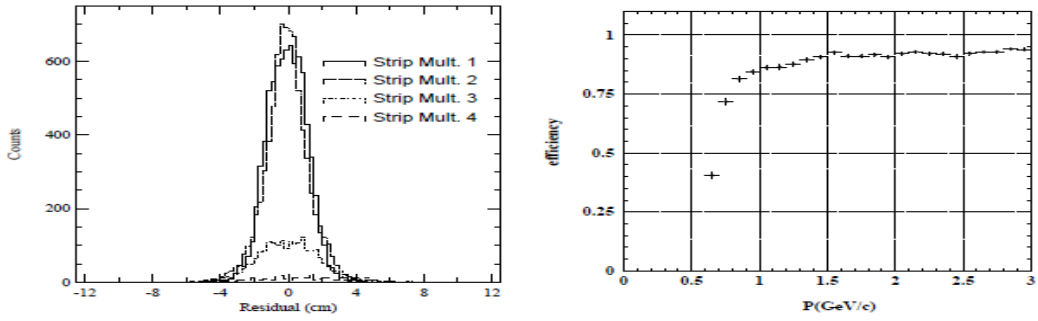

Figure 2.25: **Left:** Spatial resolution of a super-layer of KLM **Right:** Muon detection efficiency versus momentum in KLM.

Important performance is K_L detection efficiency and μ detection efficiency. K_L must shows cluster in KLM without signal or track information in CDC. By excluding within 15 degreees of particle track, average number of K_L clusters per event 0.5 is getted and this value agree with Monte Carlo simulation.

About μ detection, below 500 MeV/c momentum μ can't reach KLM.

Fig. 2.25**(right)** shows efficiency distribution versus momentum. For above 500 Mev/c, fake rate is in figure even though 0.66 likelihood cut is used. A fake rate decrease as momentum increase and above 1.5GeV/c,we have less than 5% fake rate with 90% efficiency for μ identification.

Chapter 3

Data analysis

The $\Xi_5^{--} \to \Xi^-\pi^-$ channel is very similar in topology to that for $\Xi^{*0}(1530) \to \Xi^-\pi^+$, we use the inclusive $\Upsilon(1S) \to \Xi^{*0}(1530)\,X$ with $\Xi^{*0}(1530) \to \Xi^-\pi^+$ as a control sample to optimize event selection requirement. With blind box in expecte signal region, we can compare background distribution of side-band between MC and real data. After studying background, with refrees agreement, we can open the blind box and search penta-quark. The selection requirement of the inclusive $\Upsilon(1S) \to \Xi^{*0}(1530)\,X$ with $\Xi^{*0}(1530) \to \Xi^-\pi^+$ control sample can be usable to $\Upsilon(1S) \to HX$ with $H \to \Xi^- p$ H-dibaryon searching channel. With this foundation, we can search H-dibaryon for totally three channel by stage.

3.1 Data samples with Hadron B(J) skim & MC samples

3.1.1 Number estimation for $\Upsilon(1S)$ & $\Upsilon(2S)$ data sample

For June 11 $\sim$ 30, 2008, Belle detector had run for taking data samples of $\Upsilon(1S)$ with experimental number Exp 65. In this period, totally 5.712 fb^{-1} data was taken for $\Upsilon(1S)$ resonance with CM energy $\sqrt{s}$= 9.46 GeV and 1.802 fb^{-1} data taken for continuum sample with CM energy $\sqrt{s}$= 9.43 GeV. Detailed Luminosity plot for run number can be checked by Fig. 3.1.

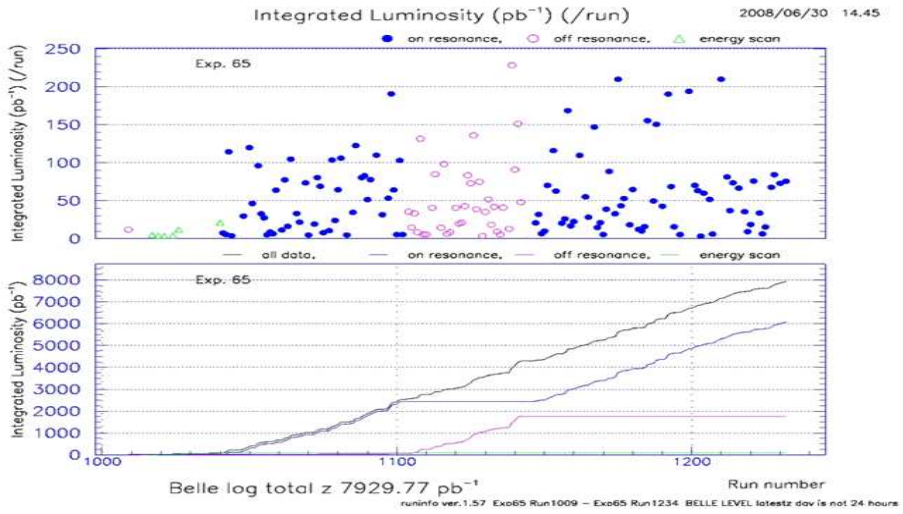

Figure 3.1: Integrated Luminosity of $\Upsilon(1S)$ run from Bhabha events

For two period, Belle detector had run for taking data samples of $\Upsilon(2S)$. First run was for December 9 $\sim$ 22, 2008 with experimental number Exp

67 and Second run was from October 27 to November 30 with experimental number Exp 71. Totally 24.7 fb^{-1} data samples are taken for $\Upsilon(2S)$ resonance with CM energy $\sqrt{s}$ = 10.02 GeV and 1.692 fb^{-1} data samples are taken for continuum sample with CM energy $\sqrt{s}$ = 9.993 GeV as in Fig. 3.2. This is world best luminosity for $\Upsilon(1S, 2S)$ resonance.

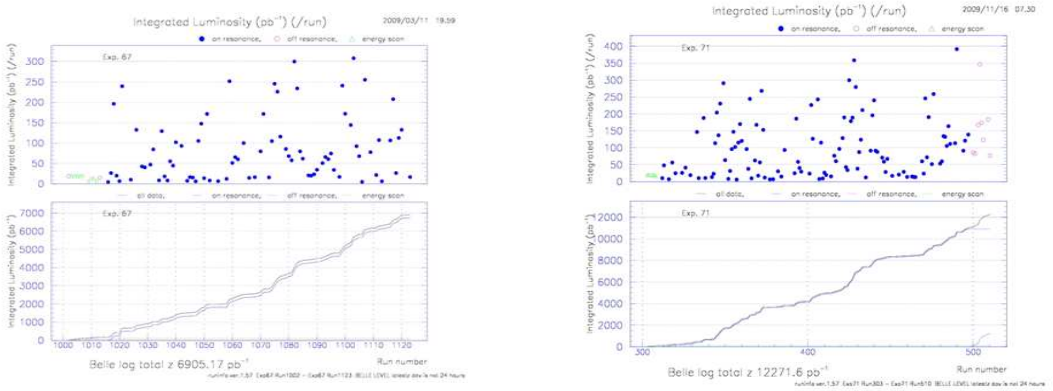

Figure 3.2: Integrated Luminosity of $\Upsilon(2S)$ run from Bhabha events about **(left)** exp 67 **(right)** exp 71.

For counting real number of $\Upsilon(1S, 2S)$ bottomonium, we can check cross section in Fig. 3.3 [43]. Roughly $\sigma_{\Upsilon(1S)}$ = 20nb and $\sigma_{\Upsilon(2S)}$ = 7nb. So expected number is about 100M and 170M for $\Upsilon(1S)$ & $\Upsilon(2S)$.

This is just instant view and more precise measurement done inside BELLE by studying hadron or lepton pair decays and comparing with continuum BG [44]. Measured $\Upsilon(1S)$ number is (102 ± 2)M and $\Upsilon(2S)$ number is (157.8 ± 3.6)M.

3.1.2 Hadron B(J) skim

Because beam energy error is in few MeV, we don't need to worry about experiment itself but we need to care about several production which is not linked to our physics topic study like Bhabha scattering, pair annihilation,

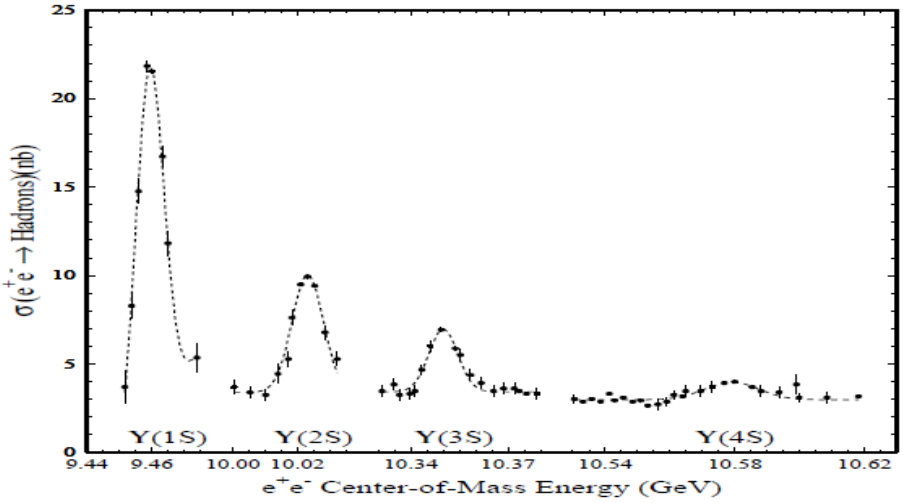

Figure 3.3: e^+e^- cross-section measured by CLEO and CUSB showing the masses of the Υ resonance. There is an underlying continuum of $e^+e^- \rightarrow \gamma^* \rightarrow q\bar{q}$ events. Then there is a dramatic increase in the number of events observed when producing the $^3S_1$ states of $b\bar{b}$ bound state system. The observed resonances are the n = 1,2,3, and 4 radial excitations.

lepton pair production, non-resonance hadron productions (Two jet events) and etc, though we want to only see bottomonium resonance to hadron production. These other processes have high enough cross section compared with resonance hadron production as Table 3.1 for $\sqrt{s}$ = 10.58GeV. As shown, even few % of QED and Bhabha events make size of data be fat. Not only several process background, beam gas events which generated by gas molecules in beam chamber of interaction with beam is big background problem for study. This background is hard to model with Monte Carlo and has run dependance. So it's hard to study every person by themselves.

In this complicated situation, skim selection can choose needed process

Table 3.1: Cross section for various processes in e^+e^- collisions at $\sqrt{s}$ = 10.58 GeV. QED refers to Bhabha and radiative Bhabha process. [45]

Process	σ(nb)
$b\bar{b}$	1.1
$q\bar{q}$(q = u, d,s ,c)	3.3
$\tau^+\tau^-$	0.93
QED ($25.551^o < \theta < 159.94^o$)	37.8
$\gamma\gamma \rightarrow q\bar{q}$ (ω >500 MeV)	11.1

and reduce beam gas events. To select hadron production events from a mountain of detected data with several process, we need to give simple selection criteria named skim. Belle have many kind of official skim which select events with simple cuts for specific physics mode like Hadron B(J) skim for decay to hadrons, TauPair skim for tau pair and LowMuit skim for two-photon, etc. To study inclusive baryon decay channels, we select Hadron B(J) skim as basic selection. Eventually we also need to remove non-resonance hadron production so called continuum event which is $e^+e^- \rightarrow q\bar{q}$ where q = u,d,s and c. But it will deal with continuum data samples.

To select hadronization events with high efficiency and to remove other events, Hadron B(J) skim is used. Hadron B(J) skim define Hadron event by cut of Track multiplicity, Visible energy, Calorimeter Energy sum, Momentum valance, Primary Vertex Position, etc. Using "good track" and "good cluster" which is satisfied momentum, impact parameter cut, ECL energy and angle cut, all quantities are computed. At lease, 3 good track need to exist and visible energy which is sum of good track momentum and good photon energies be more than 10% of CM energy. Efficiency of hadronization events is 99% and non-hadronization events is 2%. Detail cut values are in [45]

3.1.3 BELLE library

With progress of detecting software, BELLE collaboration make library setting which is used for reprocessing raw data set by physics analysis data set. We call this library setting as Belle level. Because the change of mechanism and cut, each experiment has different Belle level depends on run year. The data set which have run year dependent library is called caseA. While caseB is reprocess data after end of Belle detector run with latest library (as of Feb. 9. 2010). This adapted to after Exp 31 to Exp 71. (Before data-set is too old to reprocess using caseB library)

The difference between caseB and caseA for data-set is caseB has that tracking way is changed, SVD-self tracking is added and ECL threshold energy which depends on θ angle is turn on. Because of these changes, caseB has more higher particle track number and show different feature compare with caseA. My analysis begin in 2010 year, so i used caseA data-set for $\Xi^{*0}(1530)$ resonance analysis. After $\Xi^{*0}(1530)$ channel i change data-set to caseB. Data set what i use for analysis is Exp 65, Exp 67 and Exp 71 of on-resonance data and from Exp 31 to Exp 65 of off-resonance data. Because Exp 71 use caseB library, we analysis caseA $\Upsilon(1S)$ data set (Exp65), caseB $\Upsilon(2S)$ data (Exp 67) and caseB $\Upsilon(2S)$ data (Exp 71). We decide cut requirement using optimized FoM to caseA library but even we use same cut for caseB library data, there's no bias or significant problem.

3.1.4 MC generation

event generator

To study signals and backgrounds without bias and to precisely estimate efficiency and errors, large sample of simulated $\Upsilon(1S) \rightarrow$ hadron decays was produced using the PYTHIA event generator [47]. Module what is used is EvtGen which is general MC generator in Belle. Detail of EvtGen is destribed

below. EvtGen is event generator designed for the simulation of the physics of B decays. EvtGen is initiated by CLEO and developed/maintained by BaBar for precision simulation of

- Angular correlations in sequential decays
- CP violationg decays
- Resonant substructure
- Specialized matrix elements for rare decays.

This EvtGen is merged with PYTHIA which is tuned by LHC data samples. Although EvtGen is precisely studied tool for $\Upsilon(4S)$'s B-decay, what eventually used is PYTHIA for studying hadronization of $\Upsilon(1S, 2S)$. This PYTHIA is standard tool for generation of high energy physics, comprising a coherent set of physics models for the evolution from a few-body hard process to a complex multi-hadronic final state. [47] PYTHIA can cover $pp,\ \bar{p}p,\ ee, and\ \mu\mu$ collision as hard processes. With process of Parton showers algorithm, Multiple interaction machinery and hadronization framework, PYTHIA quite well distribute bottomonium decays and continuum data. Because of lack of data, branching fraction or ratio of hadrons can be differ little even though decay table from PDG is used.

detector simulation

As detector description and simulation tool, we used GSIM tool based on GEANT3 which is general standard in BELLE. The GEANT program describes the passage of elementary particles through the matter, originally designed for the high energy physics experiments. Using same design of BELLE detector and generated particle information from EvtGen, GSIM simulate data which depends on belle library. (caseA or caseB, and more seperated libraries.) As mentioned HadronB(J) skim, we can't reproduce

background perfectly because of many effect which is difficult to understand and to estimate. So Belle use beam background itself on the simulated MC event by gsim which named addbg which is made from the real random-triggered data.

signalMC generation

We can generate baryon or meson particle in MC by adding information of particle property and decay table. But what we focus on is penta-quark and H-dibaryon composed of 5, 6 valance quark. It's not easy making signalMC with this hadron states. So we change $\Xi^{*0}(1530)$ resonance property in particle table. After changing mass, width, lifetime and spin-parity, we generate signalMC. What we need to study using this signalMC is efficiency and resolution not branching fraction. So no bias or big discrepency are expected in this generation.

3.2 Λ selection

Extending our whole analysis from penta quark search to H-dibaryon search, first of all, we need to select Λ particle in multiple tracks. Though we can't see and measure Λ particle's kinematic information directly because of neutral charge, we can easily get huge Λ particle candidates by reconstructing p and π^- tracks. As we know, Λ baryon is composed with u,d,s quark as lightest baryon with Strangeness (-1). The Λ baryon only can decay with weak interaction with $\Delta S = 1$ to $p\pi^-(63.9\%)$ or $n\pi^0(35.8\%)$. Fraction of Λ decay follow famous $\Delta I = 1/2$ rule.

In belle detector, we use PANTHER table which is bank system for experimental values. Mdst_Vee2 is one of definded table which save extracted information of neutral particle(V0 particle) like K_s, Λ and converted γ after reconstructing 2 charged tracks using Vertex constraint fit in DST track list.

Vertex constraint fit is minimun χ^2 selection using constraint by least square method. In here, because we don't know vertex positon, i.e, mother particle's decay position, we need to give constraint using assumed position which will be decided by constraint. Using 5 track parameters (Impact parameters) which is decided by tracks and equation of motion, we can give constraint. Easily say, this table collect one (+) charged track and one (-) charged track which is satisfied equation of motion.

Without any selection criteria, $p\pi^-$ invariant mass distribution for these events is shown as the top distribution of data points in Fig. 3.4. The blue curve through the points shows the results of a fit using a Breit Wigner shape to represent the $\Lambda \rightarrow p\pi$ signal and a polynomial to represent the background. The fit gives a yield of $(4.52 \pm 0.01) \times 10^6$ Λs out of a total of 46.26×10^6 entries. Because Λ bound energy is apart from thereshold of m_p+m_π, we can assume linear background. Normally, we can think that because Λ baryon has life-time (ignorable width), Λ peak be gaussian shape by detector resolution. We didn't study exact region why it has more wide tail in both side, we can deduce the reason as dependece of many detector's difference efficiency for many parameters. In this kind of situation, we can use Breit Wigner or two gaussian, and Breit Wigner shows quite good fitted result. After you will see, resolution of Λ mass will be ignored by mass constraint.

Backgrounds in data make statistical error be higher and make hard to find signal. Because of multiplicity, there's huge background in M(pπ) distribution which is mis-combined. To handle Λ baryon candidates, we studied parameters of proton, π and Λ itself. To reduce backgroud, we require two kinds of cut parameter eventually. One is proton selection and the other is Λ selection. What we did for proton and π track is just give p or π's PDG mass for each charged tracks without Particle identification. Franckly we can get rough mass value by CDC and TOF detector. By exactly timeing by TOF with 100ps error and momentum information of tracks from CDC, we can calculate mass of track particle as Fig. 2.18 **(right)**. But it has very

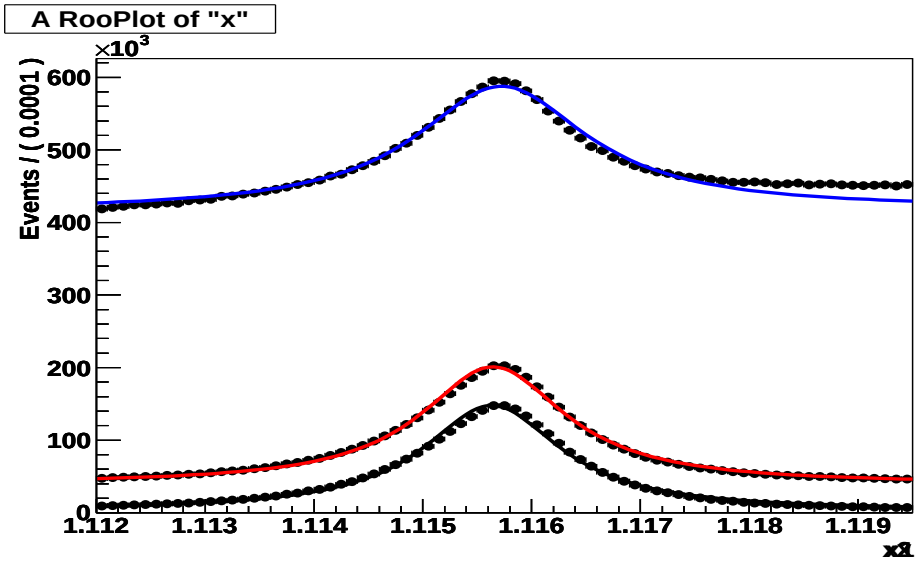

Figure 3.4: The $M(p\pi_1^-)$ distribution for selected events. The top distribution of data points includes all Λs from the DST track list; the middle distribution of points shows the events that survive the proton id requirement; the lower points show the events remaining after the goodvee=1 *or* goodvee=2 requirement. The curves are results of fits used to extract the signal yields described in the text.

big error and usable only for particle identification. So we give PDG mass value of proton, π and kaon for each particle tracks and select using PID or other ways. Because almost all charged tracks are π and there's small proton compare with π, we can expect many proton tracks in DST track table which are actually πs not protons. To subtract these πs from proton candidates, we use PID cut for proton compare with π and K by atc_pid class. PID means Particle IDentification based on the likelihood ratio comparing with signal

and background particle species as Eq. 3.1.

$$R(i|j) = \frac{\mathcal{L}_i}{\mathcal{L}_i + \mathcal{L}_j}. \tag{3.1}$$

where L_i and L_j are the product of likelihoods obtained from each detector. ($L_i = L_i^{dE/dx} \times L_i^{TOF} \times L_i^{ACC}$)

We require $R(p|\pi) \geq 0.1$ and $R(p|k) \geq 0.1$ for all positive tracks which are candidates of proton. By throwing away kaon-like and π-like track, we got more clean signal. When we choose cut values, we checked not only background rejection efficiency but also signal efficiency. According to the MC, this requirement loses very few real $\Lambda \rightarrow p\pi$ tracks. In the inclusive MC, the number of real Λ's (from the truth table) that are lost are 339 out of 12,496, a 3% loss. The M(pπ) distributions after the particle identification requirements is applied are shown as the middle distribution of data points in Fig. 3.4. When we see the distribution of PID ratio, there's three big peak in 0, 0.5 and 1 and small data only in medle region. For example, R(p|π) $\geq$ 0.1 means throw away which seems like π with 90% likelihood ratio and left which is not hard to decide proton or π.

After selecting precise proton and π, there's many background by wrong combined samples. Because there's many produced proton and π from other decays, we need to select samples which come from the same mother which is Λ. So secondly, we use the GoodVee selection criteria which is default Λ selection in BELLE [33] that makes momentum dependent selections. The GoodVee cut is consisted of 4 parameters which is named zdist, dr, dphi, fl.

- zdist : The distance of two daughter tracks at their interception position in z axis.
- dr : The minimum distance of the daughter tracks and the interaction point(IP) in x-y plane.
- dphi : The difference of the azimuthal angle of the vertex vector and the momentum vector.

• fl : the flight length of Λ candidates in x-y plane.

When we think about Λ's daughter particle tracks, we can understand these 4 parameters easily. Because two daughter tracks need to come out same position which is Λ decay position, two track's distance need to be short. By using z direction distance between two track and interception position, we can select samples which have small zdist. Almost tracks reconstructed in detector are generated from beam collision itself or unstable resonance state same as near IP position. But Λ's dauther particles tracks generated decay position of Λ which depart from IP position because of Λ's life time, so dr of these tracks are larger than others. For about dphi, if Λ generated near IP, then it is nature that momentum and vertex direction is same. But if angle is too big, we can think these events come from mis-reconstruction or by background particles. At last, normal fl values for two tracks generated in IP is almost 0, but from Λ's $c\tau_\Lambda$(life time) = 7.89 cm: if we cut out small fl value data, we can save many real Λ and through away many mis-combinations.

Belle people decide two kind cut level by checking FoM : GoodVee = 1 or GoodVee = 2. GoodVee(1) is selection criteria optimized for R(p|π) > 0.6 and GoodVee(2) is selection criteria with all charged tracks using a sample of $\Upsilon(4S)$ data and a sample of mixed $B\bar{B}$ and continuum data. Detail cut values are in Table. 3.2

Using these two cut parameters (PID, GoodVee) and other possible parameters like $c\tau_\Lambda$ and χ^2_Λ, We checked efficiency of signal and background. $c\tau_\Lambda$ distribution mentioned in here is $c\tau_\Lambda \equiv \vec{\ell} \cdot \vec{p}_\Lambda M_\Lambda / |\vec{p}_\Lambda|^2$ and $\vec{\ell}$ is the displacement between the run-dependent average interaction point (IP) and the fitted vertex position. But $c\tau_\Lambda$ and χ^2_Λ was not helpful when we check using real data. So we decide only deal with particle PID and GoodVee function. By requiring either GoodVee = 1 or GoodVee = 2, we further reduce the background under the Λ mass pick compared with PID cut only.

The black curve in Fig. 3.4 with data points is result after all Λ selection

Table 3.2: The good Lambda cuts

good Lambda Level 1				
Momentum	zdist	dr	dphi	fl
> 1.5	<12.9	>0.008	<0.09	>0.22
$0.5 - 1.5$	< 9.8	>0.010	<0.18	>0.16
< 0.5	< 2.4	>0.027	<1.20	>0.11
good Lambda Level 2				
Momentum	zdist	dr	dphi	fl
> 1.5	< 7.7	>0.018	<0.07	>0.35
$0.5 - 1.5$	< 2.1	>0.033	<0.10	>0.24
<0.5	< 1.9	>0.059	<0.60	>0.17

cuts. The fit gives a signal yield of $(3.17 \pm 0.02) \times 10^6$ Λs out of a total of 3.42×10^6 entries. The two selection requirements have a Λ signal efficiency in the data of $(70.1 \pm 0.1)\%$ and an efficiency for the background of 0.6%. For the inclusive MC sample, the efficiency is 79%. The $c\tau_\Lambda$ distribution for the surviving Λ candidates, showm in Fig. 3.5, shows no evident prompt background. Black dots are data points and blue line is fitted fuction. Used function is convoluted function of decay function and gaussian function. Fitted value of $c\tau_\Lambda = 7.00\ cm$ is a little differ with $c\tau_{PDG} = 7.89\ cm$. the fitted FWHM resolution of the Λ mass peak with all Λ selection requirement is $\Gamma^{resol}_{\Lambda\to p\pi} = 1.50 \pm 0.01$ MeV

3.3 $\Xi^-\pi$ selection

3.3.1 Ξ^- selection

Ξ^- particle is baryon state composed of (d,s,s) valance quarks. Because this is lightest baryon with Strangeness = (-2) and heavier than $m_\Sigma + m_\pi$, it almost decay with weak force coupling to Λ and π with long life time as like

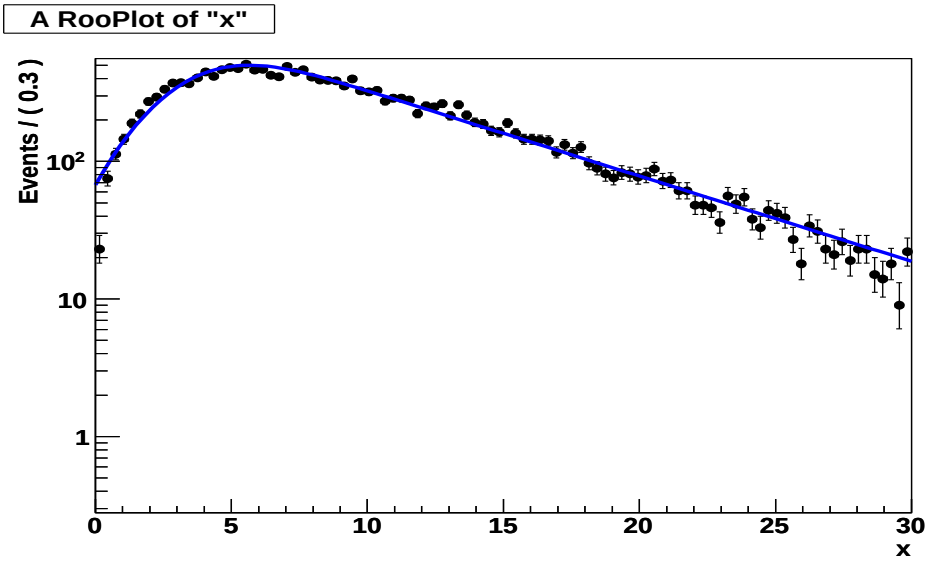

Figure 3.5: The $c\tau$ distribution for the selected Λ^0 candidates.

Λ decay to proton and π. Also Ξ^- particle has (-1) charge, so 99.9% of decay ratio is $\Lambda\pi^-$.

Because we already studied good selection criteria for Λ, we can get pure Ξ^- samples by adding one (-1) charged track to Λ samples. What we can know for charged track in belle detector is just momentum and position information with some signal difference in detector for PID. Though we can estimate particle ID using Likelihood ratio but it's not perfect truth, so we need to assign mass and particle type by arbitrarily. With Λ particle selected by our requirement, we reconstruct Ξ^- particle by adding one (-1) charge tracks after assigning π mass and determine the distribution of $M_{\Lambda\pi} = M(p\pi_1^-\pi_2^-) - M(p\pi_1^-) + m_\Lambda$ with $m_\Lambda = 1115.68$MeV (PDG), which is shown in Fig. 3.6. Top points which fitted by blue histogram is distribution with only Λ requirements applied.

When we see the distribution of $M(\Lambda\pi^-)$ from threshold mass range, we can see totally three peak in Fig. 3.7 black histogram. This is MC simulation

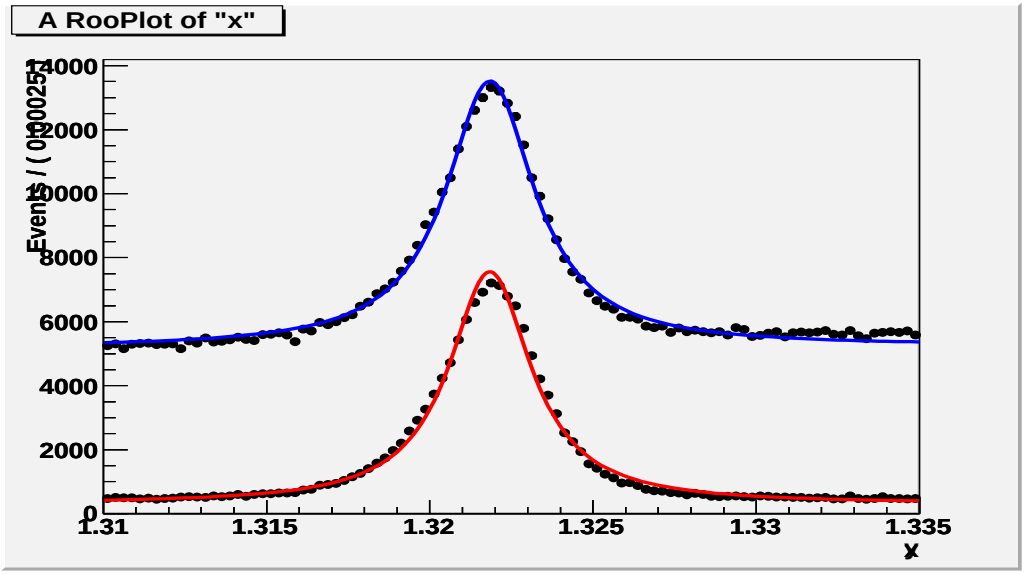

Figure 3.6: the M($\Lambda\pi^-$) distribution for selected Λ candidates. The top array of data points show the distribution with only Λ requirements applied. The lower set of points is the distribution for events that survive all cuts listed in Table. 3.3

data with rough cut for checking mass background distribution. The middle peak is Ξ^- resonance peak as we know and right-side wide width resonance peak is $\Sigma^-(1385)$ resonance which has $\Gamma_{PDG} = 36 \pm 5$MeV. Left side peak in threshold is duplicated π peak which we simply named. In $\Xi^*(1530)$ study, we don't need to give cut for this peak like Background bump because it is in outside of 2 Γ range of Ξ^-. But it will be important in H-dibaryon search. Below is detailed explanation.

When we select π^- tracks to add Λ samples for making Ξ^-, we reject π^- track candidates if π^- track is used both as the Λ's daugther and as the Ξ^-'s daughter. But there's still same tracks which be used twice because of wrong tracking. One possible idea is charged track traped inside CDC and

draw many tracks with different z value. the other is charged particle left footprint with big position deviation which is enough tracking as two track. In both case, these two tracks have similar track arc, it have almost similar momentum. As a result, if we add these two track then we can get bump like background in threshold mass region of two times of assigned mass because there's no momentum difference between two tracks. Because we can get true particle MC information from MC truth Panther table, we can confirm this by MC. For rejecting duplicated tracks, we can use mass distribution of two tracks as $M(\pi_1^-\ \pi_2^-)$ and number of signal hits from two tracks in CDC which will be explained later. The red line in Fig. 3.7 left panel histogram is after giving $M(\pi_1^-\ \pi_2^-)$ cut. The $M(\pi_1^-\ \pi_2^-)$ distribution is in right panel histogram and below 0.288GeV is used cut value in left figure. In our selection criteria, we doesn't use this cut because there's almost no effect of this duplicate track in signal region.

Here we need to explain about assigning Λ mass as PDG value in $M_{\Lambda\pi}$ distribution. If you see Fig. 3.4, you can see that Λ particle mass distribution has non zero resolution because of detection error though Λ doesn't have width itself. For ignoring this uncertainty, we can assume all Λ have same mass as PDG value. It means we can ignore uncertainty of proton and π tracks and vertex fitting error. By this way we can clearly distinguish Ξ^- with background otherwise resolution of Ξ^- would be worse than Fig. 3.6. So in this figure, a $\Xi^- \to \Lambda\pi_2^-$ signal is clearly evident. Here a fit using a BreitWigner fuction to represent the Ξ^- resonance peak and a polynomial function to represent the background. Signal yield of Ξ^- of upper Blue curve with data points is 13,578 $\pm$ 858 in a total 33,327 entries (within $\pm$ 2Γ of the peak), with a FWHM resolution of $\Gamma^{resol}_{\Xi\to\Lambda\pi} = 2.27 \pm 0.03$ MeV. The fit returns $M_{\Xi^-} = 1321.84 \pm 0.01$ MeV (statistical error only); the PDG value is 1321.71 ± 0.07 MeV. Lower red curve with data points is results after giving all cut values optimized after. All cut values are decided by using FoM with $\Xi^*(1530)$ resonance for optimizing $\Xi^\pm + \pi^\pm$ samples.

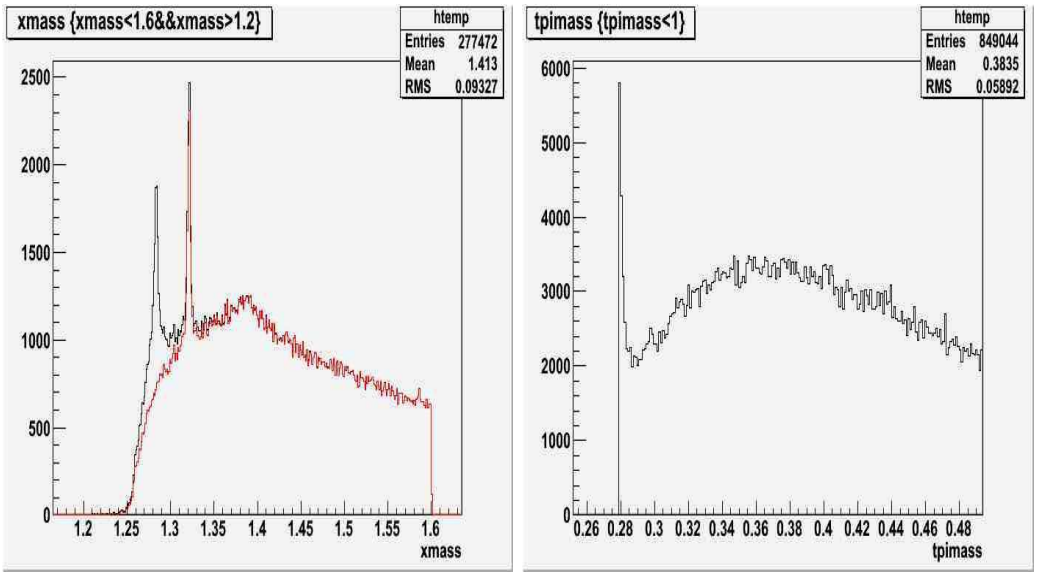

Figure 3.7: **left)** the M($\Lambda\pi^-$) distribution for selected Λ candidates with rough cut values for Ξ^- optimization from threshold mass to 1.6 GeV. **right)** $M(\pi_1^-\ \pi_2^-)$ distribution with background bump in thresold by duplicated tracks.

The other property of Ξ^- what we can check is $c\tau_{\Xi^-}$ distribution. Differ with $c\tau_\Lambda$ distribution, we can expect many Background. If you see Fig. 3.8, you can see Log scale $c\tau$ distribution of dotted MC data fitted with one gaussian (blue) and one convoluted function of gaussian and decay function (red). Measured life-time is $c\tau_{\Xi^-} = 3.72\ cm$ and PDG value is $c\tau_{PDG} = 4.91\ cm$.

A small asymmetry in the $\Xi^-\rightarrow\Lambda\pi^-$ line shape is observed in the lower M($\Lambda\pi^-$) distribution in Fig. 3.6. To investigate this we plot the $M(\Lambda\pi^-)$ distributions for low momentum ($p_{\Xi^-} < 1.2GeV$) and high momentum ($p_{\Xi^-} > 1.2\ GeV$) Ξ^- candidates separately in Fig. 3.9, respectively.

Here it can be seen that the asymmetry is confined to the low momentum

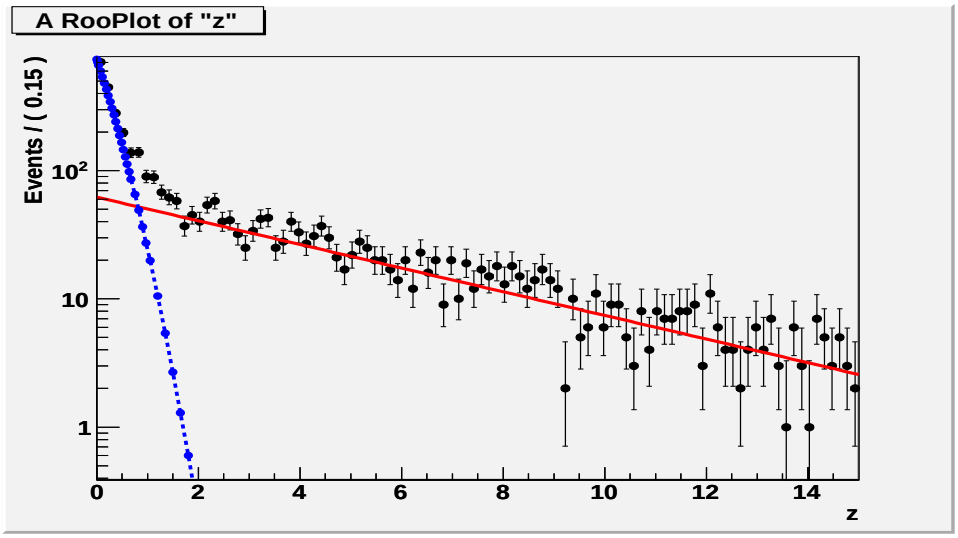

Figure 3.8: The $c\tau$ distribution for the Ξ^- candidates that survive all final selection requirements except for $c\tau \geq 0.5\ cm$. The solid ilne is the figure shows the result of a fit described in the text.

candidates. A momentum-dependent measurement bias for low momentum charged pions has been observed in the process $\psi' \rightarrow \pi^+\pi^- J/\psi$ [48]. We suspect that this bias is responsible for the line-shape asymmetry for low-momentum $\Xi^- \rightarrow \Lambda\pi^-$ candidates.

3.3.2 $\Xi^-\pi$ selection

By adding Ξ^- sample to (+) charged tracks assumed π, we can reconstruct $\Xi^*(1530)$. A loose selection $|M_{\Lambda\pi} - m_{\Xi^-}| < 2\Gamma^{resol}_{\Xi\rightarrow\Lambda\pi}$ is made to define initial Ξ^- candidates and these are combined with a positive track that is assigned a pion mass to produce the $M_{\pi\Xi} = M(p\pi_1^-\pi_2^-\pi_3^+) - M(p\pi_1^-\pi_2^-) + m_{\Xi^-}$ distribution shown as the upper histogram in Fig. 3.10. Here, since any Ξ_5^{--} penta-quark signal would likely be accompanied by a similar one for $\Xi_5^0 \rightarrow \Xi^-\pi_3^+$, the mass region between 1.7 GeV and 2.0 GeV is deliberately

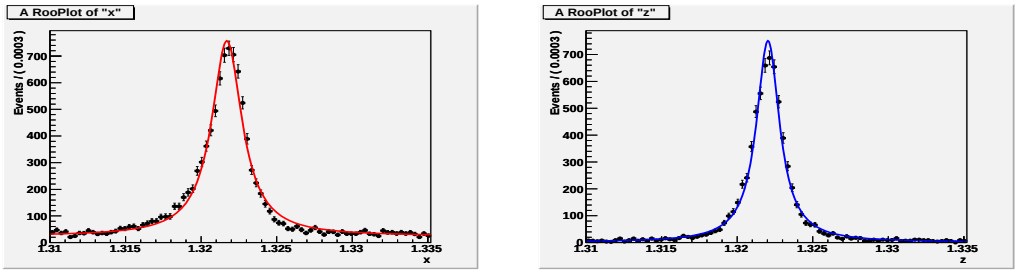

Figure 3.9: The M($\Lambda\pi^-$) distributions for $p_\Xi < 1.2\ GeV$(Left), and $p_\Xi > 1.2\ GeV$(Right) for events in the $\Xi^*(1530)$ peak. A small asymmetry in the shape of the low momentum $\Xi^- \to \Lambda\pi^-$ mass peak is attributed to bias in the slow-pion momentum measurements.

blinded. In this figure, there is a prominent $\Xi^{*0}(1530)$ resonance peak and a small, but significant narrow peak near 2.74 GeV that we attribute to resonance $\Xi_c^0(2470) \to \Xi^-\pi_3^+$.

As you can see black line histogram in Fig. 3.10 left panel, there's too many backgroud compare with signal. To reduce these backgroud, we used several cut parameters. We use the $\Xi^{*0}(1530)$ peak to form a figure of merit for further cuts as control sample. By this way, we can get branching fraction for $\overline{\Xi}^{*0}(1530)$, $\Xi_c^0(2470)$ and $c.c$ not for $\Xi^{*0}(1530)$. Lower bold line histogram is the result after using all requreiments decidec by FoM. Fig. 3.10 right panel shows the result of a fit to the $\Xi^{*0}(1530)$ mass region using a Gaussian-broadened BW function [49] with floating peak mass & resolution and BW width fixed at the PDG world average value ($\Gamma_{\Xi^{*0}} = 9.1 \pm 0.5$ MeV [29]), plus an ARGUS-type function [50] to represent the background. We use the fitted $\Xi^{*0}(1530)$ signal yield, $n_{\Xi^{*0}(1530)}$ and the integral of the background over a mass interval of $\pm\,\Gamma_{\Xi^{*0}}$ around the peak, n_{bkg}, to form a figure of merit $FoM = n_{\Xi^{*0}(1530)}/\sqrt{n_{\Xi^{*0}(1530)} + n_{bkg}}$ that is used to optimize selection requirements on the Ξ^- and Λ^0 candidate selection.

We tried many kinds of cut parameter for optimization. We optimize se-

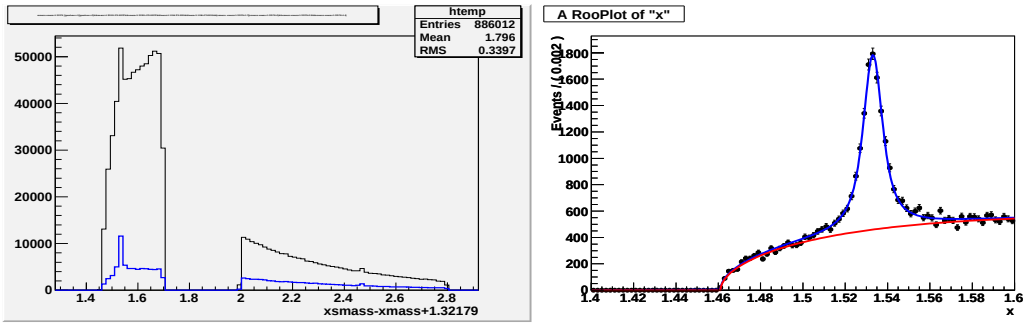

Figure 3.10: **Left:** The $M(\Xi^-\pi_3^+)$ distribution for selected Ξ^- candidates. The black (upper) histogram is the result for the loose Ξ^- selection. The blue (lower) histogram is the result after optimizing the Ξ^- and $\Xi^-\pi_3^+$ selection requirements using the FoM described in the text. **right:** A fit to the $\Xi^{*0}(1530)$ region of the $M(\Xi^-\pi_3^-)$ distribution.

lection requirements for the $\Xi^{*0}(1530)$ for the quantities : $\Delta M_{p\pi_1^-} = M_{p\pi_1^-} - m_\Lambda$, $\Delta M_{\Lambda\pi_2^-} = M_{\Lambda\pi_2^-} - m_{\Xi^-}$, $c\tau_{\Xi^-}$, $\chi^2_{\pi_2^-}$ from a $\Lambda\pi_2^-$ vertex fit; and $dz_{\pi_2^-}$, $dz_{\pi_3^-}$ & $dr_{\pi_3^-}$ which dz & dr are the minimum displacements between the track and the run-dependent interaction point along and transverse to the beam direction, respectively.

Most important cut parameters which give big decrease of Background are $\Delta M_{p\pi_1^-}$, $\Delta M_{\Lambda\pi_2^-}$ and $c\tau_{\Xi^-}$. With rough cut values which required for stable background fitting, we got FoM distribution as Fig. 3.11. With in mass interval of $\pm\ \Gamma_{\Xi^{*0}}$ around the peak, we use the fitted $\Xi^{*0}(1530)$ signal yield $n_{\Xi^{*0}(1530)}$ and the integral of the background n_{bkg} to form a $FoM = n_{\Xi^{*0}(1530)}/\sqrt{n_{\Xi^{*0}(1530)} + n_{bkg}}$.

Fig. 3.11 (left) shows how the FoM varies with n_Λ for the $|\Delta M_{p\pi_1^-}| < n_\Lambda \cdot \Gamma^{resol}_{\Lambda\to p\pi}$ requirement on the Λ mass ($\Gamma^{resol}_{\Lambda\to p\pi} = 1.50$ MeV). Fig. 3.11 (right) shows the corresponding plot for n_Ξ for the $|\Delta M_{\pi_2^-\Lambda^0}| < n_\Xi \cdot \Gamma^{resol}_{\Xi^-\to\Lambda\pi}$ requirement on the Ξ^- mass selection ($\Gamma^{resol}_{\Xi^-\to\Lambda\pi} = 2.27$ MeV). In both cases, there is a broad maximum near $n = 2$ and a slow fall-off at larger values; we select

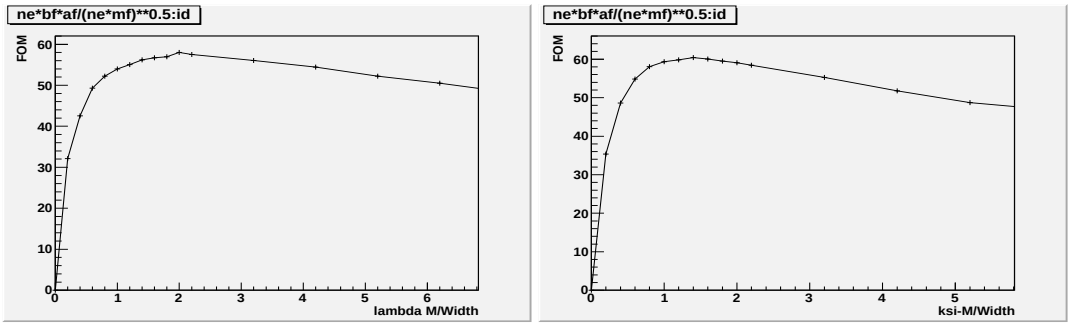

Figure 3.11: *FoM versus* n_Λ **(left)** and n_Ξ **(right)** for events within $\pm\Gamma_{\Xi^{*0}}$ of the $\Xi^{*0}(1530)$ peak.

events with $\Delta M_\Lambda < 2\Gamma^{resol}$.

Fig. 3.12 **(left)** shows how FoM varies *vs* $c\tau_\Xi^{min}$ cut value. As you can see in Fig. 3.8, there's BG with gaussian distribution with mean $\simeq 0$ and signal is convoluted distribution of decay function and gaussian with mean is more than 0. when the Ξ^- candidates are required to have $c\tau_\Xi \geq c\tau_\Xi^{min}$. Here a peak occurs in FoM for $c\tau_\Xi^{min}$ just above zero; in the following we use $c\tau_\Xi^{min} = 0.5$ cm. When we select $c\tau_\Xi$ cut parameter we studied $c\tau_\Xi$ and $dr_{\pi_2^-}$ both. Because we can expect correlation between dr and $c\tau$, we need to choose one of them. You can see scatter plot of MC in Fig. 3.12 **(right)** X-axis is dr and Y-axis is $c\tau$ distribution. Red cross is signal MC and black dot is Background. As you can see many signal near 0 of dr and $c\tau$ but because of cos factor in $c\tau$ parameter, we can cut out Background only events below 0 of $c\tau$ differ with dr. But because of short life-time of Ξ it's hard to cut out large value of cτ or dr. So eventually we select cut parameter as $c\tau$ with near 0 cut requirement.

Differ with $dr_{\pi_2^-}$, we can use $dr_{\pi_3^+}$ for cut parameter because $\Xi^{*0}(1530)$ doesn't have life-time with strong decay and penta-quark is also expected no lifetime. Also $\Xi_c^0(2470)$ resonance has small life time $c\tau = 33.6\ \mu m$ so there's no problem to see peak as Fig. 3.10. Because $\Upsilon(1,2S)$ decay to $\Xi^{*0}(1530)$ and other particles without life-time, $dr_{\pi_3^-}$ need to be near zero

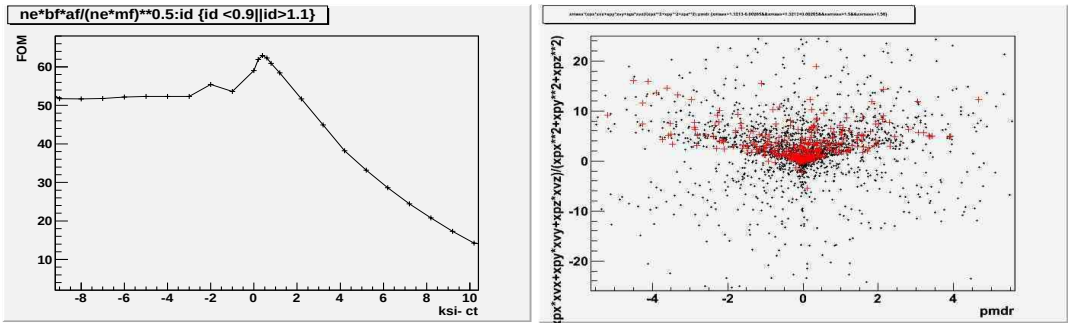

Figure 3.12: **(left)** *FoM versus* $c\tau_{\Xi}^{min}$ for events within $\pm\Gamma_{\Xi^{*0}}$ of the $\Xi^{*0}(1530)$ peak. **(right)** scatter plot $dr_{\pi_2^-}$ *versus* $c\tau$ distribution with red cross signal and black dot background.

as Fig. 3.13 (left) viewed with Log scale. As you can see BG also gathered near zero but we can reduce π tracks with large dr value would be generated out side of beam position like beam pipe background. Shaded histogram is signalMC and colorless histogram is inclusive MC. Right panel figure is FoM with cut change of $|dr| < dr_{cut}$. Dotted point is checked values and X-axis for $dr_{\Xi^{*0}(1530)}$ value and Y-axis is FoM. When we get FoM, we use real $\Upsilon(1S)$ data without subtracting continuum data.

Before go to next cut parameter, it is better to mention about $\cos\theta_{\Xi^{*0}(1530)}$ cut in here. Although this parameter is not used in final cut requirements, we studied for checking. The definition of $\cos\theta_{\Xi^{*0}(1530)}$ is below.

$$\cos\theta_{\Xi^{*0}(1530)} = \frac{p_{\Xi^{*0}(1530)} \cdot l_{\Xi^{*0}(1530)}}{|p_{\Xi^{*0}(1530)}||l_{\Xi^{*0}(1530)}|}. \tag{3.2}$$

It's hard to find exact physical meaning of this parameter. Because of no life-time of resonance, decay position would be randomly distributed near IP position. So signal will be no dependece for cos. But for background we can assume by asymmetry of beam energy that mis-combination of Ξ^- and π^+ will show enhance in near 1 and -1 cosine value differ with signal

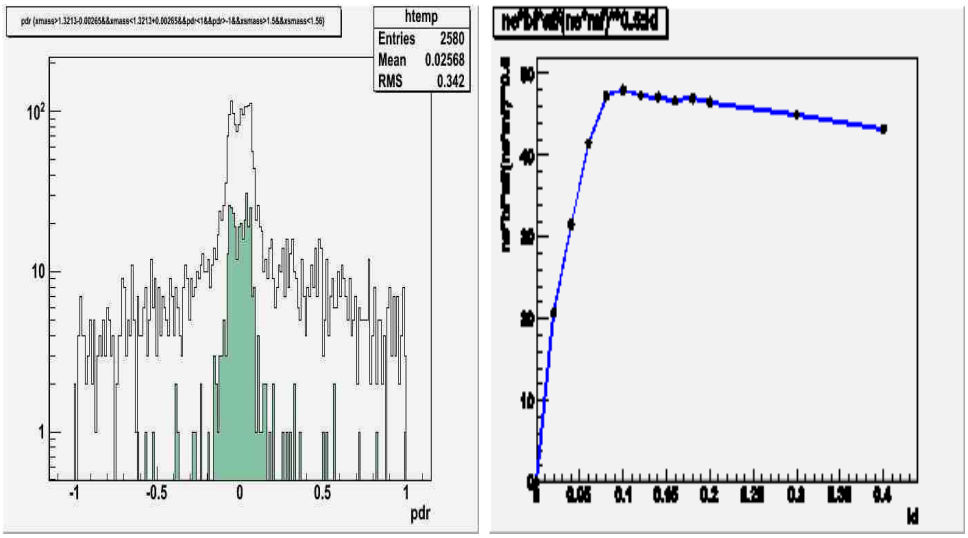

Figure 3.13: **(left)** $dr_{\pi_3^+}$ distribution with Signal MC(painted histogram) and inclusive MC background(colorless histogram). **(right)** *FoM versus* $|dr|^{max}_{\pi_3^+}$ for events within $\pm\Gamma_{\Xi^{*0}}$ of the $\Xi^{*0}(1530)$ peak.

which will not show any enhance in whole region as Fig. 3.14 **(left)**. For $\cos\theta_{CM}$ there's no difference expected between signal MC and inclusive MC. Fig. 3.14 **(middle)** CM frame distribution which satisfy expectation. In both histogram, shaded histogram is for signalMC and colorless histogram is for inclusive MC. We can cut out BG using $\cos\theta$ cut but it correlate with $dr_{\pi_3^+}$. After study, we conclude that $dr_{\Xi^{*0}(1530)}$ can cut out Background with better efficiency than $\cos\theta$. Fig. 3.14 **(right)** is scatter plot with X-axis for $dr_{\pi_3^+}$ and Y-axis for $\cos\theta_{\Xi^{*0}(1530)}$. mild color dot is signal MC which distributed in center line only and black dot is inclusive MC. By cut out dr mentioned in upper paragraph, we can cut out Background without signal using $dr_{\pi_3^+}$ in $\cos\theta$ near 1 and -1.

We can give similar cut for $dz_{\pi_3^+}$ & $dz_{\pi_2^-}$ like $dr_{\pi_3^+}$. Our detector has worse resolution for z direction compare with x-y plane as mentioned in detector section. So eventually we need to give wide cut value for efficiency.

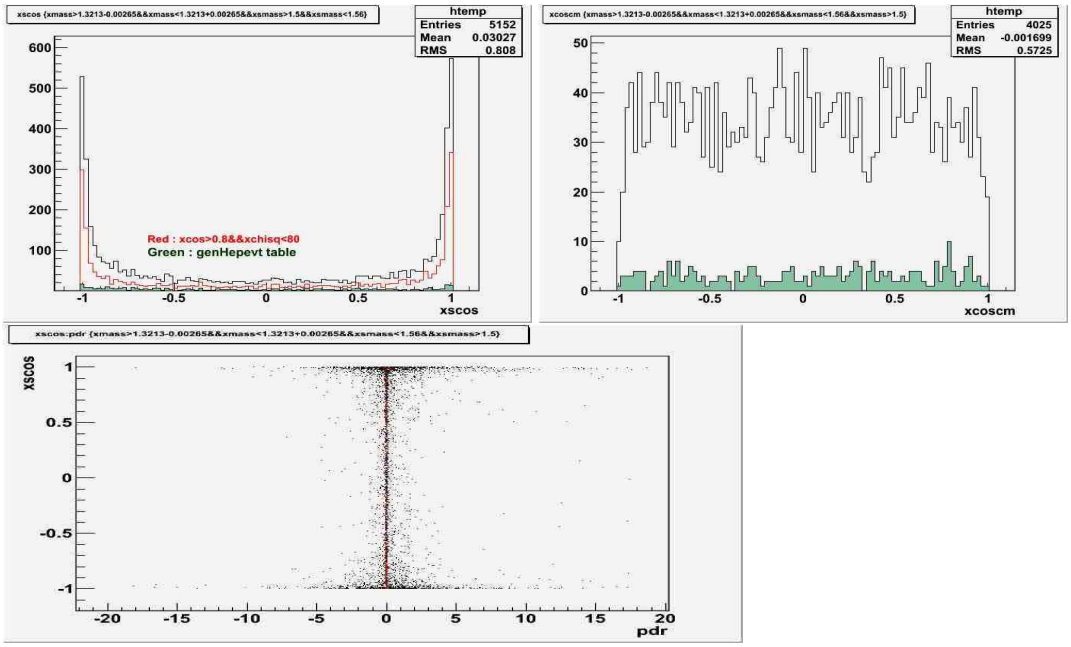

Figure 3.14: **(Upper left)** $\cos\theta_{\Xi^{*0}(1530)}$ distribution for signalMC (painted histogram) and inclusiveMC (colorless) histogram. **(Upper right)** $\cos_{CM}\theta_{\Xi^{*0}(1530)}$ distribution for signalMC (painted histogram) and inclusiveMC (colorless) histogram in CM frame. **(lower)** $dr_{\pi_3^+}$ *versus* $\cos\theta_{\Xi^{*0}(1530)}$ scatter plot with red point is signalMC and black point is inclusiveMC.

Fig. 3.15 **(left)** is FoM of $dz_{\pi_3^+}$ and **right** is FoM of $dz_{\pi_2^-}$. Dotted point is fitted position and we analysis more position where expected be large FoM values. The deviation is differ for dz between π from $\pi_3^+(\Xi^{*0}(1530))$ and $\pi_2^+(\Xi^-)$. Because of life-time Ξ^-, π_2^- need to have detected position a little far from IP-position. So dz of π_2^- can be large for signalMC. Also z position precisely detected near IP-position by cathode detector, so π_2^- which depart from IP can have worse resolution than π_3^-.

Next one is χ^2 values from vertex-fitting. Vertex fitting gives minimum-χ^2 value with decay position using equation of motion constraint by track

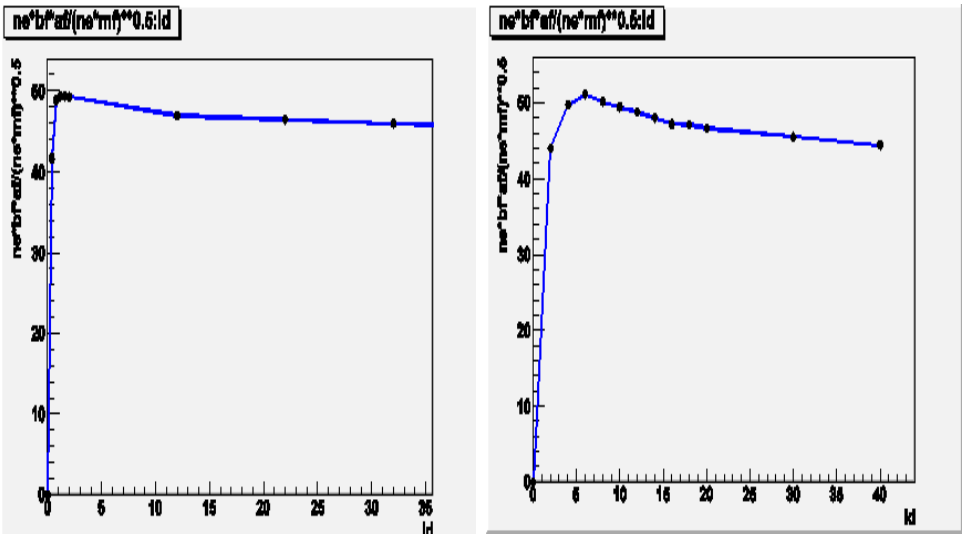

Figure 3.15: **(left)** *FoM versus* $|dz|^{max}_{\pi_3^-}$ and **(right)** *FoM versus* $|dz|^{max}_{\pi_2^-}$ distribution for events within $\pm\Gamma_{\Xi^{*0}}$ of the $\Xi^{*0}(1530)$ peak.

parameters. For Ξ^- reconstruction, χ^2 determined also by mass constraint of $m_{PDG}(\Xi^-)$. Fig. 3.16 is *FoM* figure for $\Xi^{*0}(1530)$ **(left)** and Ξ^- **(right)**. When we see χ^2 distribution directly, distribution decrease with increasing χ^2. So without worry for overestimated low χ^2 background, we cut out high χ^2 events.

When you see the near blind box region below 1.7GeV in Fig. 3.10 black line histogram, distribution of background can be bump like even though this effect looks be disappear after cut requirement which is mentioned below. When we study of this region by inclusive MC samples with rought cut value, we can also see this effect as in Fig. 3.17 (left). Upper histogram is with rought cut values, middle histogram is with $\mathcal{R}(\pi_3|K) \geq 0.1$, and lower bold histogram is with $\mathcal{R}(\pi_3|K) \geq 0.1$ & $\mathcal{R}(\pi_3|P) \geq 0.1$. We can suspect this parameter as same as dupicated track effect in Ξ^- distribution. Because assigning m_p and m_π for two duplicated same track, peak like bump arise in near 1.7GeV mass region. By selecting π_3^- track with likelihood is more than

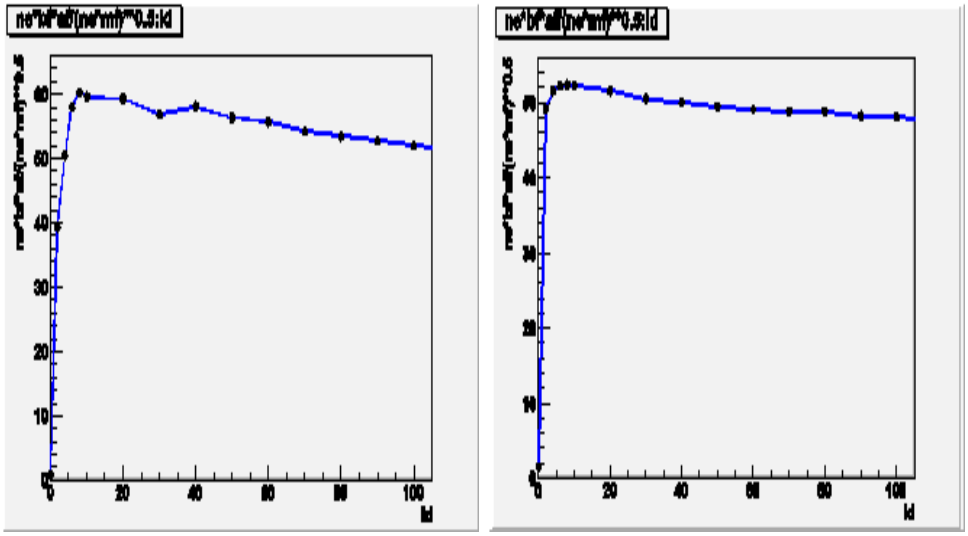

Figure 3.16: **(left)** *FoM versus* $\chi^2(\Xi^-\pi_3^+)$ and **(right)** *FoM versus* $\chi^2(\Lambda\pi_2^-)$ distribution for events within $\pm\Gamma_{\Xi^{*0}}$ of the $\Xi^{*0}(1530)$ peak.

0.1 compare with other possible particles, we can subtract this bump-like Background. After this PID criteria, you can see there's no more bump in near 1.7GeV as Bold line histogram in Fig. 3.10. For more exact investigation, we see mass distribution of $\mathrm{M}(\pi_3^- + p)$ after changing π_3^- mass to proton mass value. With $\mathcal{R}(\pi_3|K) \leq 0.1$ & $\mathcal{R}(\pi_3|P) \leq 0.1$ which will cut out, we can get peak distribution in mass threshold which is expected duplicated tracks.

Table 3.3 show all selection requirements what i mentioned above text. All cut values are decided by efficiency and FoM for getting high efficiency of $\Xi^{*0}(1530)$ which we expect also high efficiency for penta-quark search.

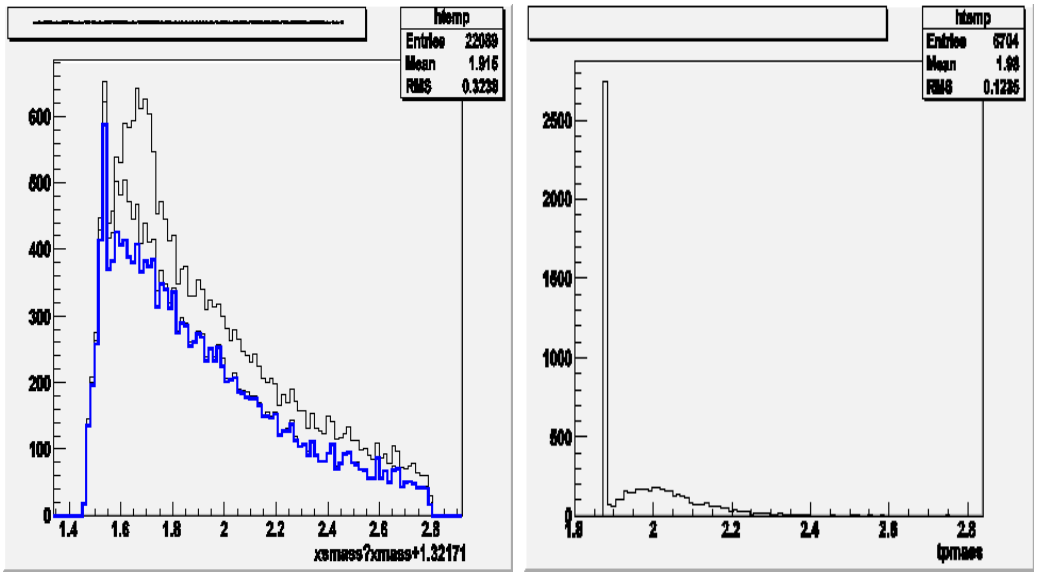

Figure 3.17: **(left)** shows $M(\Xi^-\pi^+)$ distribution of MC with rought cut. Middle histogram is with $\mathcal{R}(\pi_3|K) \geq 0.1$ and lower bold histogram is with $\mathcal{R}(\pi_3|K) \geq 0.1$ & $\mathcal{R}(\pi_3|P) \geq 0.1$. **(right)** shows $M(\pi_3(m_p)p)$ distribution and big peak in threshold is duplicated track of proton and π_3.

Table 3.3: A listing of the $\Xi^-\pi$ selection requirements.

Particle	Quantity	Requirement
Λ^0 ($\bar{\Lambda}^0$)		
	$\mathcal{R}(p\|\pi^+)$	≥ 0.1
	$\mathcal{R}(p\|K)$	≥ 0.1
	$c\tau_\Lambda$	no cut
	$\Delta M_{p\pi}$	$\leq \pm 2\Gamma^{resol}_{\Lambda\to p\pi}$
	goodvee	1 or 2
Ξ^- ($\bar{\Xi}^+$)		
	$c\tau_\Xi$	≥ 0.5 cm
	$\Delta M_{\Lambda\pi}$	$\leq \pm 2\Gamma^{resol}_{\Xi\to\Lambda\pi}$
	$\chi^2_{\pi_2^-}$	≤ 20
	$\|dz_{\pi_2^-}\|$	≤ 10 cm
$\Xi^-\pi$ ($\bar{\Xi}^+\pi$)		
	$\chi^2_{\pi_3}$	≤ 20
	$\mathcal{R}(\pi_3\|p)$	≥ 0.1
	$\mathcal{R}(\pi_3\|K)$	≥ 0.1
	$dr_{\pi_3^+}$	≤ 0.2 cm
	$\|dz_{\pi_3^+}\|$	≤ 5 cm

3.3.3 data comparision

We decide selection criteria by studying FoM using MC sample of $\Upsilon(1S) \to \Xi^{*0}(1530)X$ inclusive channel. We need to see anti-particle channel for checking which is $\Upsilon(1S) \to \overline{\Xi^{*0}}(1530)X$ inclusive channel. We can expect same PDF distribution and a little different total events number because of different cross section and property of particle and anti-particle. Fig. 3.18, Fig. 3.19 and Fig. 3.20 show mass distribution of each particle (black line histogram) and anti-particle (red line histogram) for inclusive MC in left figure and for real $\Upsilon(1S)$ samples in right figure. Fig. 3.18 two histograms are mass distribution of Λ. Fig. 3.19 two hisograms are mass distribution of Ξ^- and Fig. 3.20 two histograms are mass distribution of $\Xi^{*0}(1530)$.

There's two main difference between histograms. One is difference of signal to background ratio between MC and real data. The reason is estimated branching ratio of each baryon is not exactly same with real. But after you can see, we compare properties like number of track, total energy, etc between MC and real data later and we conclude okay to use. Also because distribution of background and signal, i.e, PDF shape is same for each parameter, we can think MC for comparision and background reducing cut estimation would be fine. For $\Upsilon(1,2S)$ meson decay, only few inclusive decay channel is studied and no baryon inclusive channel branching fraction measured. So we need to fix yield of baryon in MC. Another is difference between particle and anti-particle. This difference can come from many effect but mainly we can understand about small amount of anti-particle by big cross-section of anti-particles with materials compare with particles. This make change particle trajectory and reduce efficiency although we generate same number of particle and anti-particle in MC. The numbers in histogram is to show difference between particle and anti-particle. Do not compare these number between MC and real data because generated $\Upsilon(1S)$ is differ and we didn't subtract continuum data in here.

When we think about penta-quark, we need to care $\Xi_5^0 \to \Xi^-\pi^+$ and

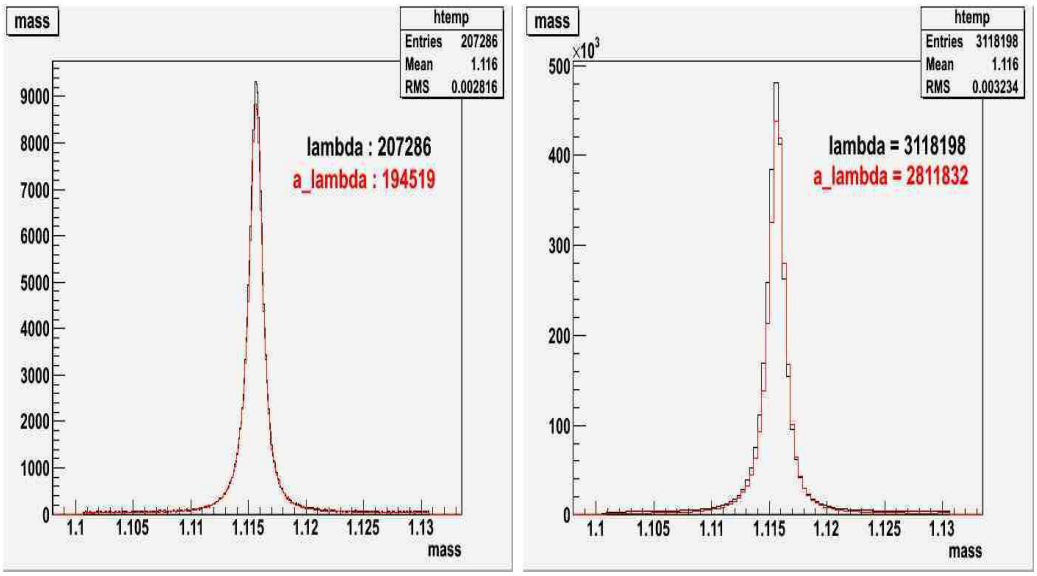

Figure 3.18: $M(p\pi_1^-)$(black line), $M(\bar{p}\pi_1^+)$(red line) distribution from MC data sample **(left)** and real data sample **(right)**.

$\Xi_5^{--} \to \Xi^-\pi^-$ channel both. If we see signal only in $\Xi^-\pi^+$ channel, it's hard to say what we see is penta-quark rather baryon resonance. But if wee see signal both channel, it's good sign of penta-quark anti-decuplet expectation.

Fig. 3.21 show mass distribution of $M(\Xi^-\pi_3^+)$ as black line histogram and mass distribution of $M(\Xi^-\pi_3^-)$ as shaded histogram. Left figure is of inclusive MC and right figure is of $\Upsilon(1S)$ real data. In both MC and real data have similar distribution without signal shape with a little difference of ratio of particle and anti-particle channel as mentioned above. In real data distribution, we can see $\Xi_c^0(2470)$ clearly differ with MC (we didn't give decay ratio of $\Upsilon(1S) \to \Xi_c^0(2470)X$). Middle part of histogram is empty because of blind analysis box and we can expect stable linear distribution of background in blind region like MC for real data.

To validate the MC and efficiency calculations, we compare data and

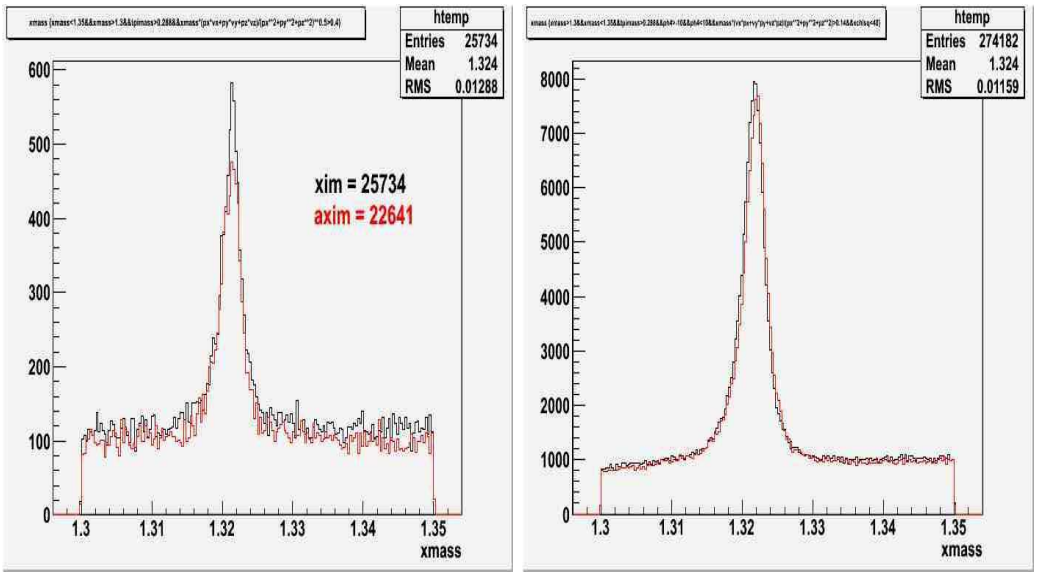

Figure 3.19: $M(\Lambda\pi_2^-)$(black line), $M(\bar{\Lambda}\pi_2^+)$(red line) distribution from MC data sample **(left)** and real data sample **(right)**.

MC distributions of the number of charged track n_{trk}, neutral clusters n_{cls}, Fox-Wolfram moment R_2, visible track energy (assuming π masses) E_{trk}, the visible neutral energy E_{vis}, and the total visible energy E_{sum} in Fig. 3.22, where the red color histograms are for data and the black histograms are for MC. From this comparision, we can say simulation of detector performance is quite agree with real. So we can trust our cut estimation using MC and signal efficiency. Reasonable agreement is shown in figures.

After all these check, we also see braching fraction value of each run for checking. There's three kinds of run that is on-resonance run, off-resonance run and energy scan run. When we use data sample for analysis of $\Upsilon(1S, 2S)$, we need to use appropriated run number which is on-resonance run. It already decided what run number is on-resonance, but we need to check and see the tendency. Fig. 3.23 show branching fraction values for each run **(left)** and

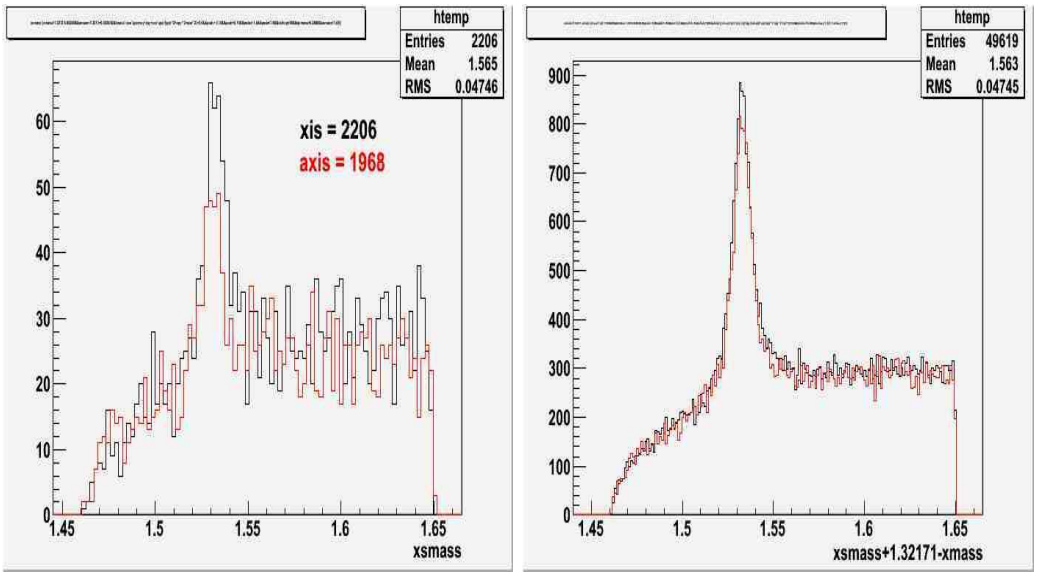

Figure 3.20: $M(\Xi^-\pi_3^+)$(black line), $M(\Xi^+\pi_3^-)$(red line) distribution from MC data sample **(left)** and real data sample **(right)**

for divided run **(right)**. Right figure show off-resonance in 1,3 bin, energy scan in 2 bin and the other is on-resonance. In both case we use generated number as $\Upsilon(1S)$ number in BELLE, so difference between bin in only important and absolute value doesn't have any mean. You can also compare left and right figure. So what we use in analysis is these on-resonance data samples only.

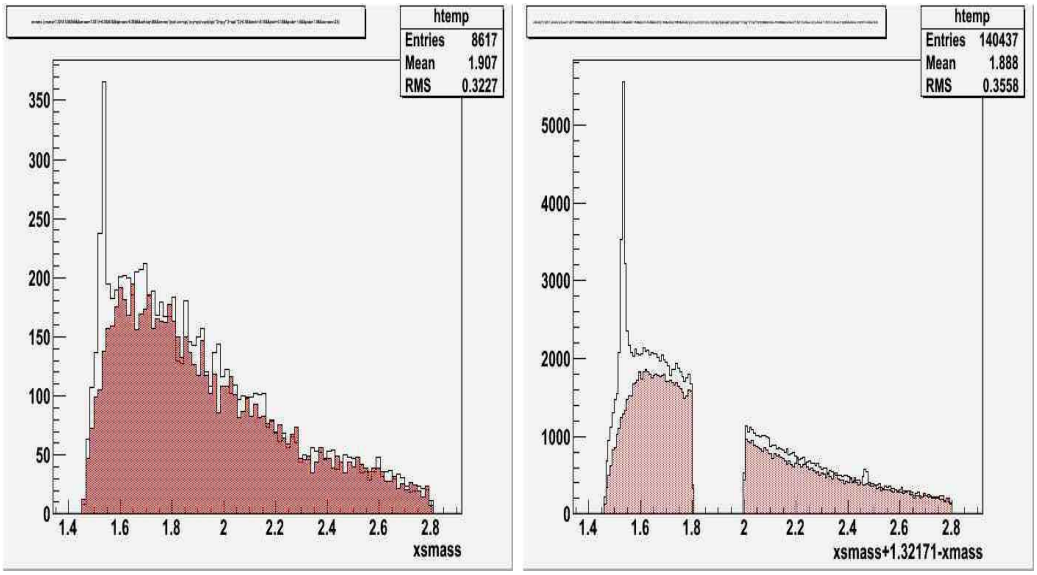

Figure 3.21: $M(\Xi^-\pi_3^+)$ (black line), $M(\Xi^-\pi_3^-)$ (red painted) distribution from MC data sample **(left)** and real data sample **(right)**

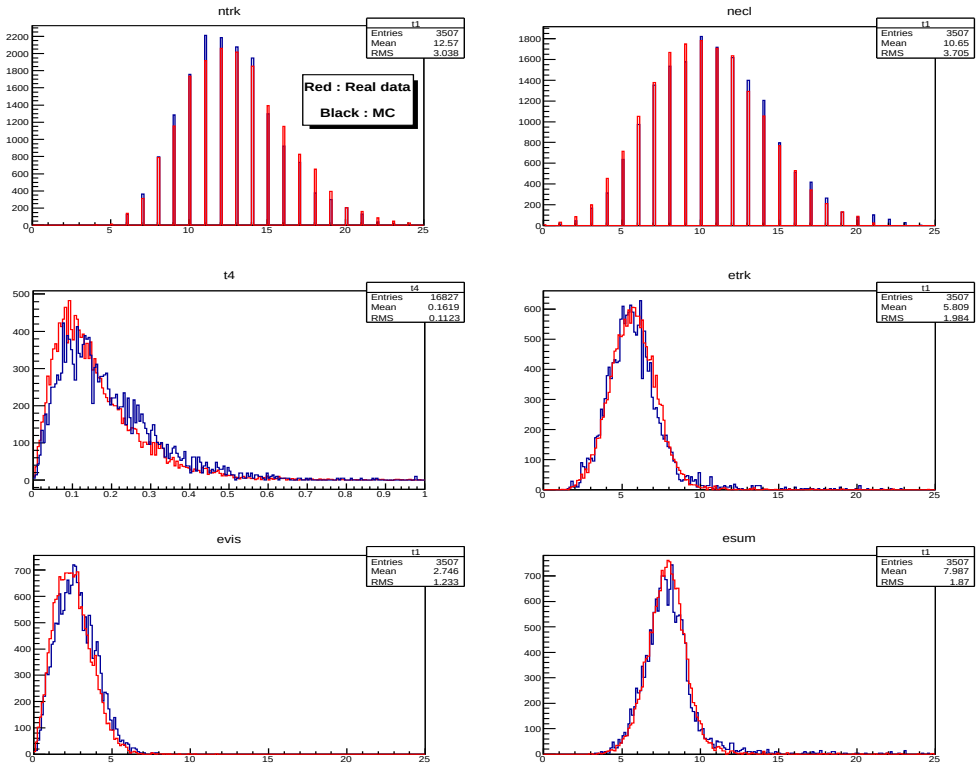

Figure 3.22: Data (red) and MC (blue) distributions for: **upper:** number of charged tracks (left), number of neutral clusters (right) **middle:** Fox-Wolfram moment R_2 (left), charged track energy sum (right), **lower:** visible neutral energy (left), total energy sum (right).

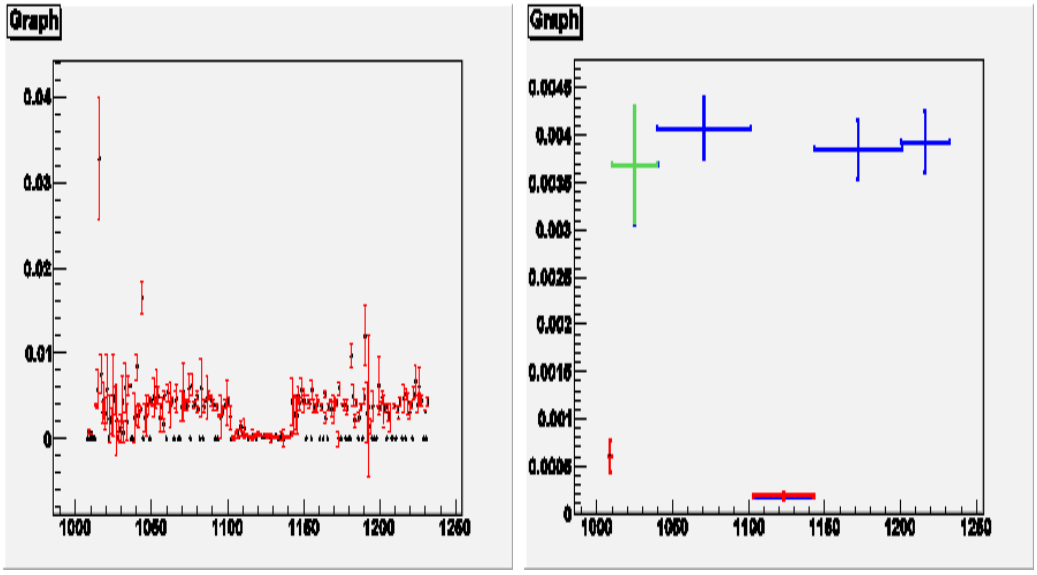

Figure 3.23: Values of $\mathcal{B}(\Upsilon(1S) \rightarrow \bar{\Xi}^{*0}(1530)\ X)$ determined run-by-run **(Left)** and for six subdivisions of the data sample **(Right)**. In the right panel, the red points (1^{st} and 4^{th} bins) are for off-resonance runs, the green point (2^{nd} bin) is from the energy scan and the blue points are from on-resonance running.

3.3.4 continuum-subtraction

As mentioned in Hadron B(J) section, we couldn't cut out continuum background by skim selection. If we want to subtract continuum background by cut parameter, we need to use event shape parameter. Because continuum background distribute two jet-like cone shape quark pair, we can distinguish $B\bar{B}$ pair decay from $\Upsilon(4S)$ because this show two spherical distribution. Our $\Upsilon(1S, 2S)$ decay to hadrons will show different distribution compair with two jet-like shape by more multiplicity than continuum data becasuse of OZI-rule's three gluons. But when we get R_2 distribution which is well-known distinguish factor, this cut will loose too much efficiency. Franckly speaking, we don't need to give to much attention for continuum background because $\Upsilon(1, 2S)$ cross-section is much higher than continuum cross-section.

So our strategy is subtraction of small continuum contribution by continuum data samples. To determine the level of background from $e^+e^- \to q\bar{q}$ ($q = u,\ d,\ s,\ \&\ c-$quarks) reapplied the same selection to Belle's near-$\Upsilon(4S)$ off-resonance data samples. The $M(\Xi^-\pi^+)$ distribution for these events, shown in Fig. 3.24 **(left)**, has prominent $\Xi^{*0}(1530)$ and $\Xi_c^0(2470)$ signals. To account for different luminosity and continuum cross sections, we scale the resulting $M(\Xi^-\pi)$ distributions by a factor F_{scale}, which for the $\Upsilon(1S)$ data is

$$F_{scale}^{1S} = \frac{\mathcal{L}(\Upsilon(1S))}{\mathcal{L}(\text{off}-\text{reson})} \times \frac{\sigma_{\text{cont}}(\Upsilon(1S))}{\sigma_{\text{cont}}(\text{off}-\text{res})} = \frac{5.75\ \text{fb}^{-1}}{56.08\ \text{fb}^{-1}} \times 1.22 = 0.125, \quad (3.3)$$

and the $\Upsilon(2S)$ is

$$F_{scale}^{2S} = \frac{\mathcal{L}(\Upsilon(2S))}{\mathcal{L}(\text{off}-\text{reson})} \times \frac{\sigma_{\text{cont}}(\Upsilon(2S))}{\sigma_{\text{cont}}(\text{off}-\text{res})} = \frac{24.9\ \text{fb}^{-1}}{56.08\ \text{fb}^{-1}} \times 1.10 = 0.49. \quad (3.4)$$

Because of Luminosity dependence for Belle Library, caseB library give different factor. $F_{scale}^{1S} = 0.110$ and $F_{scale}^{2S} = 0.43$. Subtract continuum distribution from our measured $M(\Xi^-\pi)$ distributions is shown in Fig. 3.24 **(right)**. The $\Xi_c^0(2470)$ signal persists in the $\Upsilon(1S)$ and $\Upsilon(2S)$ data samples

after the continuum subtraction. As we learned R value ($R = \frac{\sigma(e^+e^-\to q\bar{q})}{\sigma(e^+e^-\to\mu^+\mu^-)}$) ($q = u,\ d,\ s,\ \&\ c-$quarks)) is proportional to z_q^2 which will give high fraction for charm baryon as $\frac{4}{9}$. Oppositely $\Upsilon(1,2S)$ decay by OZI-rule with three gluon has small fraction for charm baryon because of heavy mass of c-quark to compare with u,d,s-quark mass similarity. As a result, continuum sample show many $\Xi_c^0(2470)$ peak as in Fig. 3.24 **(left)**. So Fig. 3.24 **(right)** histogram which is continuum subtracted $\Upsilon(1S)$ data sample give small $\Xi_c^0(2470)$ peak compare with $\Upsilon(1S)$ data sample without subtraction in Fig. 3.21 **(right)**.

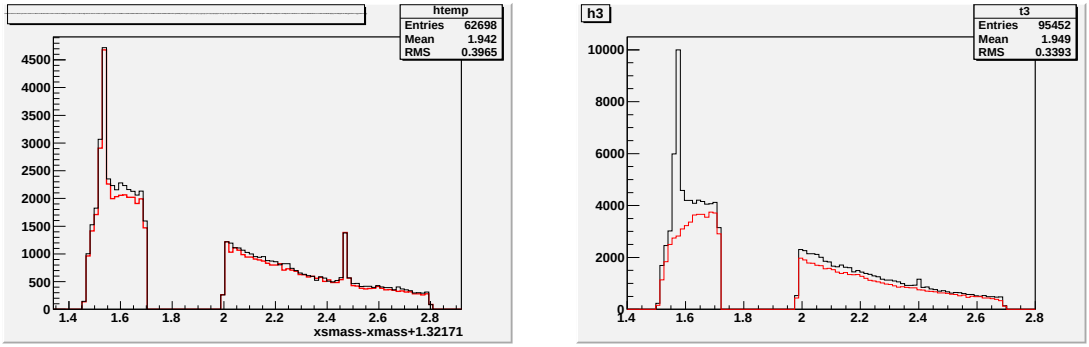

Figure 3.24: **Left)** The $M(\Xi^-\pi^+)$ (black) and $M(\bar{\Xi}^+\pi^-)$ (red) distributions for off-resonance continuum events. **Right)** Continuum-subtracted $M(\Xi^-\pi^+)$ (black histogram) and $M(\Xi^-\pi_3^-)$ (red histogram) distributions.

3.4 ΛΛ selection

3.4.1 mc simulation

To search the $H \to \Lambda\Lambda$ channel, we start with one Λ that is selected using the selection criteria listed in the Λ selection section. Differ with Ξ_5 pentaquark search, there's no peak like $\Xi^{*0}(1530)$ which can be used for deciding cut requirements as control sample. As you know there's no mother particle candidate which can decays to two baryon with strangeness. So we need to decide cut criteria using signalMC of H-dibaryon. When we decide cut requirements, signalMC samples with a $M_H = 2.24GeV$ and total width $\Gamma_H = 5MeV$ added to the inclusive MC background with an assumed signal branching fraction $\mathcal{B}(\Upsilon(1S) \to \Lambda\Lambda) = 4 \times 10^{-5}$. H-dibaryon mass in signalMC is decided by mass threshold of $2m_\Lambda = 2.232GeV$. When we try to give same cut for Λ_1 and Λ_2 both, it loose too many signal. So we use Λ selection to Λ_1 candidates only. For the second Λ_2 selection, we use the same particle ID and $\Delta M_{p\pi}$, and examine the combined Λ_1, Λ_2 vertex χ^2, and $c\tau_{\Lambda_2}$ using FoM and efficiency without GoodVee selection. When we select second Λ, we choose 2 tracks that one is (+) charge and the other is (-) charge which is not used in first Λ. It means one proton can be used first Λ and second Λ but it can't used twice in one sample.

The black histogram in Fig. 3.25 shows the $M(\Lambda\Lambda)$ distribution for inclusive MC events only where both Λs are selected using the Λ criteria given at the Λ selection section without signalMC. Here a sharp peak near threshold is evident. The source of this peak are events where the two proton tracks used in the $\Lambda\Lambda$ reconstruction are produced by the same particle as mentioned before in Ξ^- distribution named duplicated tracks. The blue histogram shows the $M(\Lambda\Lambda)$ distribution for events where the MC truth-table mother ID of the two daughter protons is required to be different; in this case, the near threshold peak is absent. If we see signal MC, duplicate tracks of π also show

this kind of bump. So we remove this potentially dangerous background in data by selection requirements of M(pp), $M(\pi^-\pi^-)$ and the number of CDC hits associated with a tracking, $Nhit_{trk}$.

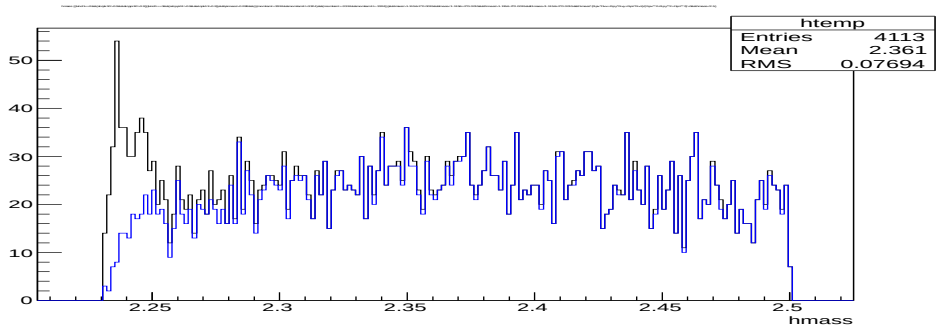

Figure 3.25: The $M(\Lambda^0\Lambda^0)$ distribution for inclusive MC events. The black histogram shows all entries; the blue histogram shows only those entries where the MC truth-table mother id of the two daughter protons are different.

Events in which one proton (π) produces two reconstructed tracks have $M(p_1p_2)$ ($M(\pi_1^-\pi_2^-)$) values that are very near $2m_p$ ($2m_\pi$). (Here we use the notation $\Lambda_1 \to p_1\pi_1^-$ $\Lambda_2 \to p_2\pi_2^-$.) The black histogram in Fig. 3.26 **(left)** shows the $M(p_1p_2)$ distribution for inclusive MC events; The sharp peak right at threshold is removed by the requirement $M(pp) > 1.878$ GeV. Fig. 3.26 **(right)** shows the corresponding $M(\pi^-\pi^-)$ distributions. We reduce these events by requiring $M(\pi^-\pi^-) > 0.28$ GeV. When we decide cut values, we checked signalMC also. As you can see in Fig. 3.26, cut value is almost near mass threshold but signalMC shows equally distributed to independent ot mass that means signal loss by these cut is almost negligible. Frankly speaking, for subtracting all background which make bump, we need to give $M(pp) > 1.9\ GeV$ which cut out too many signals. For subtract this background perfectly and save high efficiency, we used one more cut which performance is very powerful.

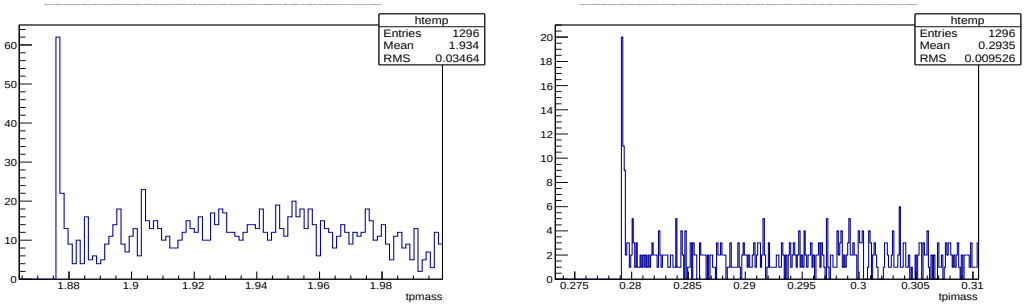

Figure 3.26: **Left** The black histogram shows the $M(pp)$ distribution for inclusive MC events. The red histogram shows the distribution for events where the two reconstructed protons are required to have different mother ids in the MC truth table. **Right:** The corresponding $M(\pi^-\pi^-)$ distributions.

In the cases when two reconstructed tracks are produced by a single proton, each track has a smaller-than-average number of associated CDC hits. This is evident in Fig. 3.27 **(left)**, where the black histogram shows the distribution of total number of CDC hits sum, N_{hit}, for the two proton tracks in inclusive MC events. The red histogram is the same distribution for $H \rightarrow \Lambda^0\Lambda^0$ signal MC events. The blue histogram shows the N_{hit} distribution for events where both reconstructed protons have the same mother id. This latter distribution is concentrated below $N_{hit} = 60$, while the inclusive and signal MC distributions are concentrated above $N_{hit} = 60$. The red histogram in Fig. 3.27 **(right)** shows the $M(\Lambda\Lambda)$ distribution for inclusive MC events with $N_{hit} > 60$, where the near-threshold peak is absent.

After using these all cut, we study the FoM distribution of signalMC added to inclusive MC for choosing best cut values. The histogram in Fig. 3.28 **(left)** shows the χ^2 distribution from the $\Lambda_1 - \Lambda_2$ vertex fit for signal MC with red color and inclusive MC with blue color. The data points in Fig. 3.28 **(right)** shows the FoM associated with the maximum selected χ^2 value. If you see more detail, you can see there's many line in Fom dis-

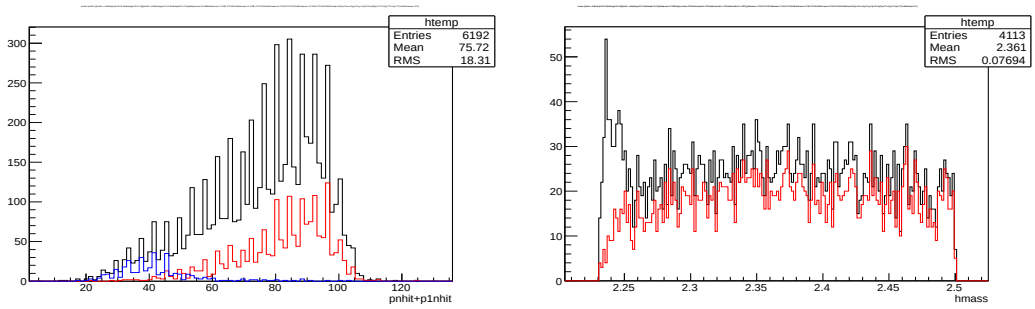

Figure 3.27: **Left** The black (red) histogram shows the N_{hit} distribution for inclusive (signal) MC events. The blue histogram shows the N_{hit} distribution for events where the two reconstructed protons have the same mother id. **Right:** The black (red) histogram shows the $M(\Lambda\Lambda)$ distribution for all inclusive MC events with $N_{hit} > 0$ ($N_{hit} > 60$).

tribution which show results with difference cut for second Λ. In here we can conclude that Particle ID selection only used is better than GoodVee cut for second Λ selection. Because the FoM value is very insensitive to the χ^2 value cut, as long as it is greater than 100 ($\chi^2_{Max} < 100$) we require $\chi^2_{Max} \leq 200$. If you compare this χ^2 cut value with $H \to \Xi^- p$ or $H \to \Lambda\, p\pi$ channel, you can see this value is quite big. The reason is we give IP-position constraint which is named Beam-Constraint-Fit in here. It is known that the application of the constraint vertex is close to IP to the vertex reconstruction improves the vertex resolution. Because $H \to \Lambda\Lambda$ decay channel is strongly decay, it means that it have negligible life-time so we can expect signal near IP position differ with Λ $p\pi$ channel. We can expect this constraint reduce some background particles generated in beam pipe will be mentioned later.

After checking FoM *versus.* χ^2 and efficiency, we decide to give particle ID cut $\mathcal{R}(p|\pi^+) \geq 0.1$ & $\mathcal{R}(p|K) \geq 0.1$ which cut out look like π or kaon with 90% likelihood ratio. But it's not enough to cut background by wrong Λ candidate. Because it's hard to cut out background which is composoff

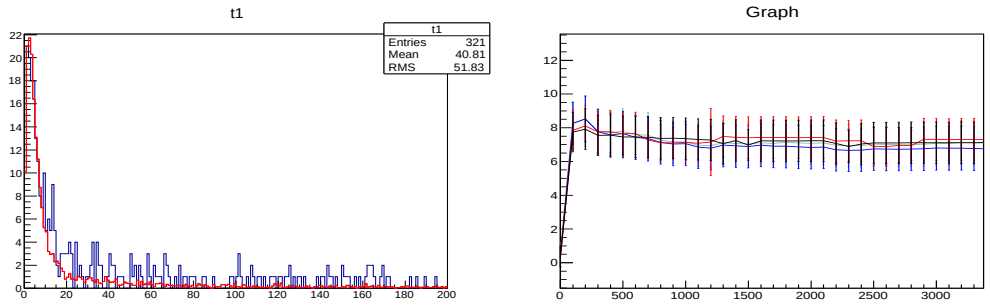

Figure 3.28: **Left** The χ^2 distribution for the Λ_1-Λ_2 vertex fit for the signal (inclusive) MC samples is shown as a red (blue) histogram. **Right:** The FoM as a function of the maximun χ^2 requirement.

real two Λ. We need to reduce all possible mis-reconstructed Λ background. For reducing this background, we checked $c\tau_{\Lambda_2}$ distribution and FoM *versus.* $c\tau^{min}_{\Lambda_2}$ cut value. The red color histogram in Fig. 3.29 **(left)** shows the $c\tau$ distribution for Λ_2 vertex fit for the signal MC sample and blue color histogram show the $c\tau$ distribution for the inclusive MC. The data points in Fig. 3.29 **(right)** shows the FoM associated with selected $c\tau^{min}_{\Lambda_2}$ value. The FoM value is very insensitive to the $c\tau^{min}_{\Lambda_2}$ value as long as it is less than zero and then be higher above zero and then decrease. So we require $c\tau \geq -0.5cm$. We can expect that mis-reconstructed Λ background will be gaussian like PDF with zero mean, so we can reduce almost one half of this background.

After these all selection requirements choosed, we checked how many samples are reconstructed in one events. Because sometimes background mis-reconstructed by one or two wrong tracks make signal like shape. For example mis-reconstructed one π with right 3-tracks can show signal like background. So we checked that the fraction of events that have two or more track combinations that share a subset of tracks is 2.8%. Although this is not a big fraction, for safety, we select only one event in one collision which

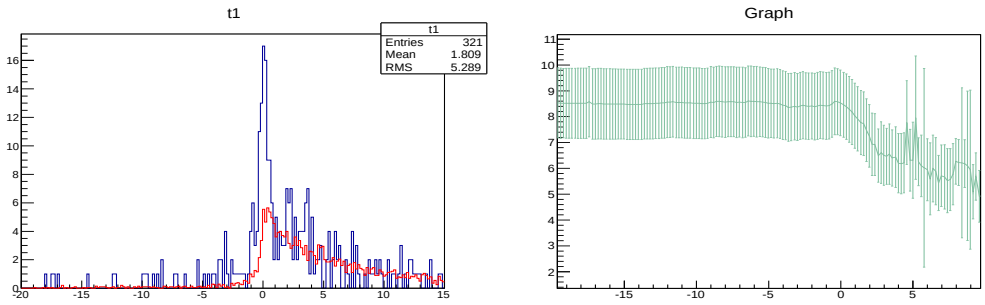

Figure 3.29: **Left:** The $c\tau_{\Lambda_2}$ distribution for the signal (inclusive) MC samples is shown as a red (blue) histogram. **Right:** The FoM as a function of the minimum $c\tau_{\Lambda_2}$ requirement.

have smallest χ^2 value of two-Λ reconstruction and this selection picks the correct event 95% of the time.

3.4.2 data comparision

Until this point, only MC has been used to establish selection requirements. Although all mass region is possible H-dibaryon region, our strategy is checking other experiment results which show positive results near 2 M_Λ threshold. So we further examined selection requirements effect on data with the near-threshold $M(\Lambda\Lambda) < (M_{\Xi^-} + M_p) = 2.26\ GeV$ blinded. This opened mass region is already studied by $\Xi^- p$ channel, we can use for checking. The data are continuum background subtracted using the technique described in continuum-subtraction subsection in $\Xi^-\pi$ selection section. For comparision, we use inclusive plus signal MC event samples, combined assuming a branching fraction of 4×10^{-5}. When we first see $\Upsilon(1S)$ data with only small cut criteria, there's big discrepency of total sample number that selected real data number is almost twice of inclusive MC. By investigating this effect from checking second proton's momentum, we can assume this effect come from

proton generated in detector. In Fig. 3.30 **(left)**, red color histogram is inclusive MC without blind box mass region and black histogram is real $\Upsilon(1S)$ data without blind box mass region. Because these proton has low momentum about 0.5 GeV and random direction, we can reduce this background by χ^2 of vertex fitting and $c\tau$ cut. Because our cut parameter enoughly reduce this background, momentum distribution be quite similar after giving $c\tau$ and χ^2 cut as in Fig. 3.30 **(right)**.

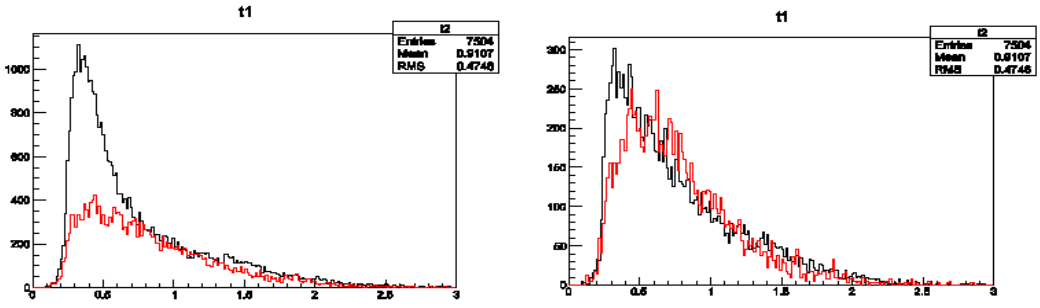

Figure 3.30: Momentum distribution from real $\Upsilon(1S)$ data sample(Black line) and inclusive MC(Red line) without χ^2 and $c\tau$ cut **(Left)** with χ^2 and $c\tau$ cut **(Right)** for opened mass region.

What we need to compare eventually is $M(\Lambda_1\Lambda_2)$ and MC need to agree with real data for this. Fig. 3.31 histogram shows the $\Delta\ M = M(\Lambda_1\ \Lambda_2) - M(\Lambda_1) - M(\Lambda_2)$ **(left)** for data (black line) and inclusive MC (red line) for surviving and $\Delta\ M = M(\overline{\Lambda_1}\ \overline{\Lambda_2}) - M(\overline{\Lambda_1}) - M(\overline{\Lambda_2})$ **(right)** with blind region which is empty bins in near zero. Left panel shows reasonable agreement between real data and MC as Fig. 3.30. The $\bar{\Lambda}\bar{\Lambda}$ data distributions in right panel have different tendency between real data and MC in the low mass region as in Fig. 3.31 **(right)**.

Because particles generated in detector are almost hadrons with quarks not anti-quarks, So we can't explain more background in $\bar{\Lambda}\bar{\Lambda}$ data samples by this assumption. Investigation show that this deficit is mostly happend by

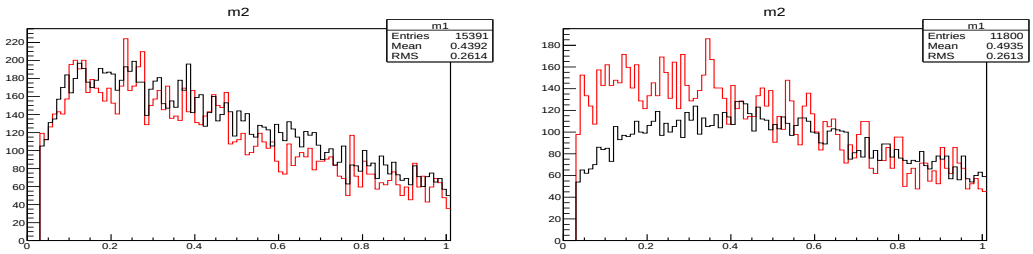

Figure 3.31: The black (red) histogram shows the $\Delta M = M(\Lambda_1\Lambda_2) - M(\Lambda_1) - M(\Lambda_2)$ **(left)** and $\Delta\bar{M} = M(\bar{\Lambda}_1\bar{\Lambda}_2) - M(\bar{\Lambda}_1) - M(\bar{\Lambda}_2)$ **(right)** distributions for data (inclusive MC) events. The regions below 0.03 GeV are blinded.

$\bar{\Lambda}\bar{\Lambda}$ combinations where at least one of the $\bar{\Lambda}$s has momentum below 1GeV. Fig. 3.32 show $M(\bar{\Lambda}\bar{\Lambda})$ distribution with $p(\bar{p_2})$, i.e, second anti-proton's momentum cut that **(left)** histogram with $p(\bar{p_2}) < 1\ GeV$ and **(right)** histogram with $p(\bar{p_2}) > 1\ GeV$. Red line histogram is real data and black line histogram is inclusive MC. This effect only generated in $\bar{\Lambda}\bar{\Lambda}$ sample with momentum below 1GeV and the other all show reasonable agreement between real data and MC. The $\bar{p}$-nucleus (and, presumably, the $\bar{\Lambda}$-nucleus) cross section grow rapidly at low $\bar{p}$ momentum and it is possible that this is not properly modeled in the MC simulation. By this effect, correct anti-particle tracking by energy loss is failed and eventually failed to pass basic cut requirements. You can check cross section in PDG figure [46]. We couldn't find other reason for this discrepancy.

Given the agreement between data and MC at this stage and understanding about discrepancy, we can have confidence that the contributions to the background in the data is resonably well modelled by the MC. We used the truth-table information to the data is resonably well modelled by the MC that remained after the above-listed requirements were applied. We found that 77% of the remaining events were due to real $\Lambda\Lambda$ pairs and , therefore,

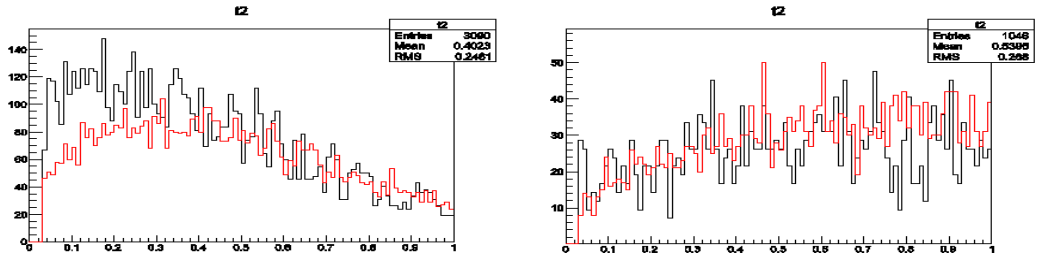

Figure 3.32: $M(\bar{\Lambda}\bar{\Lambda})$ distribution with $p(\bar{p_2}) < 1\ GeV$ **(left)** and $p(\bar{p_2}) > 1\ GeV$ **(right)**; Black line histogram is for inclusive MC and red line histogram is for $\Upsilon(1S)$ real data.

an irreducible background.

The requirements for the $\Lambda - \Lambda$ search are listed in Table. 3.4. The MC-determined selection efficiencies by averaging $\Upsilon(1S)$ & $\Upsilon(2S)$ signal MC are $\epsilon^{acc} = 10.9\%$ for $H \to \Lambda\Lambda$ and $\epsilon^{\bar{acc}} = 10.1\%$ for $\bar{H} \to \bar{\Lambda}\bar{\Lambda}$.

Before open the box, we need to check fitting function and expected distribution in blind box region. For fitting signal, A Gaussian-broadened BW function [49] is used with several fixed width and fixed resolution which studied by signal MC, plus an ARGUS-type function [50] to represent the background. Fig. 3.33 **(left)** show fitted function and data. Black dots are signal and inclusive MC and blue line is fitted PDF. Fig. 3.33 **(right)** show data without blind region (blue painted), inclusive MC (Red painted), and signal MC added with inclusive MC (colorless).

Table 3.4: A listing of the $\Lambda_1\Lambda_2$ selection requirements.

Particle	Quantity	Requirement
Λ_1 ($\bar{\Lambda}_1$)	$\mathcal{R}(p\|h^+)$	≥ 0.1
	ΔM_{Λ_1}	$\leq \pm 2\Gamma^{resol}_{\Lambda\to p\pi}$
	goodvee	1 or 2
$\Lambda_1\Lambda_2$ ($\bar{\Lambda}_1\bar{\Lambda}_2$)	$\mathcal{R}(p\|h^+)$	≥ 0.1
	$c\tau_{\Lambda_2}$	≥ -0.5 cm
	ΔM_{Λ_2}	$\leq \pm 2\Gamma^{resol}_{\Lambda\to p\pi}$
	$\chi^2_{\Lambda_1\Lambda_2}$	≤ 200
	$M(\pi_1\pi_2)$	≥ 288 MeV
	$M(p_1p_2)$	≥ 1878 MeV
	$N_{\rm hits}(p_1p_2)$	≥ 60
	multiple entries	
	$\chi^2_{\Lambda 1\Lambda_2}$	smallest

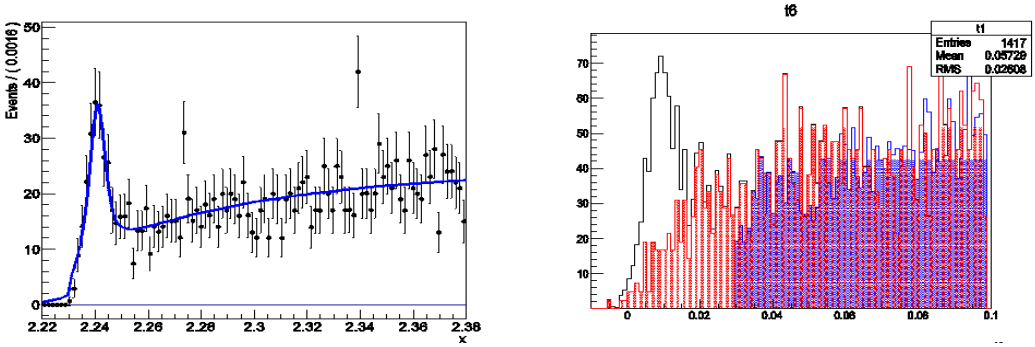

Figure 3.33: $M(\Lambda\Lambda)$ distribution of signalMC ($B(\Upsilon(1S) \to HX) = 4. \times 10^{-5}$) with inclusiveMC. **left:** shows fitted results using aGaussian-broadened BW function for signal and ARGUS-type function for background fitting; **right:** shows comparision between MC and blinded $\Upsilon(1S)$ real data sample. Blue painted histogram is blinded real data and other is MC.

3.4.3 efficiency and resolution estimation

efficiency estimation

When we estimate efficiency for H-dibaryon search, we need to use signal MC generated with same property of H-dibaryon. The meaning of efficiency in here is detection efficiency, i.e, probability that an event leads to some measured value. We can easily think that total efficiency is multiple of several detector and requirement efficiency. Eventually we can use formula for $H^0 \rightarrow \Lambda\Lambda$ channel as

$$\epsilon_T = \frac{N_{\rm det}(H)}{N_{\rm gen}(H) 2\mathcal{B}(\Lambda \rightarrow\ p\pi)}. \tag{3.5}$$

If MonteCarlo explain real data well, we can use this value with trust. But as you remember, inclusive MC of $\bar{\Lambda}\bar{\Lambda}$ selection shows discrepency to compare with real data. To account for this, we need to give some factor which will give exact efficiency. We compare the signal yields of real $\Lambda\Lambda$ and $\bar{\Lambda}\bar{\Lambda}$ determined from two-dimensional fits to a $M(p_1\pi_1^-)$ *vs.* $M(p_2\pi_2^-)$ and a $M(\bar{p}_1\pi_1^+)$ *vs.* $M(\bar{p}_2\pi_2^+)$ scatterplot. In here, we used two-dimensional BW formula added with polynomial background. You can see distribution of this in $\Lambda\bar{\Lambda}$ two-dimension fitting in Fig. 3.34. Left upper panel shows $M(\Lambda_1 : \Lambda_2)$ distribution (blue histogram) and fitting function (red lines). In horizontal plane, x-axis is $M(\Lambda_1)$ and y-axs is $M(\Lambda_2)$. The vertical axis(z-axis) is number of events. Low two histogram is projection of $M(\Lambda_2)$ and $M(\Lambda_1)$ with fitting function. Right panal's figures are about $\bar{\Lambda}\bar{\Lambda}$ channel distribution same as left panel. Signal yield is fraction which comes from both BW fitted fraction.

Without detector effect, generated yields should be equal. But because of detector effect, we will get ratio between yields of real $\Lambda\Lambda$ and $\bar{\Lambda}\bar{\Lambda}$ which is bigger than 1. When we estimate efficiency, we used Monte Carlo and simulation which is used for making Monte Carlo already have detector performance and cross-section. So correction factor what we will use need to

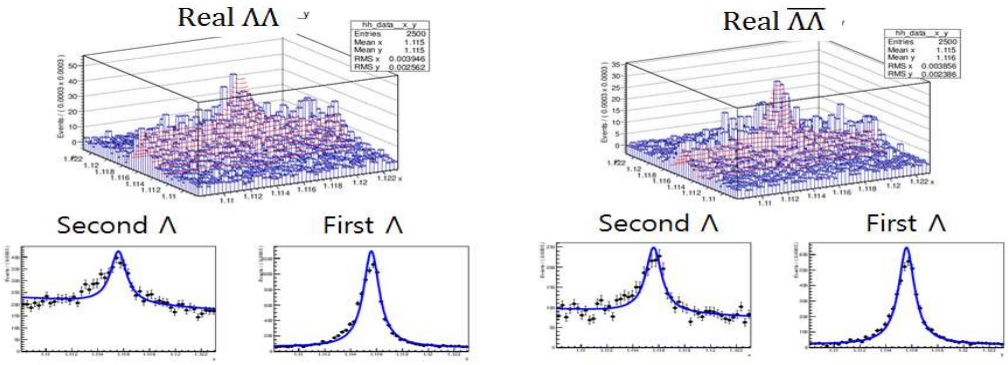

Figure 3.34: Upper two histogram shows two dimensional distribution of $M(p_1\pi_1^-)$ *vs.* $M(p_2\pi_2^-)$ **(left)** and $M(\bar{p}_1\pi_1^+)$ *vs.* $M(\bar{p}_2\pi_2^+)$ **(right)**. Red lines in histogram shows fitted function of two dimensional function (gaussian(x) + polynomial(x))×(gaussian(y) + polynomial(y)). lower two histograms in each panel are projection distribution for $M(p_1\pi_1^-)$ and $M(p_2\pi_2^-)$.

divide by efficiency ratio $\epsilon_H/\epsilon_{\bar{H}}$. Eventually efficiency correction factor R is

$$R_{\bar{\Lambda}\bar{\Lambda}} = (\frac{N_{\bar{\Lambda}\bar{\Lambda}}}{N_{\Lambda\Lambda}})/(\frac{\epsilon_{\bar{H}}}{\epsilon_H}). \tag{3.6}$$

We determine a correction factor $R = 0.83 \pm 0.13$ for the $\bar{\Lambda}\bar{\Lambda}$ acceptance value and use this corrected value in the branching fraction limit determination. The error on this ratio is included as a systematic error.

resolution estimation

Before open the box, we need to care resolution more carefully. What we know is estimated resolution from signal MC, this value will similar with real data as we checked MC performance in Section 3.3.3. For precise measurement of H-dibaryon, we need to get exact resolution value for fitting. Because we have Ξ^- and $\Xi_c^0(2470)$ resonance, which doesn't have width. Especially we have enough data of Ξ^- resonance to ignoring statistical error. Resolution

correction factor f is resolution fraction of real dat and MC. We got correction factor for particle channel and anti-particle channel seperately. The f correction factor from $\Xi_c^0(2470)$ is 0.801 $\pm$ 0.096 and Ξ^- is 0.851 $\pm$ 0.004. Two value is in 1 σ difference, so we can use $f_{par} = 0.851 \pm 0.004$. About anti-particle channel, f correction factor is $f_{par} = 1.12 \pm 0.01$. When we search H-dibaryon with strong decay, resolution effect can be small if H-dibaryon has large width. Efficiency of signalMC are $\epsilon^{acc} = 10.9\%$ for $H \to \Lambda\Lambda$ and $\epsilon^{\bar{a}cc} = 10.1\%$ for $\bar{H} \to \bar{\Lambda}\bar{\Lambda}$ as mentioned before section and we need to multiple correction factor to these values.

One more thing what i need to mention is way to calculate resolution of signal from $\Upsilon(1S)$ and $\Upsilon(2S)$ both. For finding H-dibaryon, we need to add $\Upsilon(1S)$ and $\Upsilon(2S)$ data for statistics. So some signal come from $\Upsilon(1S)$ and other come from $\Upsilon(2S)$. Total efficiency will be

$$\epsilon_T = \frac{N_{\Upsilon(1S)}\epsilon_{\Upsilon(1S)} + N_{\Upsilon(2S)}\epsilon_{\Upsilon(2S)}}{N_{\Upsilon(1S)} + N_{\Upsilon(2S)}}. \tag{3.7}$$

as you can calculate from 3.5. Efficiency of $\Upsilon(1S) \to H^0X$ & $H^0 \to \Lambda\Lambda$ signal MC is 0.121 and efficiency of $\Upsilon(2S)$ to same decay is 0.102. Efficiency of $\Upsilon(1S) \to \bar{H^0}X$ & $\bar{H^0} \to \bar{\Lambda}\bar{\Lambda}$ signal MC is 0.111 and efficiency of $\Upsilon(2S)$ to same decay is 0.098. The reason of efficiency difference between $\Upsilon(1S)$ and $\Upsilon(2S)$ would be final particles momentum difference.

3.5 Λ $p\pi$ selection

If the mass of the H^0 is just below $2m_\Lambda$, it would decay via weak interactions with a similar lifetime of τ_Λ and the dominant decay modes would include $H^0 \to \Lambda\ p\pi$, $H^0 \to \Sigma^- p$, $H^0 \to \Sigma^0 n$ and $H^0 \to \Lambda\ n$. We search for the $H \to \Lambda p\pi^-$ decay mode using modified version of the selection requirements applied for the serach in the ΛΛ mode.

3.5.1 mc simulation

For studying $H^0 \to \Lambda p\pi$ decay channel, we need to choose possible cut parameters. As we studied ΛΛ selection section, it's hard to give cut requirement about parameters of reconstructed H-dibaryon candidate itself. So it is important select pure Λ, p and π samples. Because we already studied Λ selection with high efficiency and good performance. Using inclusive MC with one half amount of real data, we first see the distribution of M(Λ $p\pi$) for checking background distribution. With Λ selection requirements and a loose proton particle ID selection for the accompanying proton: $\mathcal{R}(p|\pi^+) \geq 0.1$ and $\mathcal{R}(p|K^+) \geq 0.1$, $M(p\pi^-) < m_\Lambda$ and a Λ $p\pi^-$ vertex cut of $\chi^2 \leq 50$ (discussed below) to the inclusive MC sample, we get the Λ $p\pi$ invariant mass distribution shown as the upper histogram in the Fig. 3.35 **(left)**, where a fake peak is evident. We can give $M(p\pi^-)$ cut for proton and π which directly decay from H^0 because if $M(p\pi^-)$ is above Λ mass, it means H^0 will strongly decay to ΛΛ. So we don't need to care above $2m_\Lambda$ in here. Expected source of this background was duplicated particle track effect as before. When we select only samples which doesn't have duplicated proton and π tracks using truth table, we can get lower histogram. In Λ $p\pi$ channel, we can see duplicated track background give big effect around entire mass region. So not only subtracting bump but also reduce background itself, we need to give attention for duplicated track background.

Fig. 3.36 **(left)** show M(pp) distribution of signalMC (shaded), inclusive

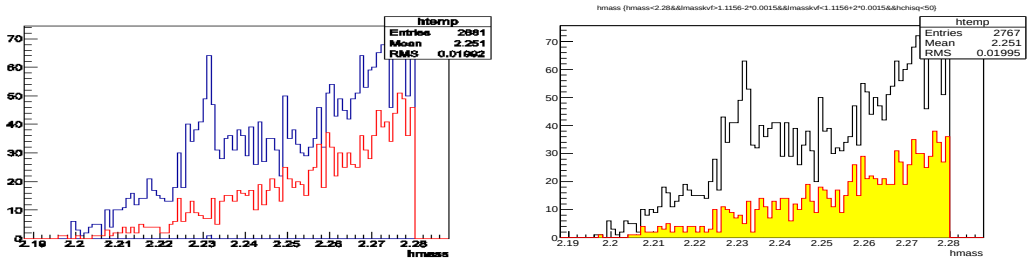

Figure 3.35: Results after application of minimal $\Lambda p\pi^-$ selection requirements to the inclusive MC sample. The $M(\Lambda p\pi^-)$ distribution: **left:** the upper(lower) histogram is before (after) the application of the same-track rejection by truth table. **right:** the open (shaded) histogram is before (after) the application of the same-track rejection requirements described in the text.

MC (open black line) and inclusive MC without duplicated tracks by using truth table(open blue color line). In open black line histogram, a sharp peak near $2m_p$ is evident and the lower blue color line histogram shows the results with same-track entries identified from the MC truth table are rejected. Fig. 3.36 **(center)** show $N_{trk}(pp)$ distribution which is added number of two proton CDC hits. Black colored histogram is inclusive MC without signalMC, right light colored histogram is signal MC and left mild colored small histogram is duplicated track background.

We need to decide cut values using these two parameter. But both cut criteria will reduce signal efficiency because of overlap between signal and duplicated track background as you can see in Figure. When we see N_{hit} distribution, signal MC region be decreased compare with $\Lambda\Lambda$ channel and reason would be the life-time of H^0.

When we select cut value, we checked background bump number and signal efficiency both as Fig. 3.37 **left (upper)** graph is number of background bump for $M(pp)$ cut value and **left (lower)** graph is efficiency of signal MC

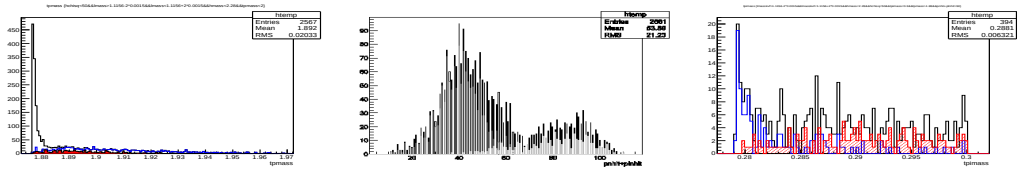

Figure 3.36: Results after application of minimal $\Lambda p\pi^-$ selection requirements to the inclusive MC sample. **left:** The $M(pp)$ distribution. **center:** The $N_{hit}(pp)$ distribution. **right:** The $M(\pi^-\pi^-)$ distribution after the requirements $M(pp) > 1.878$ GeV and $N_{hit} > 50$.

for same cut with upper. **right** graph is same as left but cut parameter is $N_{trk}(pp)$. What we need to choose value is reduce background as many as possible with high signal efficiency. Both cut parameter show steep decrease shape for background and gradual decrease of efficiency. From these graphs, we can choose cut vales as $M(pp) > 1.878$ GeV and $N_{hit} > 50$. About $M(\pi^-\pi^-)$ cut, we can give requirement $M(\pi^-\pi^-) > 0.28$ GeV to remove anomalous peak near $2m_\pi$ from Fig. 3.36 **(right)**.

After giving these all cut requirement, you can see gentle background distribution in Fig. 3.35 **(right)**. Painted histogram is after rejection by cut requirement and upper open histogram is before. There's no more anomalous structure.

Now we need to see other cut parameters which is used for reducing miscombination between Λ, p and π. We checked many kinds of parameters like $\cos\theta$ between p_Λ and p_p, dr & dz for p, π, and decay length, etc. But only χ^2 of vertex fitting of Λ, p and π tracks and $c\tau_{\Lambda p\pi}$ is helpful. Although we can expect $\cos\theta$ need to be helpful by same direction because of small mass difference between mother particle and daughter particles but it's not useful because background also have similar tendency.

In Fig. 3.38, the left panel shows χ^2 distribution for inclusive MC event as a blue line histogram and that for signal MC as a lower red colored line

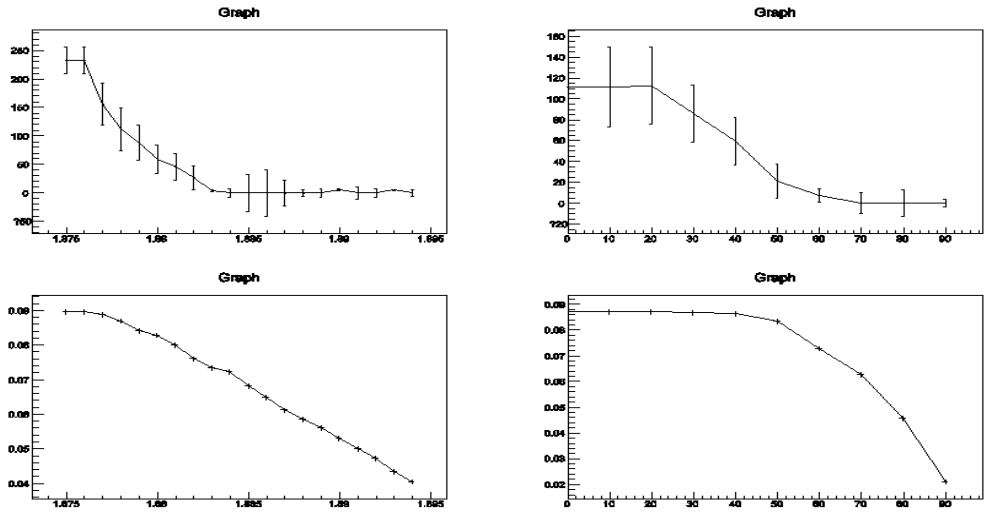

Figure 3.37: **(left upper)** graph is number of background bump for $M(pp)$ cut value and **(left lower)** graph is efficiency of signal MC for same cut with upper**(right)** graph is same as left with $N_{trk}(pp)$ cut parameter

histogram. With this histogram, you can see right side upper panel which shows a FoM for a χ^2 cut assuming a signal efficiency varies with the χ^2 cut value. The requirements $\chi^2 < 50$ gives the best FoM and signal efficiency.

In Fig. 3.39, the left panel shows $c\tau_{\Lambda p\pi}$ distirbution for inclusive MC event as a black line histogram and that for signal MC as a red colored line histogram. Right side panel shows a FoM *versus.* $c\tau$ cut distribution. Followed by FoM, expectation H^0 life-time need to more than $c\tau_{\Lambda}$, the requirements $c\tau_{\Lambda p\pi} > 0$ is decided.

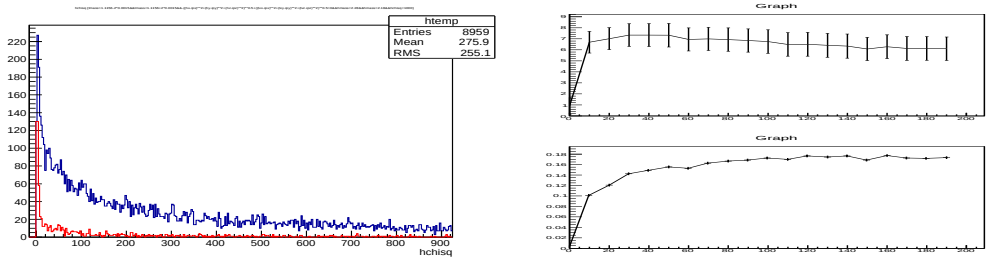

Figure 3.38: **Left:** The χ^2 distribution for the $\Lambda p\pi^-$ vertex fit for the signal (inclusive) MC samples is shown as a red (blue) histogram. **Right:** The FoM (signal efficiency) as a function of the maximun χ^2 requirement is shown in the upper (lower) figure.

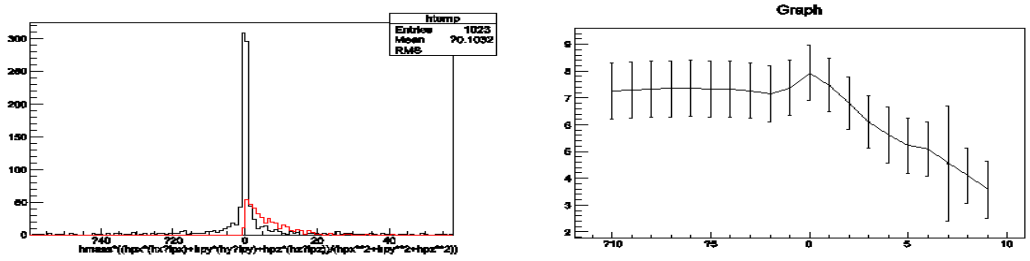

Figure 3.39: **Left:** The $c\tau$ distribution for the $\Lambda p\pi^-$ reconstructed sample for the signal (inclusive) MC samples is shown as a red (blue) histogram. **Right:** The FoM (signal efficiency) as a function of the maximun $c\tau$ requirement is shown.

3.5.2 data comparision

Like other channel study, real data need to compare with inclusve MC with blind box. The blind region is $M(\Lambda p\pi^-) < 2m_\Lambda (= 2.232$ GeV). The data are continuum-background subtracted. For comparison, we use an inclusive plus signal MC event sample that are combined assuming a branching fraction of 2.5×10^{-5}.

First, we studied events with multiple combinations sharing some of the same tracks using small subsample of different types of events. Multiple entries occur in about 10% of the MC events; they occur at a similar level in the data for the $\bar{H}^0 \to \bar{\Lambda}\bar{p}\pi^+$ channel but at the ∼22% level for the $H^0 \to \Lambda p\pi^-$ channel, as summarized in Table 3.5. The higher level in the $\Lambda p\pi^-$ data is due to secondary protons and Λs from interactions in the material of the beam-pipe and SVD, a background source that does not produce $\bar{\Lambda}$s or $\bar{p}$s. The major component of the multiple entries are the occasions when two protons and one π are used twice, which account for about 70% of all multiple entries. Multiple entries that use the same two πs and one or two different protons account for about 20% of the multiple entries. From multiple entries that share one or more tracks, we select the combination that has the best $\Lambda p\pi^-$ vertex fitting χ^2 value. For the signal MC, we find that this selection picks the correct combination 68% of the time. Same as other channel, multiple combination effect is very small. But we need to alert peaking background, so it is better to choose minimum χ^2 candidate.

The left (right) panel of Fig. 3.40 shows the $M(\Lambda p\pi^-)$ ($M(\bar{\Lambda}\bar{p}\pi^+)$) distribution for inclusive plus signal MC as a red histogram and data (for $M(\Lambda p\pi^-) > 2m_\Lambda$) as a blue histogram. While the agreement between data and MC is reasonable for the $\bar{\Lambda}\bar{p}\pi^+$ channel, the $\Lambda p\pi^-$ data shows a large excess of events relative to the MC. Possible sources for this discrepancy include: **1)** an incorrect MC generator coupled with probles with the simulation of low-energy $\bar{p}$- and $\bar{\Lambda}$-nuclei interactions in the material of the beam-pipe and SVD; and/or **2)** backgrounds from low energy protons and Λs produced

Table 3.5: A summary of multiple entry events. Here "Data" corresponds to data events in the mass range $2m_\Lambda < M(\Lambda p\pi^-) < 2.28$ GeV.

Channel	Sample	Total Entries	single entries	2 entries	≥ 3 entries
$\Lambda^0 p\pi^-$	Data	4202	3296 (78%)	495	115
	Signal MC	382	328 (86%)	46	8
	Inclusive MC	491	445 (91%)	42	4
$\bar{\Lambda^0}\bar{p}\pi^+$	Data	1252	1144 (91%)	93	15
	Signal MC	374	324 (87%)	42	8
	Inclusive MC	412	387 (94%)	24	1

by particle interactions in the material of the beampipe and SVD.

For investigating our expectation, we can see momentum distribution because both case will show discrepency in momentum distribution between real data and inclusiveMC. Fig. 3.41 show momentum distribution that blue line histogram is real data after continuum subtraction and red color line histogram is inclusive MC. As you can see anti-particles in real data quite agree with MC. Problem arise only particle channel below 1GeV region. It means that the source of discrepancy is low energy particle produced inside beam detector which is **2)** in upper sentence.

To sure about this expectation, we also see other parameters as in Fig. 3.42. In histogram, blue colored open histogram is real data, red colored open histogram is inclusive MC and painted small histogram is signal MC. From the dr(p) distribution, we can confirm existance of beam background that real data have many samples which have large dr value and beam background particle generated in beam-pipe or detector with random direction so dr can be large. From the momentum and $c\tau_\Lambda$, we also know many Λ generated as beam background.

We also can use beam asymmetry effect. It means that because our beam

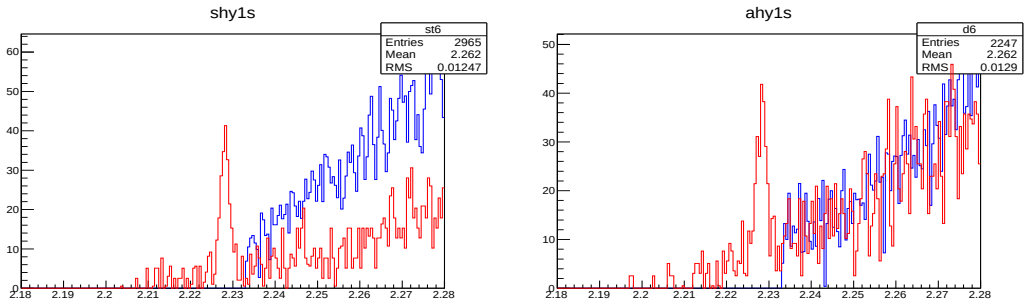

Figure 3.40: **Left** The $M(\Lambda p\pi^-)$ distribution for events satisfying the selection requirements described in the text. The red histogram is for signaal plus inclusive MC; the blue histogram is for data with the $M(\Lambda^0 p\pi^-) \leq 2m_\Lambda$ region blinded. **Right:** The corresponding $M(\bar{\Lambda}\bar{p}\pi^+)$ distributions.

is asymmetry, particles generated by e+e- collision will show symmetry in CM frame but background which is generated in detector will be asymmetry. But it's hard to see difference in lab frame because beam background also have small lean to beam direction. You can check this expectation is right in Fig. 3.43.

Fig. 3.43 **(left)** show $cos\theta$ between z-axis and p_Λ in CM frame of beam and Fig. 3.43 **(right)** is same parameter in Lab frame. Blue lined opend histogram is real data, red colored line histogram is inclusive MC and painted histogram is signal MC. Now the problem is finding best way to reduce this distrepency and save efficiency. cut parameter what we choose is lab frame momentum cut for Λ and proton.

The left panel of Fig. 3.44 shows how the signal efficiency (vertical axis) varies with the background rejection efficiency (horizontal axis) for different requirements on the minimum Λ and proton momenta. The right panel shows signal efficiency (vertecal) *versus* number of MC and number of real data's ratio (horizontal) for checking. The different colors indicate different minimum proton momentum requirements: (black, red, light-green, blue,

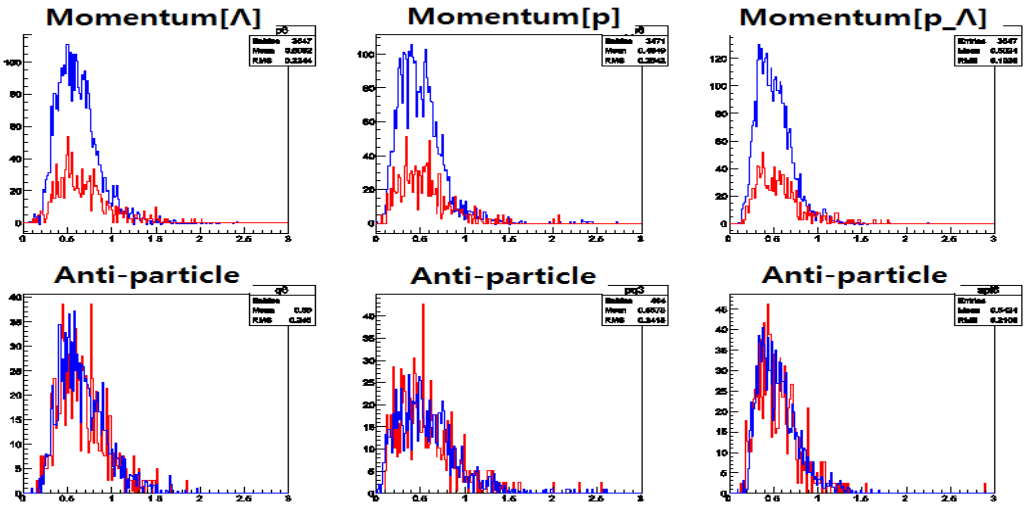

Figure 3.41: Momentum distribution of **upper(lower) left:** $\Lambda(\bar{\Lambda})$; **upper(lower) middle:** $\mathrm{p}(\bar{p})$; and **upper(lower) right:** $p_\Lambda(\bar{p}_{\bar{\Lambda}})$. Red line histogram is for inclusiveMC and blue line histogram is fro $\Upsilon(1S)$ real data sample.

yellow, pink, sky-blue, green, ocean-blue, grey) = (0, 0.1, 0.2, 0.3, 0.4, 0.5, 0.6, 0.7, 0.8, 0.9) GeV. Points of the same color correspond to minimum Λ momentum requirements for 0.1 GeV steps starting at zero. We choose the requirements $p_{\mathrm{proton}} > 0.5$ GeV and $p_\Lambda > 0.5$ GeV, which have $\sim 80\%$ efficiencies both for signal retention and for background rejection. This cut also give ratio between MC and real data be 80% agreement. I need to mention that points below 0.5 for signal efficiency has only small number of samples for inclusive MC. So it's not reliable. We give momentum only Λ $p\pi$ channel not anti-particle channel. After this cut, there is resonalbe agreement between data and MC.

We checked other possible cut parameters like $cos\theta$ in CM frame, $cos\theta$ & momentum cut both and proton momentum cut only with same strategy. But best requirements was $p_{\mathrm{proton}} > 0.5$ GeV and $p_\Lambda > 0.5$ GeV.

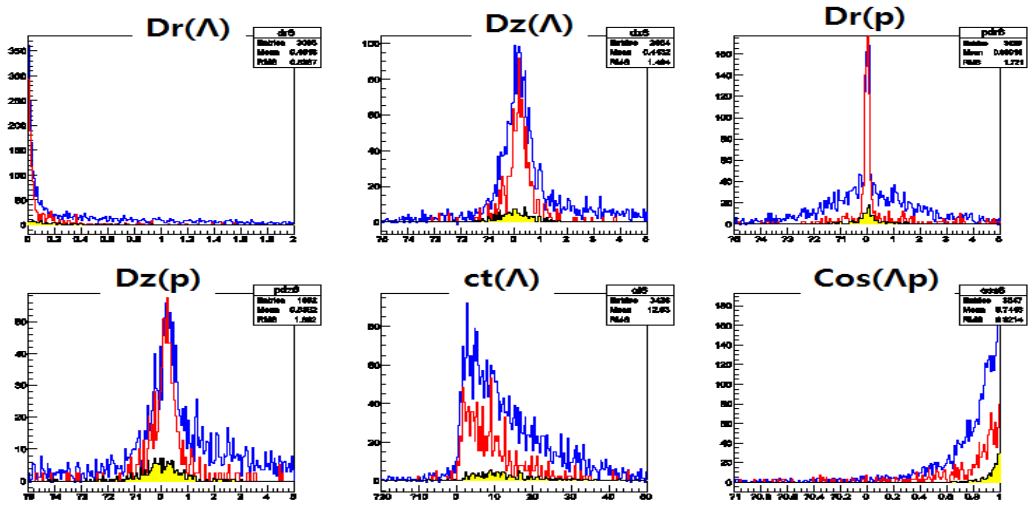

Figure 3.42: From left with clockwise rotation, dr(Λ), dz(Λ), dr(p), dz(p), $c\tau_\Lambda$, and cos($p_p \cdot p_\Lambda$); Blue line is real data, Red line is inclusiveMC and yellow painted histogram is signalMC.

Given the agreement between data an MC at this stage, we can have some confidence that the contributions to the background in the data is reasonably well modeled by the MC. We used the truth-table information to determine the types of events in the inclusive MC that remained after the above-listed requirements were applied. We found that 47% of the remaining events were due to real $\Lambda p\pi^-$ combinations and irreducible. Most of the other entries had one or more particles misidentified. We found that these could be reduced by 78% with a 9% loss in real $\Lambda p\pi^-$ events by more stringent particle id requirements for the proton and π^-: the proton id cut was tightened from $\mathcal{R}(p_2|h^+) \geq 0.1$ to $\mathcal{R}(p|h^+) \geq 0.9$ ($h^+ = \pi^+$ or K^+), a loose π id requirement was added $\mathcal{R}(\pi^+|K^+) \geq 0.6$. There is some contamination from electrons that is removed by an electron veto requirement: $\mathcal{R}(e|\pi) \leq 0.1$. According to the MC, with these added requirements the remaining background is $\sim 73\%$ due to real $\Lambda p\pi^-$ pairs.

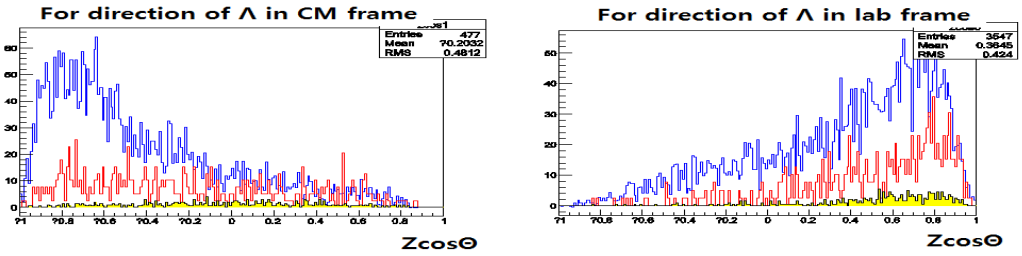

Figure 3.43: **left:** $cos\theta$ between z-axis and p_Λ in CM frame; **right:** $cos\theta$ between z-axis and p_Λ in Lab frame.

Fig. 3.45 **Left (right)** shows mass distribution $M(\Lambda\ p\pi^-)$ ($M(\bar{\Lambda} p\pi^+)$) after using all cut requirements. Blue colored line historgram shows real data without data points in blind box region and red colored line histogram shows signalMC samples added to inclusive MC which is scaled as real data amount. Signal MC is also scaled to $\mathcal{B}(\Upsilon(1S) \to H^0X) = 2.5 \times 10^{-5}$. Inclusive MC in matched region with real data looks quite agreement and distribution loos gentle without fluctuation. Compare with Fig. 3.40, Background is extremly decreased and signal MC is dominant. One more important point is small difference between inclusive MC and real data. This difference in anti-particle channel is already studied in $\bar{\Lambda}\Lambda$ sample. Next section will deal with this. The final selection efficiencies are determined fom MC to be $\epsilon_1^{\rm acc} = 8.3\%$ for $H \to \Lambda p\pi^-$ and $\bar{\epsilon}_1^{\rm acc} = 9.0\%$ for $H \to \bar{\Lambda}\bar{p}\pi^+$.

The selection requirements for the $\Lambda p\pi^-$ searches are summarized in Table 3.6.

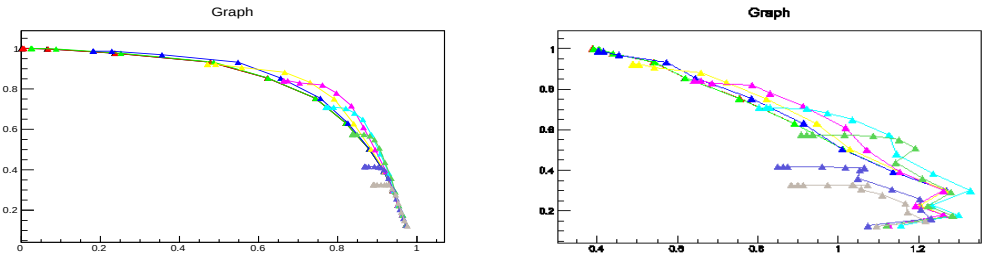

Figure 3.44: **Left** The signal efficiency (vertical) *versus* background rejection efficiency (horizontal) for different minimum Λ and proton laboratory frame momentum requirements. The color coding is described in the text. The pink points are for minimum Λ momentum requirements in 0.1 GeV increments starting at zero (at the left) for $p_{\text{proton}} > 0.5\ GeV$. **Right:** The signal efficiency (vertecal) *versus* number of MC and number of real data's ratio (horizontal) for different minimum Λ and proton laboratory frame momentum requirements.

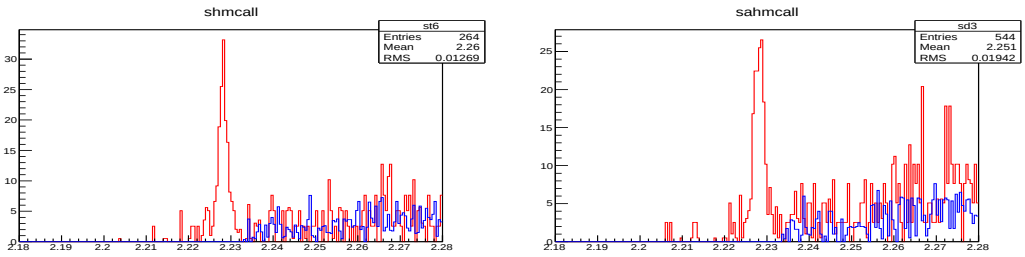

Figure 3.45: $M(\Lambda\ p\pi^-)(M(\bar{\Lambda}\bar{p}\pi^+))$ distribution of MC(red line) and $\Upsilon(1S)$ real data sample with blind box.; signal MC has $\mathcal{B}(\Upsilon(1S) \to H^0X) = 2.5 \times 10^{-5}$.

Table 3.6: A listing of the $(p\pi^-)$ selection requirements.

Particle	Quantity	Requirement
Λ_1 ($\bar{\Lambda}_1$)	$\mathcal{R}(p\|h^+)$	≥ 0.1
	ΔM_{Λ_1}	$\leq \pm 2\Gamma^{resol}_{\Lambda\to p\pi}$
	goodvee	1 or 2
$\Lambda p\pi^-$ ($\bar{\Lambda}\bar{p}\pi^+$)	$\mathcal{R}(p\|h^+)$	≥ 0.9
	$\mathcal{R}(\pi^-\|K^-)$	≥ 0.6
	$\mathcal{R}(e\|\pi^-)$	≤ 0.1
	$c\tau_{p\pi^-}$	≥ 0.0 cm
	$\chi^2_{\Lambda p\pi^-}$	≤ 50
	$M(\pi_1\pi_2)$	≥ 28 MeV
	$M(p_1p_2)$	≥ 1878 MeV
	$N_{\rm hit}(p_1p_2)$	≥ 50
	multiple entries	
	$\chi^2_{\Lambda p\pi^-}$	smallest
	$\Lambda p\pi^-$ mode only	
	p_Λ	≥ 0.5 GeV
	$p_{\rm proton}$	≥ 0.5 GeV

3.5.3 effieciency and resolution estimation

As mentioned in Section 3.4.3, low momentum anti-particle efficiency can be differ with MC estimation by attribution of improper modeling of the effect of the large cross-section in material. We save low momentum particles in $\bar{H^0} \rightarrow \bar{\Lambda}\bar{p}\pi^+$ differ with $H^0 \rightarrow \Lambda p\pi^-$ channel which have momentum cut 0.5GeV. So we need to use R correction factor also in efficiency of $H^0 \rightarrow \Lambda p\pi$ decay channel. When we get the R correction factor, we used number of two Λ sample with enough statistics. If we try to use number of Λ, p and one π in here, it's not easy. Because particle Identification is not an absolute division factor of particle, we can't know or select exact one proton, π differ with select two Λ. So we need trick that because two Λs also decay to two protons and two πs, we can use same correction factor which is used in ΛΛ sample. Of course, we checked agreement of this R factor with R factor from $\Lambda p\pi$ sample with tight particle ID selection and result was similar.

Differ with strongly decaying exotic particle search, in here, we need to care about life-time of H-dibaryon. Efficiency what we got from signalMC is for H-dibaryon with $c\tau_H = 7.89cm$ which is same as $c\tau_\Lambda$. If life-time of H-dibaryon is smaller than Λ, we can expect more efficiency because daughter particles (proton and π) make track more early, track reconstruction and particle ID accuracy be more. Because H-dibaryon is expected life-time is more than Λ, we don't care about this. But oppositly if life-time of H-dibaryon is larger than Λ, efficiency be smaller and we need to care about this. Expected mass region in our search is between $m_\Lambda + m_p + m_\pi$ and $2m_\Lambda$. Differ with expected long life-time H-dibaryon with tight bound energy which much below than $2m_\Lambda$, near $2m_\Lambda$ H-dibaryon would have short life-time that we can expect. But for sure we also checked efficiency for long life-time H-dibaryon using signalMC.

For H-dibaryon with $c\tau_H = 2 \times c\tau_\Lambda$, efficiency is 6.9 (7.2)% and for H-dibaryon with $c\tau_H = 5 \times c\tau_\Lambda$, efficiency is 3.7 (4.2)% We can see if H-dibaryon's life-time is 5 times of Λ's life-time, efficiency be half. We need to

keep in mind about this.

About resolution, we give same f correction factor to estimated resolution value from signalMC. You can see detail in Section. 3.4.3.

3.6 $\Xi^- p$ selection

For searching H-dibaryon in mass region above $m_{\Xi^-} + m_p$, we checked $\Xi^- p$ decay channel. We can use all cut criteria which already studied using $\Xi^{*0}(1530)$ resonance except π_3 particle ID selection cut. (This channel's box opening was done faster than $H^0 \to \Lambda\Lambda$ channel. i mean after searching above $m_{\Xi^-} + m_p$ region by $\Xi^-\pi^+$ control sample study, we studied below $m_{\Xi^-} + m_p$ blinded for $\Lambda\Lambda$ channel study and compare real data and MC using above $m_{\Xi^-} + m_p$ region for analysis. Same strategy is used to $\Lambda\ p\pi$ channel)

3.6.1 mc simulation

We use same $\Xi^-\pi$ selection criteria in here for Λ parameters and Ξ^- parameters. For last proton p_2, we use same dr, dz and χ^2 cut value. For particle Identification, we give likelihood ratio be more than 0.9 as $\mathcal{R}(p|\pi^+) \geq 0.9$ and $\mathcal{R}(p|K^+) \geq 0.9$. One more parameter we need to check is duplicated track parameters.

Fig. 3.46 **(left)** shows $M(pp)$ distribution using signal and inclusive MC. Opened histogram with black line is inclusive MC, painted peak in leftside is duplicated proton background and opend histogram with red color line is signalMC. **Right** panel shows $N_{hits}(pp)$ distibution with opened histogram with darker line is inclusive MC, mild color line is signalMC and painted small histogram in leftside is duplicated particle background. By giving cut value $M(p_1p_2) \geq 1878$ MeV and $N_{\rm hit}(p_1p_2) \geq 60$, we can reject duplicated particle background with enough efficiency. Table. 3.7 shows all requirements.

Before box opening, we need to compare mass distribution of $M(\Xi^- p)$

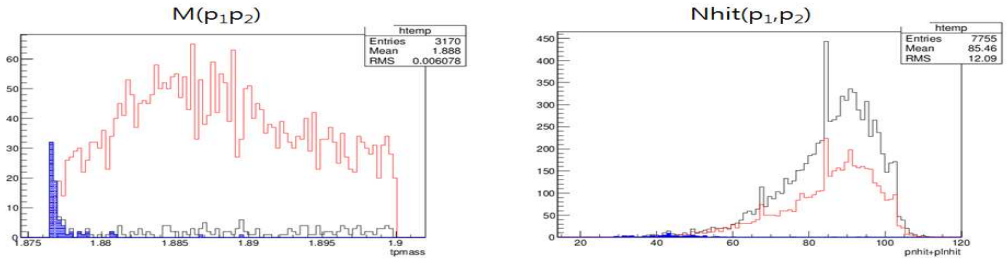

Figure 3.46: **Left** $M(p_1p_2)$ distribution of MC and **right** $N_{hit}(p_1p_2)$ distribution of M; Red line histogram is signal MC and lower black line histogram is inclusive MC. Painted part in inclusive MC histogram is duplicated track background.

between MC and real data. Fig. 3.47 shows mass distribution with arbitrary scale factor. Because generated proton number in inclusive MC is not same with real data, we need to use arbitrary scale factor to inclusive MC. Continuum-subtracted $\Upsilon(1S)$ data sample fit well with inclusive MC in above blind box region.

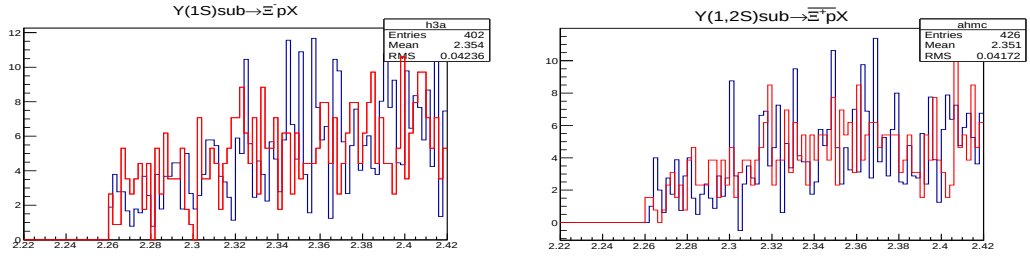

Figure 3.47: $M(\Xi^- p)$ distribution **(Left)** and $M(\bar{X}i^+\bar{p})$ distribution **(right)** with blind box in left of histogram. Red line histogram is inclusive MC with arbitrary scale factor and blue line histogram is $\Upsilon(1S)$ real data after continuum subtraction.

Table 3.7: A listing of the $\Xi^- p$ selection requirements.

Particle	Quantity	Requirement
Λ^0 ($\bar{\Lambda}^0$)		
	$\mathcal{R}(p\|\pi^+)$	≥ 0.1
	$\mathcal{R}(p\|K)$	≥ 0.1
	$c\tau_\Lambda$	no cut
	$\Delta M_{p\pi}$	$\leq \pm 2\Gamma^{resol}_{\Lambda\to p\pi}$
	goodvee	1 or 2
Ξ^- ($\bar{\Xi}^+$)		
	$c\tau_\Xi$	≥ 0.5 cm
	$\Delta M_{\Lambda\pi}$	$\leq \pm 2\Gamma^{resol}_{\Xi\to\Lambda\pi}$
	$\chi^2_{\pi^-_2}$	≤ 20
	$\|dz_{\pi^-_2}\|$	≤ 10 cm
$\Xi^- p$ ($\bar{\Xi}^+ p$)		
	$\chi^2_{\pi_3}$	≤ 20
	$dr_{\pi^+_3}$	≤ 0.2 cm
	$\|dz_{\pi^+_3}\|$	≤ 5 cm
	$\mathcal{R}(p\|\pi)$	≥ 0.9
	$\mathcal{R}(p\|K)$	≥ 0.9

3.6.2 efficiency and resolution estimation

Differ with before studies of H-dibaryon signalMC study, we need to care about efficiency and resolution which depend on mass. Expected mass region in here is from $m_{\Xi^-} + m_p$ to $2m_\Sigma$ and mass difference is $\Delta m_{\Xi^- p} \simeq 130 MeV$ which is larger compare with $\Delta m_{\Lambda\Lambda} \simeq 30 MeV$ and $\Delta m_{\Lambda p\pi} \simeq 40 MeV$. For studying about this effect, we made signalMC for each 10MeV and checked tendency of efficiency and resolution. We checked efficiency and resolution show linear increase for mass increase. Because $\Upsilon(1S)$ and $\Upsilon(2S)$ data will be added, we also made signalMC for $\Upsilon(2S)$ for each mass region. As you can see in Fig. 3.48, efficiency of total sample ϵ_T is getted by average of two linear efficiency line.

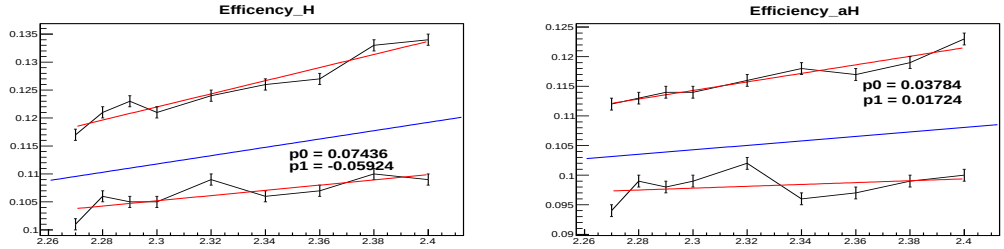

Figure 3.48: Efficiency *versus* H-dibaryon mass distribution for $H \to \Xi^- p$ channel **(Left)** and $\bar{H} \to \Xi^+ \bar{p}$ channel **(right)**; Lower graph is efficiency for $\Upsilon(1S)$ signalMC and higher graph for $\Upsilon(2S)$ signalMC. Blue line in middle is normalized efficency.

We can see efficiency difference for $\Upsilon(1S)$ and $\Upsilon(2S)$ decay. Differ with efficiency, resolution shows similar distribution of resolution. The reason would be affection of momentum to particle identification is big. As you can see Fig. 3.49, we can get resolution linear function for $\Xi^- p$ and $\bar{\Xi}^+ \bar{p}$.

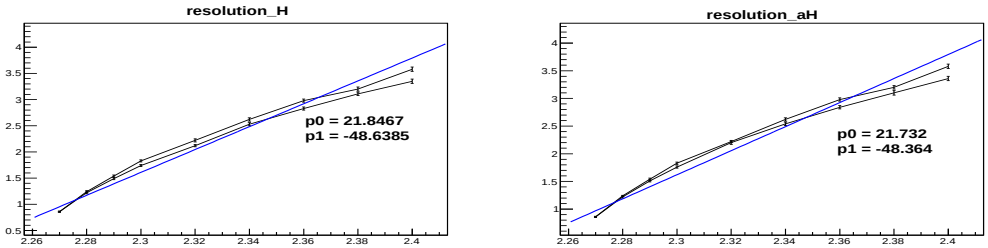

Figure 3.49: Resolution *versus* H-dibaryon mass distribution for $H \to \Xi^- p$ channel **(Left)** and $\bar{H} \to \Xi^+ \bar{p}$ channel **(right)**.

Chapter 4

Results & Discussion

4.1 Results for $\Xi^{*0}(1530)$ and $\Xi_c^0(2470)$ production

4.1.1 $\mathcal{B}(\Upsilon(1S) \to \bar{\Xi}^{*0}(1530)\ X)$

Since we used the $\Xi^{*0}(1530)$ resonance signal to optimize the event selection, we use the $\overline{\Xi^{*0}}(1530) \to \bar{\Xi}^{+}\pi^{-}$ signal channel, extracted with the same requirements, to determine the inclusive branching fraction $\mathcal{B}(\Upsilon(1S) \to \overline{\Xi}^{*0}(1530)\ X)$. Because we didn't blind $\Xi^{*0}(1530)$ and used itself to decide FoM, $\mathcal{B}(\Upsilon(1S) \to \Xi^{*0}(1530)\ X)$ would be bias. The continuum-subtracted $M(\bar{\Xi}^{+}\pi^{-})$ distribution near 1530 MeV is shown as data points in Fig. 4.1. The $\overline{\Xi}^{*0}(1530) \to \bar{\Xi}^{+}\pi^{-}$ signal yield is determined by binned χ^2 fit to the data that uses an ARGUS-lke function [50] to represent the background and a resolution-broadened Breit-Wigner function, a so-called Voigtian [49], to represent the signal. The results of the fit, shown as a smooth curve in

Fig. 4.1, is $N_{\rm evts} = 9148 \pm 161$ events.

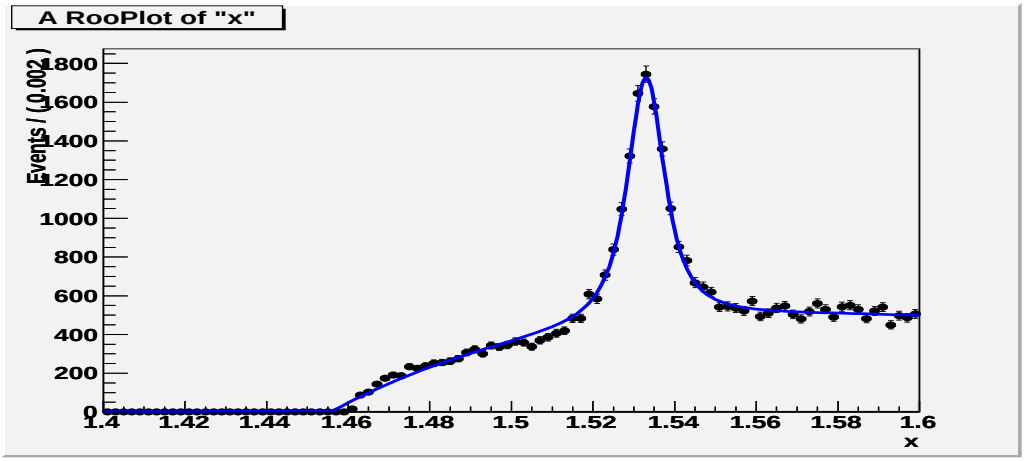

Figure 4.1: The data points show the continuum-subtracted $M(\bar{\Xi}^+\pi^-)$ distribution in the $\bar{\Xi}^{*0}(1530)$ region; the smooth curve shows the results of the fit described in the text.

The inclusive branching fraction is determined via the relation

$$\mathcal{B}(\Upsilon(1S) \to \bar{\Xi}^{*0}(1530)\ X) = \frac{N_{\rm evts}}{N_{\Upsilon(1S)}\mathcal{B}(\Xi^{*0}(1530) \to \Xi^-\pi^+)\mathcal{B}(\Lambda^0 \to p\pi^-)\epsilon_{\rm acc}}. \quad (4.1)$$

Here $N_{\Upsilon(1S)} = (102 \pm 2) \times 10^6$ is the number of $\Upsilon(1S)$ decays in the data sample [44], $\mathcal{B}(\Xi^{*0}(1530) \to \Xi^-\pi^+) = 0.667$ (determined from Clebsch-Gordon coefficients), $\mathcal{B}(\Lambda^0 \to p\pi^-) = 0.639 \pm 0.005$ [29] and $\epsilon_{\rm acc}(\Xi^{*0}(1530)) = 0.065 \pm 0.005$ is the MC-determined acceptance. The resulting branching fraction is

$$\mathcal{B}(\Upsilon(1S) \to \bar{\Xi}^{*0}(1530)\ X) = (3.23 \pm 0.02\ (\text{stat}) \pm 0.26\ (\text{syst})) \times 10^{-3}, \quad (4.2)$$

where (for now) the systematic error is entirely due to the statistical error on the MC-determined acceptance. This is the first measurement of an inclusive strange particle branching fraction for the $\Upsilon(1S)$.

Figure 4.2(left) shows the MC-determined efficiency for the $\Xi^{*0}(1530)$ as a function of scaled momentum $x = p/p_{\max}$, where p is the three-momentum in CM frame and $p_{\max}$ is its maximum possible value. Figure 4.2(center) shows $d\mathcal{B}(\Upsilon(1S) \to \Xi^{*0}(1530)\, X)/dx$ for data and Fig. 4.2(right) shows the same distrbution for MC.

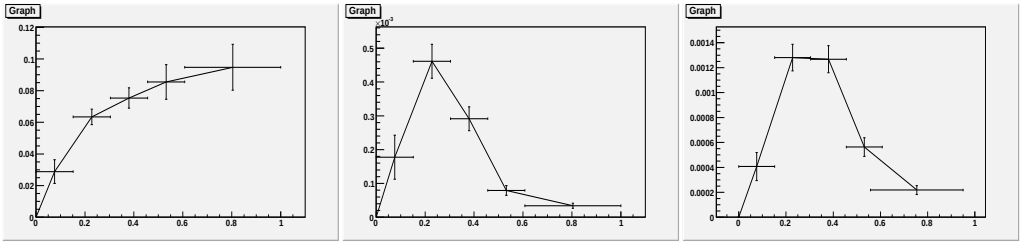

Figure 4.2: efficiency**(Left)**; MC data *Bf***(Middle)**; Real data *Bf***(Right)**.

4.1.2 $\mathcal{B}(\Upsilon(1S) \to \Xi_c^0(2470)\ X) \times \mathcal{B}(\Xi_c^0 \to \Xi^-\pi^+)$

Figure 4.3 shows the continuum-subtracted combined $M(\Xi^-\pi^+)$ and $M(\bar{\Xi}^+\pi^-)$ distributions in the 2470 MeV nass region as data points, and the results of a fit that uses a Gaussian function to represent the $\Xi_c^0(2470) \to \Xi^-\pi^+$ signal and a first-order polynomial to represent the backgound as a smooth curve. The signal yield from the fit is $N_{evts}(\Xi_c^0) + N_{evts}(\bar{\Xi}_c^0) = 612 \pm 59$ events.

We determine the product branching fraction from the relation

$$\mathcal{B}(\Upsilon(1S) \to \Xi_c^0\ X) \times \mathcal{B}(\Xi_c^0 \to \Xi^-\pi^+) = \frac{(N_{\rm evts}(\Xi_c^0) + N_{\rm evts}(\bar{\Xi}_c^0))/2}{N_{\Upsilon(1S)}\mathcal{B}(\Lambda^0 \to p\pi^-)\epsilon_{\rm acc}(\Xi_c^0)}, \quad (4.3)$$

where the efficiency $\epsilon_{\rm acc}(\Xi_c^0) = 0.137 \pm 0.005$ is determined from Monte Carlo. The result is

$$\mathcal{B}(\Upsilon(1S) \to \Xi_c^0(2470)\, X) \times \mathcal{B}(\Xi_c^0 \to \Xi^-\pi^+) = (3.42 \pm 0.34\,(\text{stat}) \pm 0.15\,(\text{syst})) \times 10^{-5}. \quad (4.4)$$

Here (also for now) the systematic error is due to statistics on the MC-determined acceptance. The combined Ξ_c^0 and $\bar{\Xi}_c^0$ signal has about a 10σ

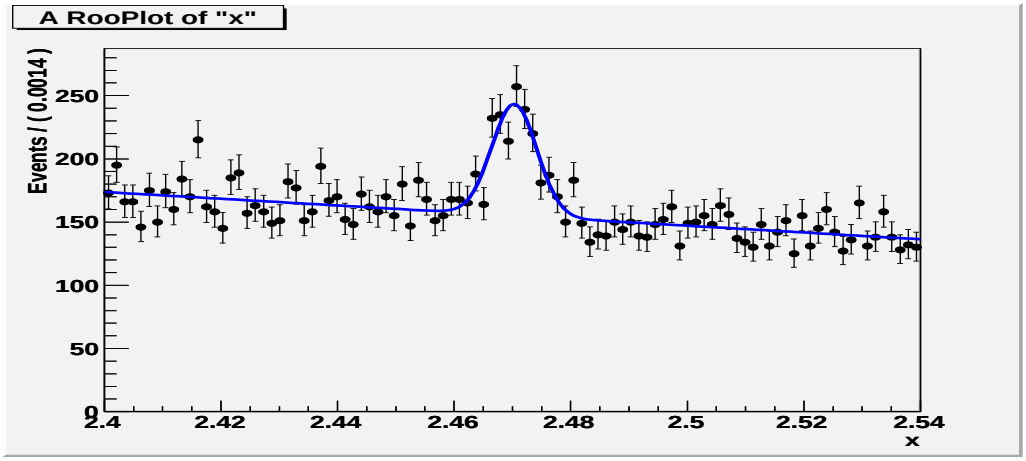

Figure 4.3: The data points show the continuum-subtracted combined $M(\Xi^-\pi^+)$ and $M(\bar{\Xi}^+\pi^-)$ distributions in the $\Xi_c^0(2470)$ region; the smooth curve shows the results of the fit described in the text.

statistical significance and the inclusive branching fraction for Ξ_c^0 production is comparable with that for antideuterons $(2.86 \pm 0.28)\times 10^{-5}$. This indicates that we have the desired sensitivity for an Ξ_5^{--} search in the $\Xi^-\pi^-$ decay channel.

4.1.3 $\mathcal{B}(\Upsilon(2S) \to \overline{\Xi^{*0}}(1530)\ X)$

By applying the same selection technique to the $\Upsilon(2S)$ data sample, we determine the continuum-subtracted $\bar{\Xi}^+\pi^-$ invariant mass distribution in the $\bar{\Xi}^{*0}(1530)$ mass region shown in the Fig. 4.4. Here the smooth curve shows the results from the application of the same fitting technique that we used for the $\Upsilon(1S)$ data sample, which gives a $\bar{\Xi}^{*0}(1530)$ signal yield of 19780 ± 270 events. From this, we use Eq. 4.1 to determine the branching fraction $\mathcal{B}(\Upsilon(2S) \to \bar{\Xi}^{*0}(1530)\ X)$ to be

$$\mathcal{B}(\Upsilon(2S) \to \bar{\Xi}^{*0}(1530)\ X) = (4.52 \pm 0.06\ (\text{stat}) \pm 0.35\ (\text{syst})) \times 10^{-3}. \quad (4.5)$$

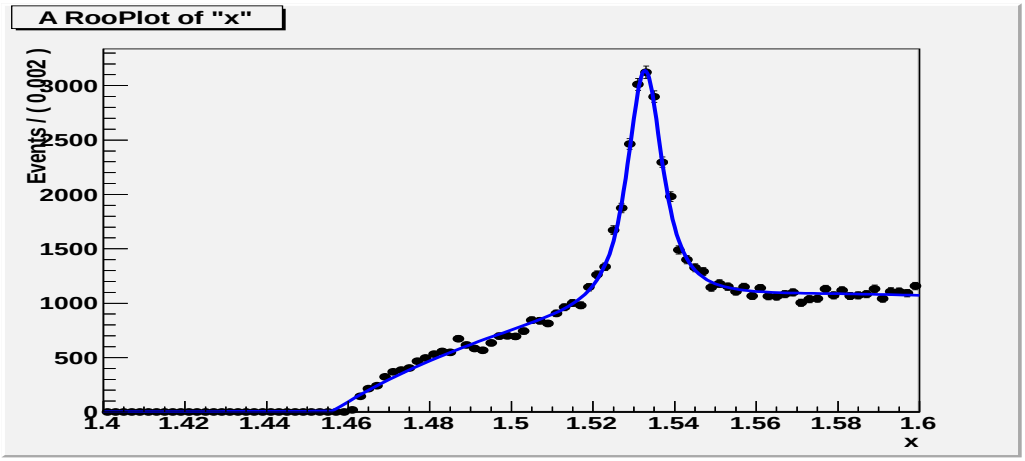

Figure 4.4: The $M(\bar{\Xi}^+\pi^-)$ invariant mass distribution for the $\Upsilon(2S)$ data sample in the near-threshold region.

4.1.4 $\mathcal{B}(\Upsilon(2S) \to \Xi_c^0(2470)\ X) \times \mathcal{B}(\Xi_c^0 \to \Xi^-\pi^+)$

Fig. 4.5 shows the combined $\Xi^-\pi^+$ and $\bar{\Xi}^+\pi^-$ invariant mass distribution for the $\Upsilon(2S)$ data sample in the region of the $\Xi_c^0(2470)$. The fit results, shown as a smooth curve in the figure, indicate a combined signal yield of 1296 ± 104 events. Using Eq. 4.3, we determine the inclusive branching fractin branching fraction $\mathcal{B}(\Upsilon(2S) \to \Xi_c^0(2470)\ X)$ to be

$$\mathcal{B}(\Upsilon(2S) \to \bar{\Xi}_c^0(2470)\ X) = (5.13 \pm 0.41\ (\text{stat}) \pm 0.16\ (\text{syst})) \times 10^{-5}. \quad (4.6)$$

In here, branching fraction ratio between $\Upsilon(2S)$ sample divide $\Upsilon(1S)$ sample of $\Xi_c^0(2470)$ is bigger than $\bar{\Xi}^{*0}(1530)$. It mean more charm quark pairs are generated in $\Upsilon(2S)$ decay.

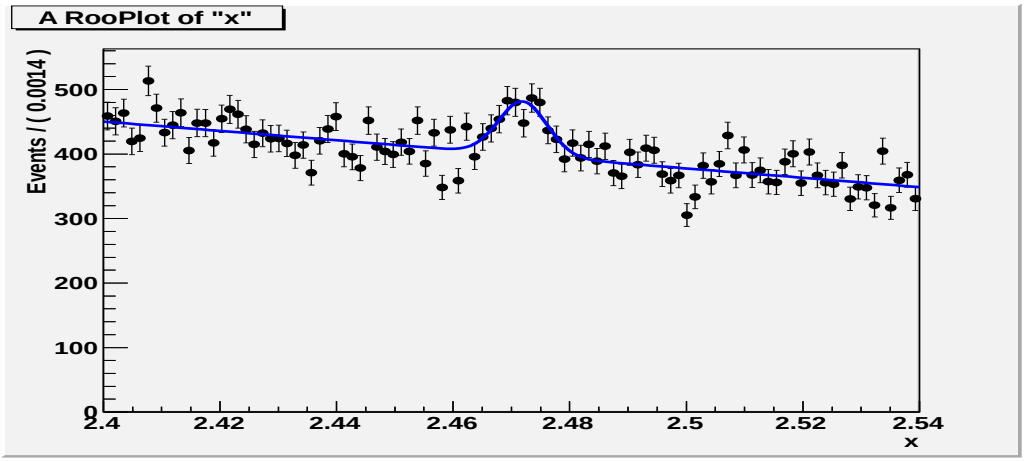

Figure 4.5: The combined $\Xi^-\pi^+$ and $\bar{\Xi}^+\pi^-$ invariant mass distributions for the $\Upsilon(2S)$ data sample in the vicinity of the $\Xi_c^0(2470)$. The smooth curves show the results of the fits described in the text.

4.2 Searching the Ξ_5 pentaquark

4.2.1 Opening the Ξ_5 blind box

After getting agreement from Belle referees, we examined the blinded $M(\Xi^-\pi^-)$ and $M(\Xi^-\pi^+)$ mass regions with anti channel. Figure 4.6 show the continuum-subtracted $\Xi^-\pi$ mass distributions. In the combined $\Xi^-\pi^+$ & $\bar{\Xi}^+\pi^-$ mass distribution for the $\Upsilon(1S)$ data sample, shown in the top left panel of Fig.4.6, no narrow structures other than the $\Xi^{*0}(1530)$ and $\Xi_c^0(2470)$ are evident. The combined $\Xi^-\pi^-$ & $\bar{\Xi}^+\pi^+$ mass distribution, shown in the top right panel of Fig.4.6, is featureless. The corresponding plots for the mass $\Upsilon(2S)$ data sample, shown in the middle row of Fig. 4.6 and the sum of the $\Upsilon(1S)$ and $\Upsilon(2S)$ data sample in the low row, have similar characteristics.

4.2.2 Upper Limits for $\mathcal{B}(\Upsilon(1,2S) \rightarrow \Xi_5\ X) \times \mathcal{B}(\Xi_5 \rightarrow \Xi^-(\pi^-\ (\pi^+))$

We search for signs of Ξ_5 signals by making fits to the $\Xi^-\pi^+$ plus $\bar{\Xi}^+\pi^-$ (Fig. 4.7 **(left)**) and $\Xi^-\pi^-$ plus $\bar{\Xi}^+\pi^+$ (Fig. 4.7 **(left)**) invariant mass distributions using a Voigtian function to represent the signal and a reversed ARGUS function modulated by a fourth-order polynomial the combinatorial background, where the signal peak position is confined to a 10 MeV window that is scanned in 10 MeV steps from 1.685 GeV to 1.995 GeV. The fits are done with fixed BW widths of $\Gamma = 0,\ 10$ and 20 MeV. The resulting signal yields for each mass bin, $N_{evts}(\Xi_5^0) + N_{evts}(\bar{\Xi}_5^0)$, are shown for the Ξ_5^0 scan in the top row of Fig. 4.8; there is only point more than 2.5σ from zero. The corresponding results from the Ξ_5^{--} scan are shown in Fig. 4.9. 1723,1 82

In the absence of any significant signal, we determine upper limits on

$\mathcal{B}(\Upsilon(1,2S) \to \Xi_5\ X) \times \mathcal{B}(\Xi_5 \to \Xi^-\pi))$ using the relation

$$\mathcal{B}(\Upsilon(1,2S) \to \Xi_5\ X) \times \mathcal{B}(\Xi_5 \to \Xi^-\pi)) = \frac{[N^{\rm UL}_{\rm evts}(\Xi_5 + \bar{\Xi}_5)]/2}{N_{\Upsilon(1,2S)}\mathcal{B}(\Lambda \to p\pi^-)\epsilon_{\rm acc}(\Xi_5)(1-\sigma_{\rm syst})}. \tag{4.7}$$

For the Ξ_5 efficiency (ϵ_{acc}) for each mass region, we use a linear interpolation between the $\Xi^0(1530)$ and $\Xi_c(2470)$ values. The resulting branching fraction upper limit values for $\Xi^0_5\,X$ for the the three different values of Γ are shown in the bottom rows of Figs. 4.8; those for $\Xi^{--}\,X$ are shown in the bottom panels of Fig. 4.9. The maximum upper limit for each Γ value is listed in Table 4.1; for the narrow width, an upper limit comparable to the $\mathcal{B}(\Upsilon(1S) \to \bar{d}\,X)$ value is established.

Table 4.1: Ξ_5 upper limit value.

Width	$\Xi^0_5\ + (\bar{\Xi}^0_5)$	$\Xi^{--}_5\ + (\bar{\Xi}^{--}_5)$
$\mathcal{B}[\Upsilon(1,2S) \to \Xi_5\ X]\mathcal{B}[\Xi_5 \to \Xi^-\pi]$ (90% confidence level)		
$\Gamma = 1MeV$	$\leq\ 2.5 \times 10^{-5}$	$\leq\ 2.8 \times 10^{-5}$
$\Gamma = 10MeV$	$\leq\ 3.8 \times 10^{-5}$	$\leq\ 5.0 \times 10^{-5}$
$\Gamma = 20MeV$	$\leq\ 4.9 \times 10^{-5}$	$\leq\ 6.8 \times 10^{-5}$

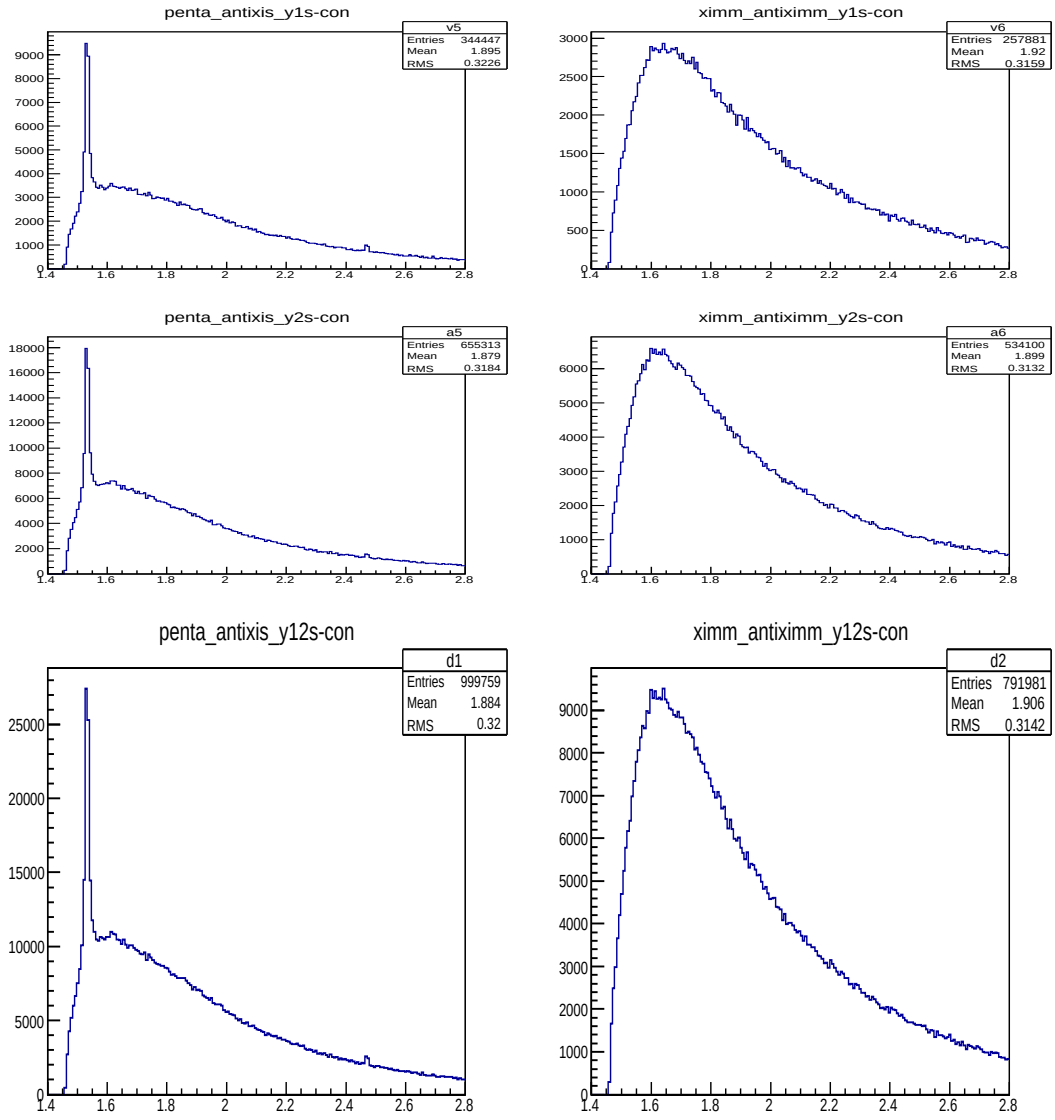

Figure 4.6: **Upper:** The combined $\Xi^-\pi^+$ & $\bar{\Xi}^+\pi^-$ (left) and $\Xi^-\pi^-$ & $\bar{\Xi}^+\pi^+$ (right) invariant mass distributions for the $\Upsilon(1S)$ data sample. **Middle:** The corresponding distributions for the $\Upsilon(2S)$ data. **Lower:** The sum of the $\Upsilon(1S)$ and $\Upsilon(2S)$ distributions.

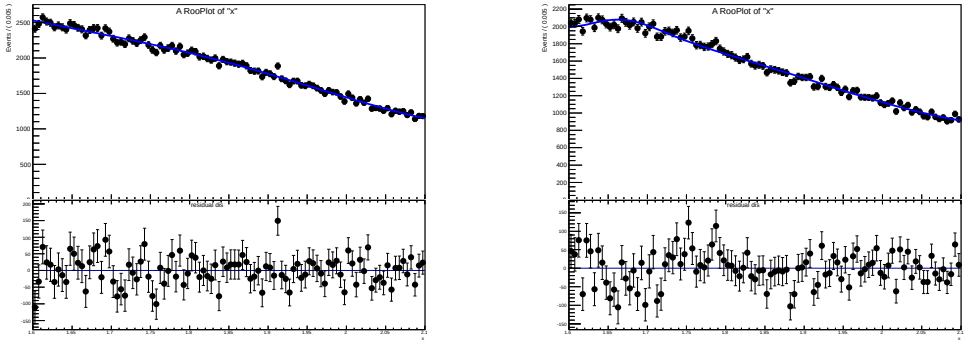

Figure 4.7: **Top:** Combined $M(\Xi^-\pi^+)$ & $M(\bar{\Xi}^+\pi^-)$ (left) and $M(\Xi^-\pi^-)$ & $M(\bar{\Xi}^+\pi^+)$ (right) distributions for the combined $\Upsilon(1S)$ and $\Upsilon(2S)$ data samples. The blue curve in each figure shows the result of a fit to the distribution using a reversed ARGUS function modulated by a fourth-order polynomial. **Bottom:** The fit residuals.

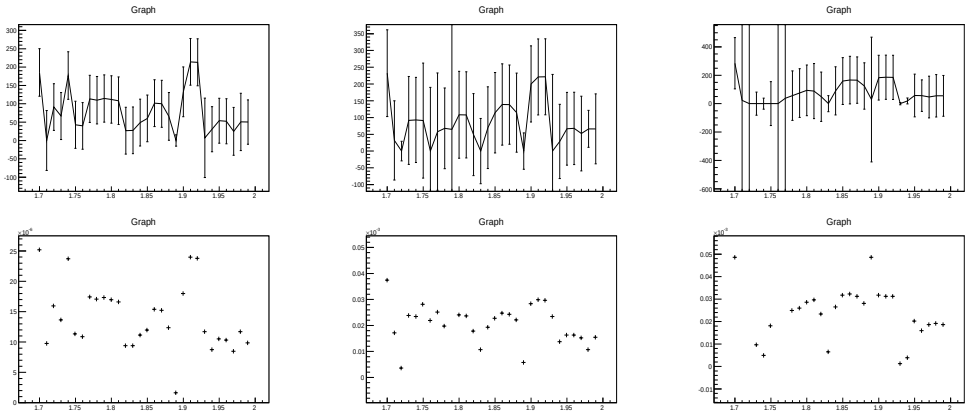

Figure 4.8: **Top:** The $\Xi_5^0 \to \Xi^-\pi^+$ signal yields from the fits described in the text for $\Gamma = 1$ MeV (left), $\Gamma = 10$ MeV(center) and $\Gamma = 20$ MeV (right). **Bottom:** The 90% CL upper limits on the $\mathcal{B}(\Upsilon(1,2S) \to \Xi_5^0 X) \times \mathcal{B}(\Xi_5^0 \to \Xi^-\pi^+)$ product branching fractions versus mass for $\Gamma = 0$ MeV (left), $\Gamma = 10$ MeV(center) and $\Gamma = 20$ MeV (right).

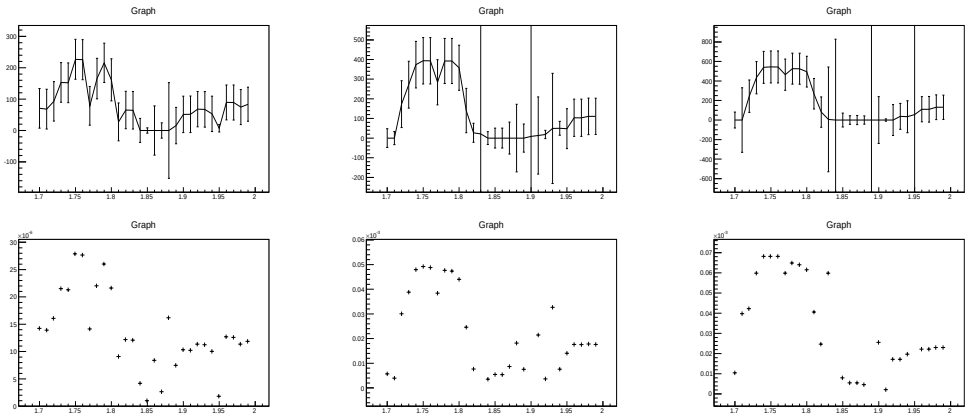

Figure 4.9: **Top:** The $\Xi_5^{--} \to \Xi^-\pi^-$ signal yields from the fits described in the text for $\Gamma = 1$ MeV (left), $\Gamma = 10$ MeV(center) and $\Gamma = 20$ MeV (right). **Bottom:** The 90% CL upper limits on the $\mathcal{B}(\Upsilon(1,2S) \to \Xi_5^{--} X) \times \mathcal{B}(\Xi_5^{--} \to \Xi^-\pi^-)$ product branching fractions versus mass for $\Gamma = 0$ MeV (left), $\Gamma = 10$ MeV(center) and $\Gamma = 20$ MeV (right).

4.3 Search for $\Upsilon(1,2S) \to H\ X$

4.3.1 Blind box open for $\Upsilon(1,2S) \to H\ X; H \to \Xi^- p$

Because we opened the blind box of penta-quark in $\Xi^-\pi^\pm$ mass distribution, we can get permission easily from refrees after adding few cut creteria for proton optimization and expected backgroud rejection. Fig. 4.10 shows $M(\Xi^- p)$ distribution adding $\Upsilon(1S)$ and $\Upsilon(2S)$ sample and subtracting continuum-background. Bin size is 1 MeV and distributed mass region cover below $2m_\Sigma$. there's no signal or hint of H-dibaryon. Fitting and upperlimit study of this channel will be explained later.

4.3.2 Search for $\Upsilon(1,2S) \to H\ X; H \to \Lambda\Lambda$

As followed before subsection, we couldn't find any hint of H-dibaryon. After studying MC samples and real data in above $m_{\Xi^-} + m_p$ mass threshold, we got agreement from refrees and opened the blind box. Fig. 4.11 shows mass distribution after box opening. Upper panel shows $M(\Lambda\Lambda)$ and $M(\overline{\Lambda\Lambda})$ added distribution for surviving events from $\Upsilon(1S)$ sample. Except fluctuation by statistical uncertainty, there's no bump or signal-like feature. middle (low) panel shows same distribution from $\Upsilon(2S)$ ($\Upsilon(1S,\ 2S)$) data samples and also we can see distribution without bump or hint of H-dibaryon. Histogram looks more fluctuate in $m \simeq 2.26GeV$ because this region is $m_{\Xi^-} + m_p$ which can be affect to phase-space distribution.

Fitted results of the $M(\Lambda\Lambda)$ ($M(\bar{\Lambda}\bar{\Lambda})$) distribution for surviving events is shown in the upper (lower) panel of Fig. 4.12, where there is no evident signal for $H \to \Lambda\Lambda$ ($\bar{H} \to \bar{\Lambda}\bar{\Lambda}$). In here, we only fit mass below $m_{\Xi^-} + m_p$ and x-axis value is $\Delta M = M(\Lambda\Lambda) - 2m_\Lambda(MeV)$. The curve is the result of a background-only fit using an ARGUS-style function. TThe dashed curve in the figure shows the expected H-dibaryon signal for a $\Upsilon(1S,2S) \to HX$ branching fraction that is $1/20^{th}$ that for anti-deuterons. The fit residuals

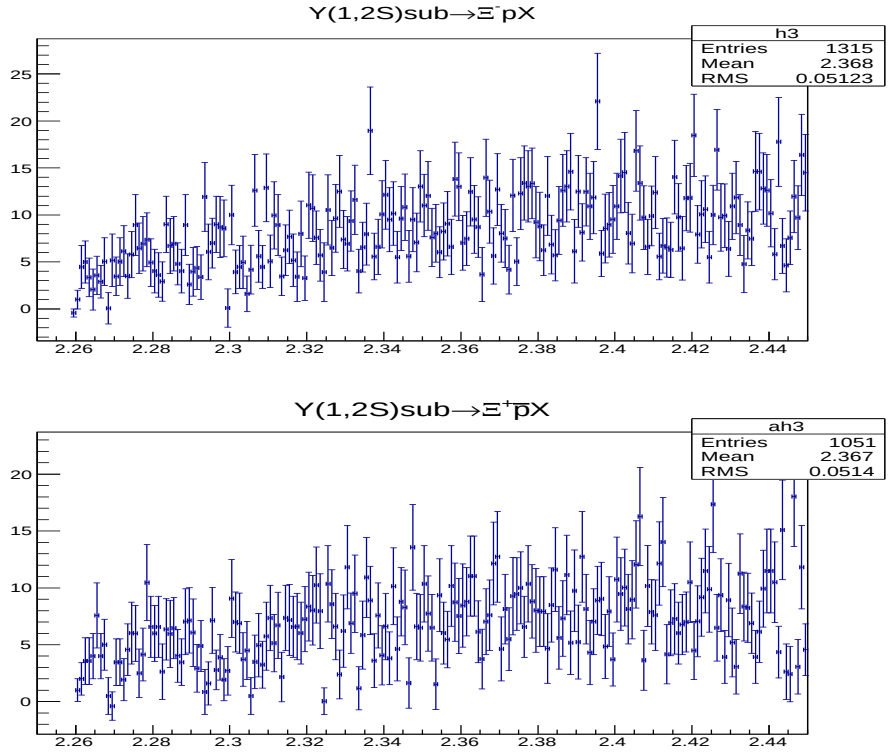

Figure 4.10: $M(\Xi^- p)$ distribution **(left)** and $M(\bar{\Xi}^+ \bar{p})$ **(right)** adding $\Upsilon(1S)$ and $\Upsilon(2S)$ sample and subtracting continuum-background.

are shown in the lower part of the panel. You can clearly see there's no bump and fluctuation also small than signal MC.

Upperlimit on $\mathcal{B}(\Upsilon(1,2S) \to H\ X) \times \mathcal{B}(H \to \Lambda\Lambda)$

As you can see continuum distribution fo $\Xi^-\pi^+$ channel, there's some contribution from continuum data to signal. For seeing perfect continuum subtracted distribution, we don't want to just use continuum expected PDF for estimating background fitting. Because of this fact, we subtract histogram which means we need to use binnned histogram for fitting. We need to

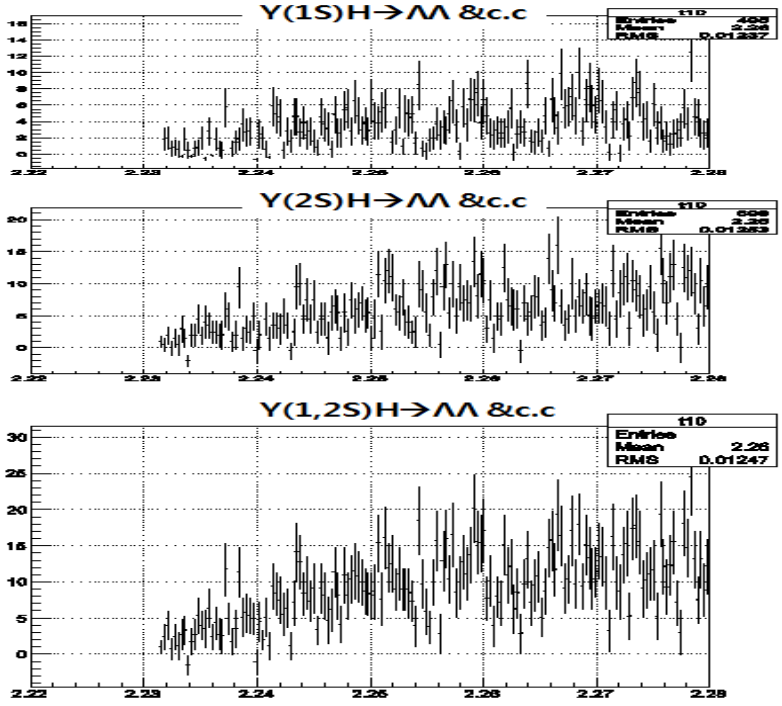

Figure 4.11: $M(\Lambda\Lambda)$ and $M(\overline{\Lambda\Lambda})$ added distribution for surviving events from $\Upsilon(1S)$ sample **(upper)**, from $\Upsilon(2S)$ sample **(middle)** and from $\Upsilon(1S, 2S)$ both sample.

choose bin size for fitting which should be smaller than resolution for non-width signal PDF(gaussian function). Signal PDF What we actually use is Gaussian-broadened BW function [49] because of strong decay width. Although Fig. 4.12 shows 1MeV bin histogram for showing, we used 0.25MeV for fitting because of 0.3MeV and 0.5MeV resolution for H and $\bar{H}$ signal with width $\Gamma = 0$. For fitting H and $\bar{H}$ signal with $\Gamma = 10MeV$, we used 0.5MeV bin histogram. Because we can't expect exact H-dibaryon mass and we counldn't find any bump in data, we need to get upperlimit for all mass if possible. But it need to many work and it would be enough getting up-

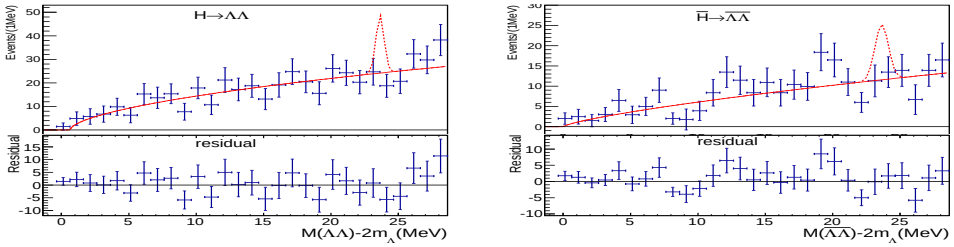

Figure 4.12: The upper panel shows the $M(\Lambda\Lambda)$ distribution and fit residuals for the combined $\Upsilon(1S)$ and $\Upsilon(2S)$ data samples with the background-only fit superimposed. The lower panel shows the same distributions for $M(\bar{\Lambda}\bar{\Lambda})$.

perlimit for each mass region. We divide mass region by 4MeV window and singla peak position in confined in this window. So totally 7 window is in $\Lambda\Lambda$ channel. For each window, we can fit gaussian function with floating mass and height parameter. By changing height we can get χ^2 distribution for each height. The area of gaussian is number of signal and we can get branching fraction from this. So we can get χ^2 distribution for branching fraction. This distribution can be change to likelihood distribution by Eq. 4.8 which need to get upperlimit.

$$\mathcal{L} = exp(-\Delta\chi^2/2) \tag{4.8}$$

This gaussian likelihood distribution have statistical error inside. When we got likelihood distribution by changing height of gaussian, For adding systematic error in this distribution, we convolute this distribution with gaussian distribution which has width as systematic error value. Systematic error of $\Lambda\Lambda(\overline{\Lambda\Lambda})$ channel is $\sigma_{\Lambda\Lambda} = 14.7(19.8)\%$. Because we got systematic error as fraction of final value width is depend on branching fraction. By convolute these function, we can get green or red graph in Fig. 4.13.

In this graph, red graph is likelihood distribution of $\Lambda\Lambda$ channel, green graph is likelihood distribution of $\overline{\Lambda\Lambda}$ channel and black graph is convoluted graph of red and green. The reason of (-) value in x-axis is gaussian signal

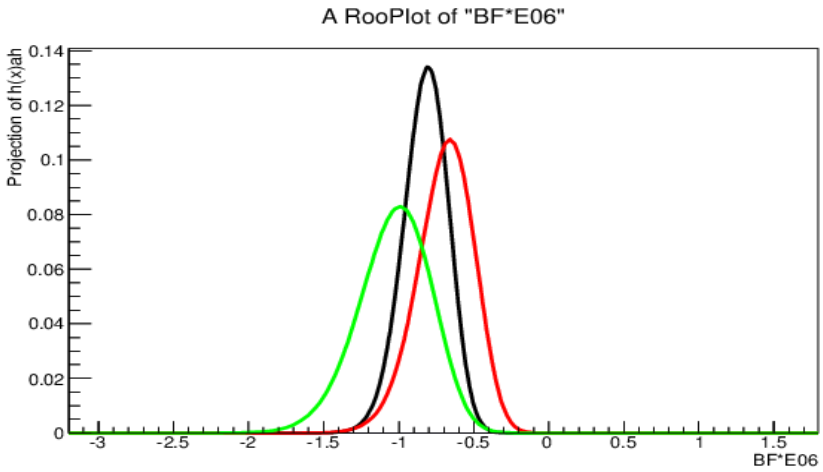

Figure 4.13: likelihood distribution of $\Lambda\Lambda$ channel(Red line), $\overline{\Lambda\Lambda}$ channel(Green line) and convoluted distribution(Black line)

PDF can be negative if best fitted height is negative. From the Eq. 4.9

$$\mathcal{B}(\Upsilon(1S,2S) \to H\ X) \cdot \mathcal{B}(H \to \Lambda\Lambda) < \frac{N^{UL}(\mathrm{M_H})}{2N_{\Upsilon(1S,2S)} 2\mathcal{B}(\Lambda \to p\pi)\epsilon_{\mathrm{T}}}, \qquad (4.9)$$

Wherer $N_{\Upsilon(1S,2S)} = (260\ \pm\ 6) \times 10^6$ is the total number of $\Upsilon(1S)$ and $\Upsilon(2S)$ events in the data sample, two branching fraction divided ($2\mathcal{B}(\Lambda \to p\pi)$) for two Λ and other division 2 is for anti-particle. So eventually we got black likelihood graph and we need to get 90% CL upperlimit from this graph. For the limits, we use the branching fraction value that contains $< 90\%$ of the above-zero area of the product of the H and $\bar{H}$ likelihood functions. Result will be shown with $\Lambda p\pi$ channel in Fig. 4.16.

4.3.3 Search for $\Upsilon(1,2S) \to H\ X; H \to \Lambda p\pi$

After the agreement from refrees, we opened the blind box of $\Lambda p\pi$ channel.

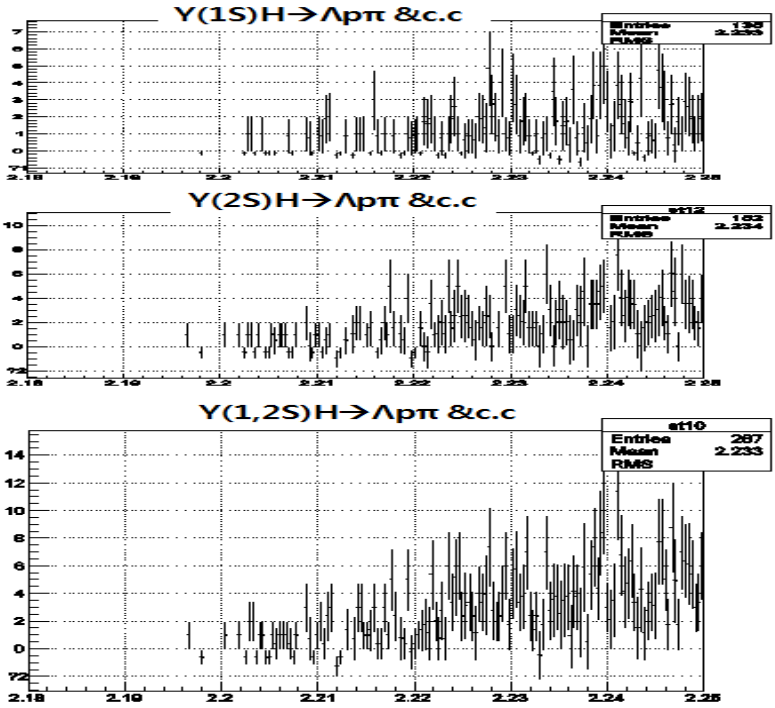

Figure 4.14: $M(\Lambda p\pi^-)$ and $M(\overline{\Lambda}\bar{p}\pi^+)$ added distribution for surviving events from $\Upsilon(1S)$ sample **(upper)**, from $\Upsilon(2S)$ sample **(middle)** and from $\Upsilon(1S, 2S)$ both sample.

Upper panel of Fig. 4.14 shows $M(\Lambda p\pi)$ distribution using $\Upsilon(1S)$ sample data without blindbox. You can see there's only few events in threshold region and gradually increase without bump or hint. Because we subtract continuum background in here, you can see some negative bins. Error in histogram estimated $\sqrt{N_\Upsilon + N_{cont}}$, you can check in histogram. Middle panel shows $M(\Lambda p\pi)$ distribution using $\Upsilon(2S)$ and lower panel is just added histogram of $\Upsilon(1S)$ & $\Upsilon(2S)$ data sample. Region we need to care is below $2m_\Lambda = 2.231$. Fitted result of the $M(\Lambda p\pi^-)$ ($M(\overline{\Lambda}\bar{p}\pi^+)$) distribution of

surviving events is shown in the upper(lower) panel of fig. 4.15

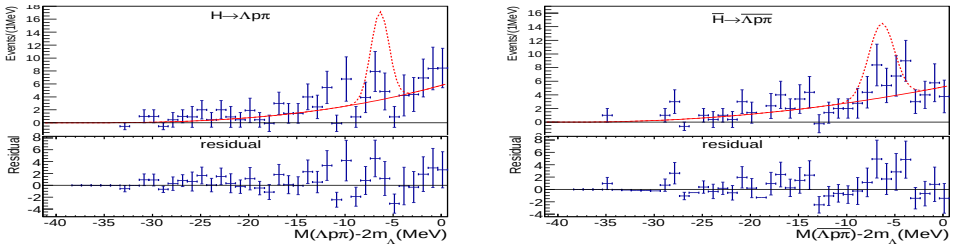

Figure 4.15: The upper panel shows the $M(\Lambda p\pi^-)$ distribution and fit residuals for the combined $\Upsilon(1S)$ and $\Upsilon(2S)$ data samples with the background-only fit superimposed. The lower panel shows the same distributions for $M(\bar{\Lambda}\bar{p}\pi^+)$.

In these histogram, x-axis is $\Delta M = M(\Lambda p\pi^-) - 2m_\Lambda(MeV)$ so fitted region has negative x values. Cross points are $\Upsilon(1S,2S)$ data which continuum subtracted and red line is background fitting using ARGUS-like function and dashed line shows expected H signal gaussian function for a $\Upsilon(1S,2S) \to HX$ branching fraction that is $1/20^{th}$ that for anti-deuterons. Lower histogram is residual distribution and you can see no signal or hint and only small fluctuation exist. Left panel is $\Lambda p\pi^-$ channel and right panel is $\bar{\Lambda}\bar{p}\pi^+$.

Upperlimit on $\mathcal{B}(\Upsilon(1,2S) \to H\ X) \times \mathcal{B}(H \to \Lambda p\pi^-)$

With same strategy of H-dibaryon upperlimit estimation of $\Lambda\Lambda$ channel, we select bin size as 0.5MeV which is enough compare with $H \to \Lambda p\pi^-(\bar{H} \to \bar{\Lambda}\bar{p}\pi^+)$ signalMC resolution value 0.94 MeV(1.34 MeV). We divide mass distribution for each 4 MeV window same as $\Lambda\Lambda$ channel and fitting with gaussian mean is inside this window with floated height and mean value. But for first two window which have only few events in window, we couldn't χ^2 fit well because of shortage of events. We estimate all events in this two bin as

possible signal and draw likelihood distribution with $\sqrt{N}$ error value. For third window, we also don't have enough events in $\bar{H} \to \bar{\Lambda}\bar{p}\pi^+$ channel and enough data to fit in $H \to \Lambda p\pi^-$ channel. So we got likelihood distribution using χ^2 fit result in $H \to \Lambda p\pi^-$ channel and convolute this with gaussian distribution by counting number of $\bar{H} \to \bar{\Lambda}\bar{p}\pi^+$ channel events with $\sqrt{N}$ error value. Of course after convolute each systematic error likelihood for each channel. For $\Lambda p\pi$ channel, we have 9 window and got 90% CL upperlimit branching fraction by calculate integraled area above zero be 90% for total area above zero. In Fig. 4.16 shows 90% confidence level upperlimit with bar for each windows of $\Lambda p\pi$ and $\Lambda\Lambda$ channel. I also draw 1-sigma and 2-sigma values of braching fraction. This values are 1,2 sigma from best fitted value and can be negative. Because of this some 1,2 sigma value didn't shows in figure. Compare with average PDG value fo $\mathcal{B}(\Upsilon(1S,2S)) \to \bar{d}X)$, we have stringent upperlimit more than 10 times smaller.

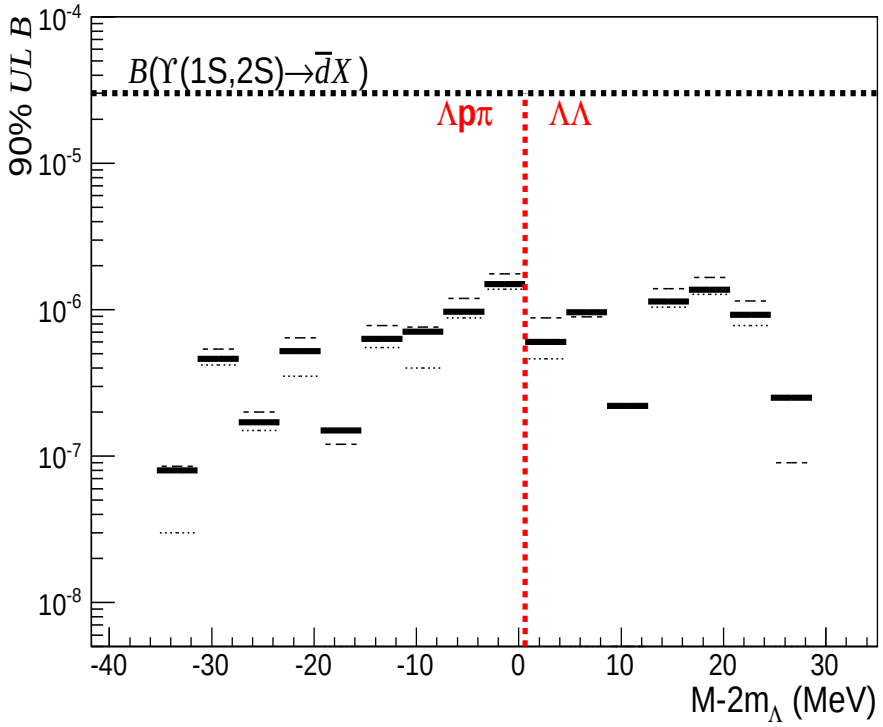

Figure 4.16: Upper limits (at 90% CL) for $\mathcal{B}(\Upsilon(1S,2S) \to HX) \cdot \mathcal{B}(H \to f_i)$ for a norrow ($\Gamma = 0$) H-dibaryon *vs.* $M_H - 2m_\Lambda$ are shown as solid horizontal bars. The one(two) sigma values are shown as the dotted (dashed) bars. (For some mass bins, there are negative and not shown.) The vertical dotted line indicates the $M_H = 2m_\Lambda$ threshold. The limits below(above) the $2m_\Lambda$ threshold are for $f_1 = \Lambda p\pi^-(f_2 = \Lambda\Lambda)$. The horizontal dotted line indicates the average PDG value fo $\mathcal{B}(\Upsilon(1S,2S)) \to \bar{d}X)$.

4.3.4 Search for $\Upsilon(1,2S) \to H\ X; H \to \Xi^- p$

Fig. 4.10 is $M(\Xi^- p)$ distribution of $\Upsilon(1S, 2S)$ data after continuum background subtracted. In $H \to \Lambda\Lambda$ and $H \to \Lambda p\pi$ channel, We used binned histogram for fitting by binned χ^2 (least squre method) fitting. But this method is not good for wide mass range fitting which has many bins and small data sample. Because of this problem, we use unbinned likelihood fitting with expected continuum PDF. Main reason we use continuum subtraction using continuum data itself is because of $\Xi^{*0}(1530)$ and $\Xi_c^0(2470)$ peak in continuum data. We can't perfectly understand continuum background make some bump or distributionm, we prefer to use data before. But in this channel, fitting completeness is more important, so we use Argus BG distribution for continuum data expectation. Totally three Argus function is used for one background fuction and resolution-broadened Breit-Wigner function, a so-called Voigtian [49], used to represent the signal. Fig. 4.17 shows fitted distribution of $M(\Xi^- p)$ **(left)** and $M(\bar{\Xi}^+ \bar{p})$ **(right)** with fitted function (Blue line). Each histogram have two red line which is expecd continuum background from $\Upsilon(1S)$ and $\Upsilon(2S)$ data.

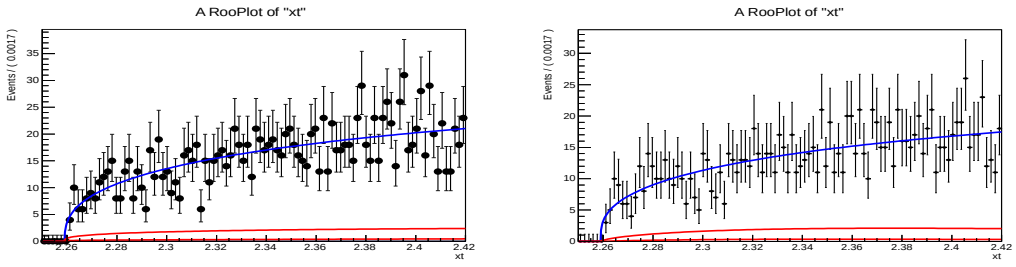

Figure 4.17: fitted distribution of $M(\Xi^- p)$ **(left)** and $M(\bar{X}i^+ \bar{p})$ **(right)** with fitted function (Blue line) and expected continuum background function(red).

After getting upperlimit of $\Xi^- p$ decay channel for each 4MeV mass bins, we draw $90\%CL$ upperlimit distribution like before. Fig. 4.18 shows $90\%CL$

upperlimit distribution for all channel with upper horizontal dashed-dotted line indicates the averaged PDG value for $B(\Upsilon(1S,2S) \to \bar{d}X)$. With stable upperlimit from $\Xi^- p$ decay channel, we can stringently banned above $1/10^{th}$ branching fraction of H-dibaryon above $m_\Lambda + m_p + m_\pi$ with assumption of $B(H \to f_i) = 1$.

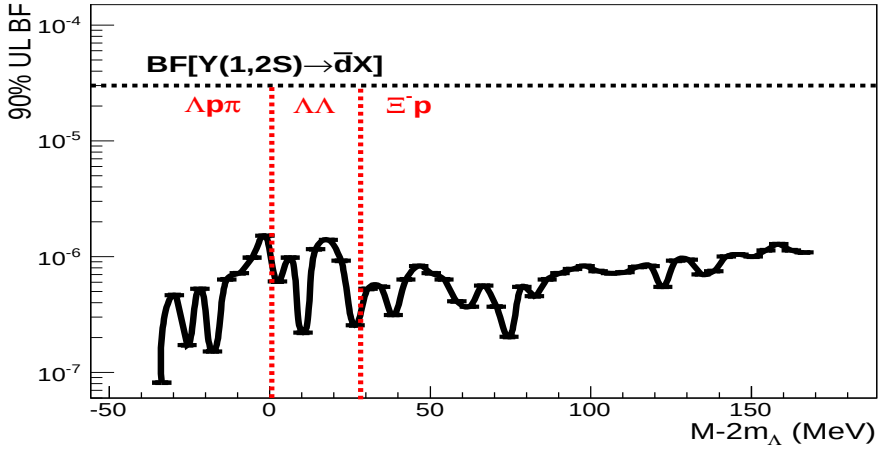

Figure 4.18: Upper limits (at 90% CL) for $B(\Upsilon((1S,2S) \to\ H\ X) \cdot B(H \to f_i)$ for a norrow ($\Gamma = 0$) H-dibaryon *versus.* M_H. The vertical dashed line indicates the mass thresholds of $\Lambda\Lambda$ and $\Xi^- p$. Left 9 bars are for $f_i = \Lambda p\pi$, middle 7bars are for $f_i = \Lambda\Lambda$ and right bars are for $f_i = \Xi^- p$ channel. The horizontal dashed-dotted line indicates the averaged PDG value for $B(\Upsilon(1S,2S) \to \bar{d}X)$

Chapter 5

systematic uncertainties

As mentioned before we use caseA data samples for penta-quark, Ξ resonance study and $\Upsilon(1S) \rightarrow HX$ with $H \rightarrow \Xi^- p$ channel study and caseB data samples for other H-dibaryon search. Because we couldn't share estimated systematic errors between channels, We need to get systematic error for each channels but way to get is same for same cut values.

When we care about systematic error it is better to see again branching fraction formula Eq. 4.3. We can see systematic error will come from $*$ signal number estimation, $*$ generated number estimation and $*$ signal efficiency. Most systamatic errors come from signal efficiency by selection requirements.

Signal number estimation means that fitting change by mass region and bin size will give different result. Because we use fitting way for window which have enough events so this error will be small. For estimate this error, we study with changing bin size, fit-range and signal resolution. Because we couldn't find any bump, we fix signal resolution as signal MC resolution with correction factor estimated by Ξ^- and $\Xi_c^0(2470)$ resonance.

Generated number error is come from $\sigma(N_\Upsilon)$ number of $\Upsilon(1S, 2S)$ error and $\sigma(\mathcal{B}(\Lambda \rightarrow p\pi))$ branching fraction error. Both errors are estimated by other peoples and just using these error values would be okay. As mentioned

in Sec. 3.1.1, BELLE colleague studied N_Υ. By Chen,.et.at [44], measured $\Upsilon(1S)$ number is (102±2)M and $\Upsilon(2S)$ number is (157.8±3.6)M. Fraction value is $\sigma(N_{\Upsilon(1S)}) = 2.3\%$ and $\sigma(N_{\Upsilon(1S)}) = 3.6\%$ When we use total number of $\Upsilon(1S)$ and $\Upsilon(2S)$ both from the $N_\Upsilon = 260 \pm 6$, systematic error fraction is $\sigma(N_\Upsilon) = 2.3\%$. $\sigma(\mathcal{B}(\Lambda \to p\pi)) = 0.8\%$ is found in PDG. So $\Lambda\Lambda$ channel have 1.6% by two Λ candidate. Because we subtract continuum background data using off-resonance data samples near $\Upsilon(4S)$ mass region. Even though excluding lost luminosity, enough off-resonance data sample make statistical effect be small. From the Belle collaboration study, we have 1.4% systematic error on aacuracy when estimate luminosity by Bhabha events of data sample. So we can use this systematic error as defalt.

Other systematic errors come from signal efficiency $\sigma(\epsilon)$. All detector performance accompany systematic error. The parameters what we use this analysis in all BELLE detector parameters are tracking and particle Identification. With this two detection efficiency, all cut requirements will give efficiency so efficiency is $\epsilon_T = \epsilon_{track} \cdot \epsilon_{PID} \cdot \epsilon_{cuts}$ and we need to estimate error from this formula. Tracking efficiency's systematic error is studied BELLE collaborator using some channels and tracking error was estimated as 0.35(1.0)% for each track. All study in here use 4 tracks, so $\sigma(\epsilon_{tracking}) = 1.4(4.0)\%$.

All detailed study will be explained in each section of channel.

5.1 Systematic error study for $H \to \Lambda p\pi^- and H \to \Lambda\Lambda$ channel

Upper paragraphs deal with systematic errors which already studied by others and can just be used. But other systematic errors by cut parameters and fitting need to be estimated by myself. For studying particle Identification of proton and π, we can use information which already studied before about momentum dependent systematic error for proton and π. For proton selec-

tion $\mathcal{R}(p|h^+) \geq 0.1$, we can use 2.15% obtained from the difference of the maximum and minimum value of $\epsilon(data)/\epsilon(MC)$ over momentum. proton selection $\mathcal{R}(p|h^+) \geq 0.9$'s systematic error is 4.43%. Eventually $\Lambda\Lambda$ sample with 2 proton PID cut have 4.3% systematic error and $\Lambda p\pi$ channel have 6.58% systematic error from one 0.1 PID cut and the other 0.9 cut. Differ with $\Lambda\Lambda$ channel, $\Lambda p\pi$ channel also have π particle ID cut compare with K. This π selection have systematic error 2.78%.

The Λ selection creteria already studied well as V0-particle selection. So we can use information which give systematic error for 3 different momentum obtained from the difference of the maximum and minimum value of $\epsilon(data)/\epsilon(MC)$ over momentum. By applying this to data sample, we get systematic error of Λ reconstruction, GoodVee selection and $M(\Lambda)$ cut. You can check all systematic errors with this in Table. 5.1. The Λ selection systematic error of $\Lambda\Lambda$ is larger that $\Lambda p\pi^-$. Large systematic error come from low momentum Λ sample and momenumtum cut in $\Lambda p\pi^-$ sample reduce this large systematic error sample. We can also explain reason that systematic error of $\bar{\Lambda}\bar{p}\pi^+$ sample is higher than $\Lambda p\pi^-$ sample differ with $\Lambda\Lambda$ channel.

For studying systematic error by cut of χ^2 from vertex fitting and $c\tau$, we used $\Lambda\bar{\Lambda}$ data sample. In the absence of H and $\bar{H}$ signals in either the $\Lambda p\pi^-$ and $\Lambda\Lambda$ decay channels, We study how the data and MC yields of high staitistics inclusive $\Lambda\bar{p}\pi^+(+c.c.)$ and $\Lambda\bar{\Lambda}$ events, selected with the same criteria, change when the vertex fit χ^2 and $c\tau$ values used in the selection requirements are varied. Compare with $\Lambda\Lambda$, number of $\Lambda\bar{\Lambda}$ sample is huge that means we can reduce statistical error in real data and MC. Using this data sample, we got $R = \epsilon(data)/\epsilon(MC)$ for χ^2 and $c\tau$ cut. Fig. 5.1 shows the $M(p\pi^-)$ *vs.* $M(\bar{p}\pi^+)$ scatter plot for selected $\Lambda\bar{\Lambda}$ events in the data. Because we need to care about statistical error in this sample, eventual systematic error is $\sigma = \sqrt{(1-R)^2 + \sigma_{stat}^2}$ and we can check R value is smaller than 1% and σ almost come from statistical error of sample data. So we got 2 3% systematic error for χ^2 and $c\tau$ cut creteria. Differ $\Lambda\Lambda$ channel error

estimation, we couldn't select proton and π in $\Lambda\bar{p}\pi^+(+c.c.)$ So using tight particle ID cut we reduce background.

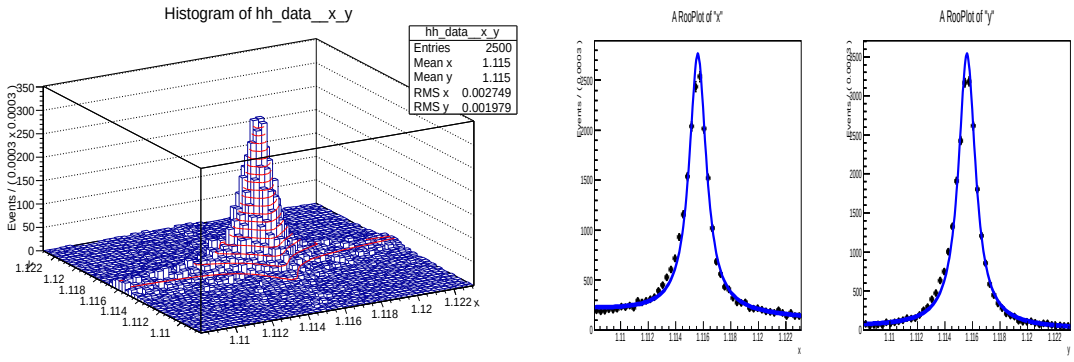

Figure 5.1: **Left:**he $M(p\pi^-)$ *vs.* $M(\bar{p}\pi^+)$ scatter plot distribution for the data. **Right:** Projections of the scatter plot distributions on to $M(p\pi^-$ (left) and $M(\bar{p}\pi^+)$ (right) axes with the results of the fit superimposed.

When we study correction factor $R_{\bar{\Lambda}\bar{\Lambda}}$, we got $R = 0.83 \pm 0.13$ and this systematic error is $\sigma(R_{\bar{\Lambda}\bar{\Lambda}}) = 15.6\%$ Because of low statistics, this factor's systematic error is estimated large. This error only affect to anti-particle channel $\bar{\Lambda}\bar{\Lambda}(\bar{\Lambda}\bar{p}\pi^+)$.

The other systematic error of efficiency come from momentum cut for $\Lambda p\pi$ sample. We give momentum cut for Λ and p_2. For checking signalMC dependece of momentum cut, we made another signalMC by changing Ξ^0's property like H-dibaryon. Because momentum difference near 0.5GeV is too big to check efficiency difference, it can depend statistical effect too much. By making signalMC with difference base, we check momentum difference effect in efficiency. Systematic error is $\sigma(p) = (\epsilon_{\Xi^{*0}} - \epsilon_{\Xi^0})/\epsilon_{\Xi^{*0}} = 1.7\%$.

For estimating systematic error by fitting, we used $\Xi_c^0(2470)$ resonance sample. signal yield difference to signal yield for changing fit-range orbinning is systematic error. By changing fit range $\pm 1 MeV$ which give small statis-

tical problem, we got 0.8% systematic error. Because binning change can big difference because of small signal of $\Xi_c^0(2470)$ we change signal mean of gaussian as $\pm 125 KeV$ which is half of bin-size. By this way we can estimate mean changed effect by changed bin-size and this error is $\sigma(bin) = 1.8\%$. Finally resolution error can get by changing resolution 10% for best fitted resolution. f correction factor what we use has negligable error, so resolution error by this estimation is 2.6%.

So above all systematic error is described in Table. 5.1 and almost error is a little over estimated by small number of sample.

Table 5.1: Systematic error sources (in percent). For cases where the H and $\bar{H}$ values differ, the $\bar{H}$ values are enclosed in parentheses.

Source	$H \to \Lambda p\pi^-$	$H \to \Lambda\Lambda$
$N_{\Upsilon(1S)} + N_{\Upsilon(2S)}$	2.3	2.3
tracking	1.4	1.4
proton pid	6.6	4.3
pion pid	2.8	–
Λ reconstruction	3.0(5.0)	12.0(9.0)
$M(\Lambda)$	1.0(1.0)	2.0(2.0)
goodvee	0.5(1.6)	3.4(2.6)
χ^2 requirement	2.8	2.5
$c\tau$ requirement	2.7	2.5
acceptance	1.9(15.8)	2.0(15.7)
continuum subtraction	1.4	1.4
$\mathcal{B}(\Lambda \to p\pi^-)$	0.5	1.0
fit range	0.8	0.8
binning	1.8	1.8
resolution	2.6	2.6
quadrature sum	10.2(19.1)	14.7(19.8)

5.2 Systematic error study for $H \to \Xi^- p$ channel

When we study systematic error of $H \to \Xi^- p$ channel, we need to study $\Upsilon(1S)$ and $\Upsilon(2S)$ sample separately. The reason is that we use $\Upsilon(1S)$ caseA data for cut estimation of $\Xi^{*0}(1530)$ resonance requirement. We can expect systematic error of caseA and caseB will be differ by different condition. Using same way as other H-dibaryon channel systematic error study, we can estimate errors by all cuts. For estimating systematic error of Ξ^2 cuts, $c\tau$, binning, and fit range, we use $\Xi^{*0}(1530)$ signal efficiency difference. For resolution, we use $\Xi_c(2470)$ signal. Estimated all errors is in Table. 5.2. When we got upperlimt, we used square root sum of $\sigma(\Upsilon(1S)) \oplus \sigma(\Upsilon(2S))$.

Table 5.2: Systematic error sources (in percent). For cases where the H and $\bar{H}$ values differ, the $\bar{H}$ values are enclosed in parentheses.

Source	$\Upsilon(1S) \to\ HX(\Xi^- p)$	$\Upsilon(2S) \to\ HX(\Xi^- p)$
$N_{\Upsilon(1S)} + N_{\Upsilon(2S)}$	2.3	3.6
tracking	4	1.4
proton pid	6.6	6.6
Λ reconstruction	4.5(3.9)	4.5(4.3)
$M(\Lambda)$	1.0	1.0
goodvee	1.3(1.0)	1.3(1.2)
$\chi^2_{\Lambda\pi^-}$ requirement	2.7	3.3
$\chi^2_{\Xi^- p}$ requirement	4.0	6.7
$c\tau$ requirement	2.6	3.3
acceptance	3.0	3.0
continuum subtraction	1.4	1.4
$\mathcal{B}(\Lambda \to p\pi^-)$	0.5	0.5
fit range	3.0	0.8
binning	0.3	0.1
resolution	2.5	2.5
quadrature sum	12.0(11.8)	12.9(12.8)

Chapter 6

Conclusions

The results reported in here are some of the most stringent constraints to date on the existence of H-dibaryon with mass near the $2m_\Lambda$ threshold and pentaquark. These upper limits are between one and two orders-of-magnitude below the average of the PDG value for inclusive $\Upsilon(1S)$ and $\Upsilon(2S)$ decays to antideuterons. Since $\Upsilon \to hadrons$ decays produce final states that are flavor-$SU(3)$ symmetric, this suggests that if an H-dibaryon exists in this mass range, it must have very different dynamical properties than the deuteron, or, in the case of $M_H < 2m_\Lambda$, a strongly suppressed $H \to \Lambda p\pi^-$ decay mode. Also above $m_{\Xi^-} + m_p$ mass region, although less interest in this mass region, upper limits are between one and two orders-of-magnitude below the average of the PDG value for inclusive $\Upsilon(1S)$ and $\Upsilon(2S)$ decays to antideuterons.

With the precise measurement of $\mathcal{B}(\Upsilon(1S) \to \Xi_c^0(2470)\ X) \times \mathcal{B}(\Xi_c^0 \to \Xi^-\pi^+)$, we can convince the no-existence of Ξ_5 pentaquark in same branching fraction of deuterons. There's many experiments which compare with $\Xi^{*0}(1530)$ resonance signal for getting upperlimit even with more signal than my result. But there's no results about 6-quark combination structure signal for comparision, but our data can compare with anti-deuteron and $\Xi^{*0}(1530)$

both.

In addidition we report first measurements of the inclusive branching fraction $\mathcal{B}(\Upsilon(1S) \to \overline{\Xi^{*0}}(1530)\, X) = (3.23 \pm 0.02\ (\text{stat})\ \pm 0.26\ (\text{syst})) \times 10^{-3}$, and inclusive product branching fraction $\mathcal{B}(\Upsilon(1S) \to \Xi_c^0(2470)\, X) \times \mathcal{B}(\Xi_c^0(2470) \to \Xi^-\pi^+) = (3.42 \pm 0.34\ (\text{stat}) \pm 0.15\ (\text{syst})) \times 10^{-5}$, using data samples containing 102 million $\Upsilon(1S)$ decays and 158 million $\Upsilon(2S)$ collected in the Belle detector at the KEKB collider.

Bibliography

[1] M. Gell-Mann, Phys. Lett. **8**, 214 (1964).

[2] G. Zweig, CERN Report 8419/Th.401 (1964).

[3] An interesting summary of the early searches for a strangeness +1 baryon is provided in the introduction section of B.K. Jennings and K. Maltman, Phys. Rev. D **69**, 094020 (2004).

[4] R.L. Jaffe, SLAC Report No. SLAC-PUB-1774 (1976).

[5] D. Strottman, Phys. Rev. D **20**, 748 (1979).

[6] R.L. Jaffe, Phys. Rev. Lett. **38**, 195 (1977).

[7] M.Praszalowicz *et al.*, Proceedings of the Workshop on Skyrmions and Anomalies(1987) p.112

[8] D. Diakonov, V. Petrov and M. Polyakov, Z. Phys. A **359**, 305 (1997).

[9] T. Nakano, *et al.* (LEPS Collaboration), Phys. Rev. Lett. **91**, 012002 (2003).

[10] A review of the events during this period together with references to the experimental work is provided in R.A. Schumacher, arXiv:nucl-ex/051204.

[11] W. M. Yao, *et al.* (Particle Data Group), J. Phys. G: Nucl. Part. Phys. **33**, 1 (2006), see, in particular, the "Pentaquark Update" by G. Trilling on page 1019.

[12] In the following, the inclusion of charge-conjugate modes is implied unless explicity stated otherwise.

[13] C. Alt, *et al.* (NA49 Collaboration), Phys. Rev. Lett. **92**, 042003 (2004).

[14] The $\Xi^{*0}(1530)$ is the $I_3 = +\frac{1}{2}$, strangeness = -2 member of the lowest-lying $J^P = \frac{3}{2}^+$ baryon decuplet; $M_{\Xi^{*0}(1530)} = 1531.80 \pm 0.32$ MeV and $\Gamma_{\Xi^{*0}(1530)} = 9.1 \pm 0.5$ MeV [29].

[15] R. Jaffe and F.Wilczek, Phys. Rev. Lett. **91**, 232003 (2003).

[16] A. Abulencia, *et al.* (CDF Collaboration), Phys. Rev. D **75**, 032003 (2007).

[17] J.M.Link *et al.* Phys. lett. B **661**, 14 (2008)

[18] Acta Phys. Polon. Supp. **5**, 593 (2012)

[19] S.R. Beane, *et al.* (NPLQCD Collaboration), Phys. Rev. Lett. **106**, 162001 (2011).

[20] S.R. Beane, *et al.* (NPLQCD Collaboration), Mod. Phys. Lett. A **26**, 2587 (2011).

[21] T. Inoue, *et al.* (HALQCD Collaboration), Phys. Rev. Lett. **106**, 162002 (2011).

[22] H. Takahashi, *et al.*, Phys. Rev. Lett. **87**, 212502 (2001).

[23] S.R. Carames and A. Valcarce, arXiv:1204.5683 [hep-ph].

[24] C.J. Yoon, *et al.* (KEK-PS E522 Collaboration), Phys. Rev. C **75**, 022201(R) (2007).

[25] R.W. Stotzer, *et al.* (BNL-E836 Collaboration), Phys. Rev. Lett. **78**, 3646 (1997).

[26] A. Alavi-Harati, *et al.* (KTeV Collaboration), Phys. Rev. Lett. **84**, 2593 (2003).

[27] I. Chemakin, *et al.* (E910 Collaboration), Nucl. Phys. A **639**, 407c (1998).

[28] J.K. Ahn, *et al.* (KEK-PS E224 Collaboration), Phys. Lett. B **444**, 267 (1998), J. Belz, *et al.*, Phys. Rev. Lett. **76**, 3277 (1996) & Phys. Rev. C **56**, 1164 (1997).

[29] K. Nakamura, *et al.* (Particle Data Group), J. Phys. G **37**, 075021 (2010).

[30] D.M. Asner, *et al.* (CLEO Collaboration), Phys. Rev. D **75**, 012009 (2007), see also

[31] T. F. CARAME and A. VALCARCE,

[32] T.Sakai *et al.*, Prog. Theor. Exp. Phys.1372000

[33] K. F. Chen *et al.*, BelleNote 684

[34] H. Feshbach, Ann. Phys. (Leipzig) 5, 357,(1958)

[35] R. Jaffe, A. Jain. Phys. Rev. D **71**, 034012 (2005)

[36] D. Rujula *et al.*, Phys. Rev. D **12**, 1 (1975)

[37] K. Shimizu, Rep. Prog. Phys. **52**, 1 (1989)

[38] T.Abe *et al.*, Prog. Theor. Exp. Phys.03A0012013

[39] A. Abashian *et al.*, NIM **A479**, 117 (2002)

[40] F.Sauli, Cern-77-09 (1977)

[41] M.Akatsu *et al.*, NIM **A454**, 322 (2000)

[42] R. Fruwirth, Nucl. Instr. and Meth.A2624441987

[43] T. E. Browder *et al.*, Prog. Part. Nucl. Phys. **35**, 81 (1995)

[44] X. L. Wang, BelleNote 1138,1185

[45] B. Casey, BelleNote 390

[46] PDG book fig 46.10

[47] T. Sjostrand *et al.*, Comput. Phys. Commun. **178**, 852 (2008)

[48] S.-K. Choi and S.L. Olsen, *Studies of* $X(3872) \to \pi^+\pi^- J/\psi$ *with the full Belle data set*, Belle Note 1177 (2011), unpublished.

[49] We use the RooVoigtian function as implemented in RooFit:

$$\frac{1}{(x-m_0)^2+(\Gamma_0/2)^2} \otimes \exp -\frac{x^2}{2\sigma^2},$$

where $x = M(\pi^+\Xi^-)$, m_0 & Γ_0 are set at the PDG values for $m_{\Xi^{*0}(1530)}$ & $\Gamma_{\Xi^{*0}(1530)}$, and σ is the resolution (allowed to float in the fit).

[50] H. Albrecht *et al.* (ARGUS Collaboration), Phys. Lett. **B241**, 278 (1990). We use:

$$\begin{aligned} f_{bkg} &= x[(\frac{x}{m_0})^2-1]^p \exp(c[(\frac{x}{m_0})^2-1]) && x > m_0 \\ &= 0 && x < m_0, \end{aligned}$$

where $x = M(\pi^+\Xi^-)$, $m_0 = m_{\Xi^-} + m_{\pi^+}$ and c and p are free parameters.

Appendix A

Experimental search list

A.1 H-dibaryon searches

Table A.1: Experimental searches for the H-dibaryon. [32]

Collaboration	reaction process(production/decay)
BNL E703	$p + p \rightarrow K^+K^+X$
BNL E810	$Si + Pb\ collision/\ H \rightarrow \Sigma^- p,\ \Lambda p\pi^-$
BNL E813	$K^- + p \rightarrow K^+ + \Xi^-,$
	$(\Xi^- d)_{atom} \rightarrow H + n$
BNL E830	$K^- +^3 He \rightarrow K^+ Hn$
BNL E836	$K^- +^3 He \rightarrow K^+ Hn$
	$K^- +^6 Li \rightarrow K^+ HX$
BNL E864	$Au + Pb\ collision$
BNL E885	$K^- + (p) \rightarrow K^+\Xi^-$
	$(\Xi^- A)_{atom} \rightarrow HX$
	$K^- + A \rightarrow K^+ HX$

BNL E886	$Au\ +\ Pt\ collision$
BNL E888	$p\ +\ A\ \rightarrow\ HX\ /\ H\ \rightarrow\ \Lambda nor\Sigma^0 n,$
	$H\ +\ A\ \rightarrow\ \Lambda\Lambda A$
BNL E896	$Au + Au\ collision\ /\ H \rightarrow \Sigma^- p\ \rightarrow\ n\pi^- p,$
	$H \rightarrow \Lambda p\pi\ \rightarrow\ p\pi^- p\pi^-, H\ \rightarrow\ \Lambda n \rightarrow p\pi^- n$
BNL E910	$p\ +\ A\ /\ H\ \rightarrow\ \Lambda p\pi,\ H\ \rightarrow\ \Sigma^- p$
BNl STAR	$Au\ +\ Au\ collsion$
KEK E176	$K^- + pp(in^{12}C) \rightarrow K^+ H$
	$K^- + p \rightarrow k^+\Xi^-, \Xi^- + p(in^{12}C \rightarrow H$
KEK E224	$K^- + pp(in^{12}C) \rightarrow K^+ H$
	$K^- + p \rightarrow k^+\Xi^-, \Xi^- + p(in^{12}C \rightarrow H$
KEK E248	$p + p \rightarrow K^+ K^+ X$
Fermilab E791	$H \rightarrow \Lambda p\pi$
	$H \rightarrow \Lambda\Lambda$
Fermilab KTeV Co.	$p + A\ /\ H \rightarrow \Lambda p\pi$
Shahbazian et al.	$p +^{12} C \rightarrow H(H^+)X/$
	$H \rightarrow \Sigma^- p, \Sigma^- \rightarrow \pi^- n$
	$H^+ \rightarrow \Lambda p\pi^0$
	$H^+ \rightarrow \Lambda p$
Alekseev et al.	$n + A \rightarrow HX/H \rightarrow \Lambda p\pi$
DIANA co.	$H \rightarrow \Sigma^- p$
Condo et al.	$\bar{p} + Xe \rightarrow K^+ HX, K^+ K^+ HX/H \rightarrow \Sigma^- p$
Ejiri et al.	$d \rightarrow H\beta\nu,\ ^{10}Be \rightarrow^8 Be\ H$
CERN NA49	Pb+Pb collision / $H \rightarrow \Sigma^- p, \Lambda p\pi$
CERN WA89	$\Sigma^- + A \rightarrow HX/H \rightarrow N\Xi, \Lambda\Lambda$
	$H \rightarrow \Lambda p\pi, \Sigma p, \Lambda n$
CERN WA97	Pb+Pb collision
CERN ALICE	Pb+Pb collision
CERN OPAL	$Z^0\ decay$

A.2 Penta-quark searches

Table A.2: Unsuccessful searches for penta-quarks. [29]

Experiment	Reaction	Limits,etc
Searches for the $\Theta(1540)^+$		
BABAR	$B^0 \to (pK_S^0)\bar{p}$	$< 2 \times 10^{-7} per B^0$
CLAS	$\gamma p \to (nK^+/pK_s^0)K^0$	$\sigma < 0.7nb, 100k\Lambda(1520)$
CLAS	$\gamma d \to (nK^+)pK^-$	$\sigma < 0.3nb$
CLAS	$\gamma d \to (nK^+)\Lambda$	$\sigma < 5 - 25nb$
COSY-ANKE	$pp \to (pK_S^0)\Lambda\pi^+$	$\sigma < 58nb$
COSY-TOF	$pp \to (pK_S^0)\Sigma^+$	$\sigma < 150nb$
DELPHI	$Z \to (pK_S^0)X$	$< 5.1 \times 10^{-4} per Z$
FOCUS	$\gamma A \to (pK_S^0)X$	$400k\Sigma(1385)^+$
HERA-H1	$ep \to (p/\bar{p}K_S^0)eX$	$\sigma < 30 - 90pb$
KEK-E522	$\pi^- p \to K^-(X)$	$\sigma < 3.9nb$
L3	$\gamma^*\gamma^* \to (p/\bar{p}K_S^0)X$	$\sigma < 1.8nb$
NOMAD	$\nu_\mu N \to (pK_S^0)X$	$< 2.13 \times 10^{-3} per evt$
Searches for the $\Phi(1860)$		
CDF	$\bar{p}p \to (\Xi^-\pi^\pm)X$	$1.9k\Xi(1530)$
DELPHI	$Z \to (\Xi^-\pi^-)X$	$< 2.9 \times 10^{-4} per Z$
FOCUS	$\gamma N \to (\Xi^-\pi^-)X$	$65k\Xi(1530)$
HERA-H1	$ep \to (\Xi^-\pi^\pm)eX$	$163\Xi(1530)$
SERP-EXCHARM	$nC \to (\Xi^-\pi^\pm)X$	$1.5k\Xi(1530)$

국문 초록

기존 강입자(hadron)의 구성 쿼크(quark)수를 넘는 쿼크수로 이루어진 엑조틱바리온(exotic baryon)은 이른 양자색역학(Quantum Chromodynamics: QCD)에서부터 예측되어 왔다. 많은 실험들이 이루어졌지만 아직 엑조티바리온의 존재에 대한 확실한 결론이 나오지 않는 상황이다. 5개의 쿼크로 구성된 펜타쿼크(Pentaquark) 바리온은 2003년부터 실험이 전성기를 이루었지만 2009년에 존재의 부정과 함께 실험이 거의 사라졌다. 그러나 비슷한 시기에 6개의 쿼크로 구성된 에이치-다이바리온(H-dibaryon)에 대한 실험이 긍정적인 결과를 내었고 이는 엑조틱바리온 실험이 계속될 필요가 있음을 보여줬다.

이 논문에서는 이러한 엑조틱바리온 실험의 일환으로 웁실론(1,2에스)(Υ(1,2S)) 보토모늄(bottomonium) 메존(meson)으로부터 붕괴하는 -2 전하의 카이(Ξ_5^{--}) 펜타쿼크과 에이치-다이바리온을 찾아보았다. 더불어 1억200만개의 웁실론(1에스) 보토모늄 메존과 1억 5500만개의 웁실론(2에스) 보토모늄 메존으로부터 붕괴하는 바리온을 포함한 붕괴율(branching fraction $B(\Upsilon(1S) \to \bar{\Xi}^{*0}(1530)X) = (3{,}23 \pm 0.15(stat) \pm 0.26(syst)) \times 10^{-3}$), 그리고 바리온을 포함한 붕괴비율 $B(\Upsilon(1S) \to \Xi_c^0(2470)X) \times B(\Xi_c^0(2470) \to \Xi^-\pi^+) = (3{,}42 \pm 0.34(stat) \pm 0.15(syst)) \times 10^{-3}$) 측정결과를 보고한다. 모든 데이터는 케이이케이비 가속기(KEKB collider)의 벨 검출기(Belle detector)에서 모은 것이다.

주요어: 엑조틱, 펜타쿼크, 에이치-다이바리온, 벨, 붕괴율

학 번 : 2009-20402

감사의 글

원자핵공학과를 졸업하고 물리과대학원에 와서 부족한 지식으로 졸업논문을 완성하니 졸업에 대한 약간의 흥분과 더불어 부족한 저의 지식에 대한 자책과 아쉬움이 몰려옵니다. 3년 반이라는 기간 동안 교수님들의 은덕과 선배들의 가르침에 감사 드립니다.

I really thanks to prof. Olsen and I' m lucky to be a student of you. 3년이란 시간 동안 올슨 교수님께 많은 것을 배우고 물리학자로써의 방식을 느꼈습니다. 감사합니다. 그리고 지도교수님으로써 제가 이렇게 공부할 수 있는 기회를 주시고 가르쳐 주신 김선기 교수님, 최선호 교수님께도 감사 드립니다. 제 이른 졸업과 함께 부족한 논문을 심사해주신 이원종 교수님. 방형찬 교수님 그리고 부산에서 올라와 주신 안정근 교수님께 감사 드립니다. 하나하나의 질문과 조언이 제 공부에 큰 도움이 되었습니다.

제가 이 논문을 쓰기 위해서 많은 선배님들께 지식을 배웠습니다. 리진 교수님께서는 제가 실험 중반에서부터 깊은 분석법과 인식을 배우는데 많은 것을 가르쳐 주셨습니다. 그리고 슈롱 박사님 또한 제 연구의 일환으로 중국의 베스가속기를 공부하는데 도움을 주었습니다. 감사합니다. 수신핑 박사님과는 제 논문이 다 끝날 때 만났지만 관심을 가지고 많은 질문을 해주신점 감사 드립니다.

3년의 연구실 생활 동안 많은 것을 배울 수 있었고 함께 할 수 있었던 동료들에게 감사에 말을 전합니다. 제가 연구를 시작함에 있어서 기초를 가르쳐주시고 연구실의 큰형으로써 모범을 보여주시던 명재형 감사 드리고 미국생활 잘하세요. 그리고 약간은 무섭지만 속은 따뜻한 수형 항상 질문 많이 드려서 죄송하고 감사해요. 잘 대해드리지 못해 죄송했던 승천이형, 항상 잘 대해주신 주희누나, 양양대장 정훈이형, 나사의 멋쟁이 상준이형, 재미있는 재금이누나, 동물의 왕 경원이누나, 행정실 큰누나 혜정이누나, 작은 비서 고은이 누나 모두 복 받으세요.

먼저 졸업하고 하와이로 가서 환골탈태한 박정완이, 아모레의 미래 건보 그리고 국가보안의 미래 김정훈이 다 대성해라. 또 원자핵공학과에서 물리과로 와서 적응이 어려운데 친구가 되어준 동현이형, 융희, 환철이, 오비지 그리고 재원아 고맙고 앞으로도 잘 지내자구. 그리고 같은 벨 연

구를 하는 친구 창우야 파이팅. 지금 같은 방을 쓰고 있는 성배형, 재용이, 민정이도 다들 잘 지내기를 바래요.

그리고 항상 저에게 가장 큰 힘이 되어주고 함께 해주신 아버지, 어머니, 송이누나 사랑하고 감사합니다.

물리라는 학문의 박사가 됨이 앞으로 제가 알고자 하는 모든 지식과 제가 얻고 싶은 모든 사유에 큰 힘이 되리라 믿습니다. 앞으로도 원하는 지식을 얻음에 있어서 끊임없이 달려갈 수 있기를 그리고 의지를 놓치지 않기를 바랍니다.

김봉호